Diss. ETH No. 26662

Balloon-borne Atmospheric Water Vapor Measurement by Laser Absorption Spectroscopy

A thesis submitted to attain the degree of

DOCTOR OF SCIENCES of ETH ZURICH
(Dr. sc. ETH Zurich)

presented by

MANUEL GRAF

MSc in Physics, University of Zurich

born on 03.02.1992
citizen of Rebstein SG

accepted on the recommendation of

Prof. Dr. Thomas Peter, ETH Zurich
Dr. Béla Tuzson, Empa Dübendorf
Dr. Lukas Emmenegger, Empa Dübendorf
Dr. Ruud Dirksen, DWD Lindenberg, Germany

2020

Contents

1 Introduction **1**
- 1.1 Water Vapor in the UTLS . . . 2
- 1.2 Open Questions . . . 4
- 1.3 Measurement of Water Vapor in the UTLS . . . 4
- 1.4 Aim of this Project . . . 7

2 Laser Absorption Spectroscopy **10**
- 2.1 Radiative Transfer and the Beer-Lambert Law . . . 11
- 2.2 Rovibrational Transitions . . . 12
- 2.3 Direct Absorption Spectroscopy . . . 15

3 Multipass Cell Design **17**
- 3.1 Beam Folding Analysis and Optimization of Mask-Enhanced Toroidal Multipass Cells . . . 18
- 3.2 Segmented Circular Multipass Cell . . . 27

4 Instrumentation **35**
- 4.1 Targets and Conditions . . . 36
- 4.2 Quantum Cascade Lasers . . . 36
- 4.3 Spectroscopic Considerations . . . 37
- 4.4 Hardware and Construction . . . 39
- 4.5 Thermal Stabilization . . . 43
- 4.6 Electronics and Software . . . 45

5 Testing and Characterization **49**
- 5.1 Closed-path Measurements . . . 50
- 5.2 Open-path Measurements . . . 55
- 5.3 Assessment in Climate Chambers . . . 60
- 5.4 Test Flights . . . 62
- 5.5 Further Developments . . . 69

6 Conclusions **72**

A QCLAS – Additional Information **74**
A.1 Summarized Specifications 74
A.2 Power Consumption and PCM Distribution 75
A.3 Balloon-borne Test Flights – Details 75

B Pressure Chamber **76**

Bibliography **77**

Acknowledgments **87**

Publications **89**

Summary

The radiative balance of the Earth is particularly affected by the abundance of water vapor, not only in the lower troposphere, but also in the upper troposphere and lower stratosphere (UTLS). Besides the absorption of long-wave radiation originating from the Earth's surface, water vapor is responsible for a variety of chemical and microphysical processes. Understanding the mechanisms that control UTLS water vapor, as well as its long-term variation, is important for reliable projections of the evolution of the global climate system. However, these insights are currently limited by the lack of accurate, frequent, and comparable water vapor measurements in the UTLS. In addition, the most frequently used instruments for high-accuracy water vapor measurements, the cryogenic frost point hygrometers, are not devoid of own weaknesses and currently seek substitution: The cooling agent fluoroform (R23, CHF_3), required for its operation, is to be phased out due to its global warming potential. Alternative concepts to frost point hygrometry are generally expensive in terms of weight and energy consumption, hence limiting their frequent deployment.

In this project, an open-path direct laser absorption spectrometer is developed, sufficiently small and lightweight to be deployed aboard of meteorological balloons. Its low weight (3.9 kg) and compactness ($30 \times 23 \times 11$ cm^3) inherently reduces sources of contamination and allows flexible and frequent soundings. The instrument incorporates a quantum cascade laser as a rapidly tunable narrowband light source in the mid-infrared spectral region, where H_2O exhibits strong absorption lines. To achieve enhanced robustness, while satisfying the stringent mass limitation, the optical and electronical concept is completely reconsidered with respect to laboratory-based spectrometers. This comprises the elaboration of a lightweight and compact multipass cell concept, called the *segmented circular multipass cell* (SC-MPC), which enables the reduction of the optical setup to its basic components only, i.e., the laser, the MPC, and the detector. Furthermore, the instrument incorporates custom-developed electronics for fast and power-saving laser driving, data-acquisition hardware based on field-programmable gate arrays (FPGA), dedicated software for controlling and monitoring, and a thermal stabilization system that suppresses the external temperature variation by almost four orders of magnitude. The spectrometer is a fully integrated, standalone system, operating autonomously for the duration of a balloon flight.

The H_2O amount fraction is retrieved by calibration-free evaluation of the spectral data, i.e., only relying on SI-traceable measurements and absorption line parameters provided by spectral databases. Laboratory-based characterization experiments demonstrate an agreement within 2 % to a reference. In a first balloon-borne test campaign, the instrument was successfully deployed up to the UTLS in two consecutive flights. The comparison to CFH shows a mean deviation of 3 % in the troposphere. At higher altitude, accumulated humidity within the enclosure of the instrument currently leads to interference with the atmospheric absorption signal. Despite this restriction, the tests demonstrate the feasibility of spectroscopic water vapor measurements in the UTLS at an effective temporal resolution of 1 Hz during ascent and descent.

Zusammenfassung

Der Wasserdampfgehalt in der oberen Troposphäre und unteren Stratosphäre (UTLS) hat einen wichtigen Einfluss auf das Strahlungsgleichgewicht der Erde. In dieser Region ist der Wasserdampf an verschiedenen chemischen und mikrophysikalischen Prozessen beteiligt und absorbiert langwellige Strahlung, die von der Erdoberfläche emittiert wird. Um das zukünftige Entwicklung unseres Klimas verlässlich vorhersagen zu können, ist es wichtig, dass die involvierten Prozesse in der UTLS verstanden sind. Dieses Verständnis ist allerdings heute, mangels Verfügbarkeit genauer, häufiger und vergleichbarer Wasserdampfmessungen, beschränkt. Überdies müssen die am häufigsten verwendeten Geräte für die hochpräzise Messung von Wasserdampf in der UTLS, die kältemittelbasierten Frost- bzw. Taupunktspiegel, in den nächsten Jahren wesentlich angepasst oder gar ersetzt werden, da der Einsatz des darin verwendeten Kältemittels wegen seines starken Beitrags zum globalen Treibhauseffekt reduziert werden muss. Die bis heute vorgestellten Alternativen zur Taupunktspiegelhygrometrie sind im Allgemeinen schwer und energieaufwendig, was ihren regelmässigen und flexiblen Einsatz stark behindert.

In diesem Projekt wird ein direktes Laserabsorptionsspektrometer mit offenem Strahlengang entwickelt, welches genügend klein und leicht ist, um es an einem meteorologischen Ballon aufsteigen zu lassen. Sein geringes Gewicht (3.9 kg) und die hohe Kompaktheit ($30 \times 23 \times 11$ cm^3) reduzieren die Quellen von Kontamination inhärent und erlauben flexible und häufige Messungen. Das Instrument beinhaltet einen Quantenkaskadenlaser als schnell durchstimmbare schmalbandige Lichtquelle im mittleren Infrarotbereich, wo H_2O starke Absorptionslinien besitzt. Um hohe Robustheit zu erreichen und gleichzeitig die enge Gewichtsbeschränkung zu erfüllen, wurde das optische und elektronische Konzept komplett überarbeitet im Vergleich zu laborbasierten Spektrometern. Dies beinhaltet die Entwicklung eines leichten und kompakten Konzepts für Mehrfachreflektionszellen (MPC), genannt *segmentierte zirkuläre Mehrfachreflektionszelle* (SC-MPC), das es erlaubt, den optischen Aufbau des Spektrometers auf ein absolutes Minimum zu reduzieren; lediglich bestehend aus den Basiselementen Laser, MPC und Detektor. Zusätzlich beinhaltet das Instrument speziell entwickelte Elektronik für das energiesparende und schnelle Betreiben des Lasers, FPGA-basierte Datenerfassung, Kontrollsoftware, sowie ein thermisches Stabilisationssystem, das die externen Temperaturschwankungen um fast vier Grössenordnungen unterdrückt. Das Spektrometer ist ein vollständiges und selbständiges System, das während der zweistündigen Dauer eines Ballonflugs autonom funktioniert.

Die Messwerte werden in einem kalibrationsfreien Verfahren, d.h., nur unter Zuhilfenahme von SI-rückführbaren Messwerten und tabellierten Linienparametern, aus den gemessenen Spektren berechnet. In laborbasierten Charakterisationsexperimenten zeigt der gemessene Stoffmengenanteil eine Übereinstimmung von 2 % mit der Referenzmessung. In einer ersten ballongestützten Testkampagne wurde das Instrument in zwei aufeinanderfolgenden Flügen bis in die UTLS gebracht. In der Troposphäre zeigt der Vergleich zum Taupunktspiegelinstrument CFH eine durchschnittliche Abweichung von 3 %. In grösserer Höhe behinderte die Akkumulation von Feuchtigkeit

innerhalb des Geräts die atmosphärische Messung. Trotz dieser Einschränkung zeigen diese Tests die Realisierbarkeit spektroskopischer Messungen von Wasserdampf in der UTLS mit einer effektiven zeitlichen Auflösung von 1 Hz während des Auf- und Abstiegs.

Abbreviations

BDC	Brewer Dobson circulation
CRDS	cavity ring-down spectrometer
CFH	cryogenic frost point hygrometer
CW	continuous wave
DAQ	data acquisition
dTLAS	direct tunable laser absorption spectroscopy
FPGA	field-programmable gate array
FPH	cryogenic frost point hygrometer (by NOAA)
GHG	greenhouse gas
GCOS	Global Climate Observing System
HHL	high-heat-load laser housing
HTP	Hartman-Tran profile
I^2C	inter-integrated circuit bus
iCW	intermittent continuous wave
IR	infrared
LiPo	lithium polymer battery
MCT	Mercury/Cadmium/Telluride detector
MOL	Meterological Observatory Lindenberg
MPC	multipass cell
NTC	negative temperature coefficient sensor
OPL	optical path length
PCM	phase-change material
PID	proportional-integral-derivative controller
PWM	pulse width modulation
QCL	quantum cascade laser
QCLAS	quantum cascade laser absorption spectrometer
RH	relative humidity
SC-MPC	segmented circular multipass cell
SI	international system of units
SNR	signal-to-noise ratio
T(D)LAS	tunable (diode) laser absorption spectroscopy
TEC	thermoelectric cooler (Peltier element)
TTL	tropical tropopause layer
UAV	unmanned aerial vehicle
UTLS	upper troposphere and lower stratosphere
XPS	expanded polystyrol

Symbols

symbol	description
p	pressure (1 atm = 1013.25 hPa)
T	temperature (0 ℃ = 273.15 K)
N	amount of substance
$\tilde{V}$	volume
n	number density
χ	amount fraction $\chi_s = N_s/N_{\mathrm{tot}}$
r	mixing ratio $r_s = N_s/(N_{\mathrm{tot}} - N_s)$
λ	wavelength
$\tilde{\nu}$	wavenumber (inverse wavelength $1/\lambda$)
t	time
e_s	saturation vapor pressure
g	standard acceleration due to gravity on Earth
E	energy
τ	quantum state lifetime
Φ	line broadening function
S_{ij}	absorption line intensity for the transition $i \leftarrow j$
V	Voigt function
σ	absorption coefficient (cross-section) *or* standard deviation
γ	air broadening coefficient
n_{air}	temperature dependence coefficient of the air-broadening
α	Doppler broadening coefficient
I_0	laser output intensity
I_b	zero-absorption intensity (transmission baseline)
I_z	measured transmission intensity after a distance z
OPL	optical path length
z	optical path length *or* beam waist position
K	Fresnel-Huygens kernel
u	irradiance field
$\mathbf{A}$	paraxial transfer matrix
w	beam (waist) size (1σ)
p, q	pattern identifier for circular MPCs
ϑ	beam coupling angle for circular MPCs
δ	beam folding efficiency (OPL per volume)
f	focal length
R	radius of curvature
ϕ	phase angle
C	scaling factor for the segment size of MPCs

For dimensionless amount-of-substance ratios, the pseudo-unit *parts-per-million by volume* (ppmv) is used in the text, denoting µmol mol^{-1}.

Chapter 1

Introduction

Water vapor is an important climate variable and plays a crucial role in various atmospheric processes from the ground to the upper atmosphere. It is a key driver of phenomena on all spatial and temporal scales – from chemistry on the molecular level up to global circulation patterns. The water vapor content, especially in the upper troposphere and lower stratosphere (UTLS), influences the Earth's climate by affecting the radiative balance. The strong ability of water vapor to absorb infrared radiation, makes it the strongest contributor to the greenhouse effect. At the same time, water vapor is a prerequisite for the formation of clouds, which attenuate and reflect incoming solar shortwave radiation, thereby influencing the Earth's albedo. Climate modeling and predictions are therefore crucially dependent on the accurate knowledge of the water vapor abundance throughout the lower and middle atmosphere and on the understanding of the processes that control its variation. However, in contrast to well-mixed atmospheric trace gases, such as, e.g., CO_2, water vapor is far more difficult to track, due to its high variability: Its vertical abundance profile ranges from mixing ratios of a few percent on the ground to a few parts-per-million in the lower stratosphere. Whereas on ground, water vapor measurement can be accomplished by low-cost capacitive sensors, its assessment in the UTLS is unequally more challenging due to the low H_2O abundance and the prevailing harsh environmental conditions, namely low pressures and temperatures. Many high-accuracy instruments for the UTLS are strongly restraining the flexibility of deployment: Either because of their large mass and energy consumption (Rollins et al., 2014) or because the measurements are restricted to the nighttime (Lykov et al., 2011). In addition, enhanced disagreements among the existing instruments are currently limiting the reliability of the measurements and, thus, the understanding of the processes controlling humidity in the UTLS (Fahey et al., 2014). Therefore, this work is intended to amend this situation by a novel approach to in-situ UTLS water vapor measurements.

1.1 Water Vapor in the UTLS

1.1.1 Controlling Mechanisms

An explanation for the extreme dryness of the stratosphere ($2 - 10$ ppmv) was first given by Alan W. Brewer (1949). Based on balloon-borne observations, he proposed a global meridional circulation pattern referred to as the *Brewer-Dobson circulation* (BDC). The BDC is maintained by extratropical poleward pumping by the breaking of gravity- and Rossby-waves, which acts as a suction pump to air ascending in the tropics (Holton et al., 1995), as shown in Fig. 1.1. This effect decides upon the injection rate of air and moisture into the stratosphere, thus, any variation in the involved dynamics may alter the stratospheric water vapor content. The adiabatic cooling experienced by ascending air parcels, leads to very cold temperatures of the tropical tropopause layer (TTL), resulting in low water vapor content (cold-trap effect). Therefore, the TTL-temperature is mainly responsible for the amount of H_2O injected into the stratosphere (Fueglistaler et al., 2009). Indeed, the seasonal temperature cycle of the TTL is observable as a vertical propagation signature in water vapor concentration within the stratosphere, referred to as *tape recorder-effect* (Mote et al., 1996; Dessler et al., 2014).

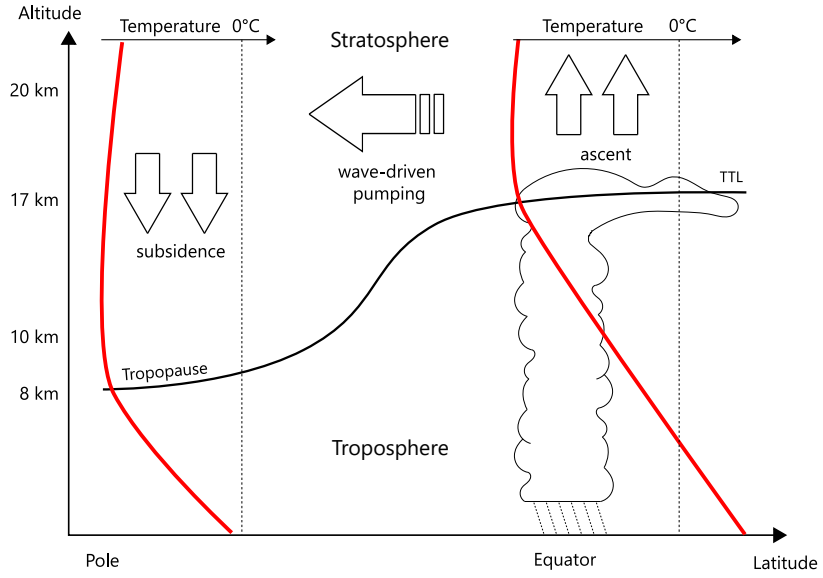

Figure 1.1: Brewer-Dobson circulation as most important mechanism for stratospheric humidity. (Figure inspired by Holton et al. (1995))

1.1.2 Stratospheric Chemistry

Since H_2O is an inert and photostable molecule, water vapor is almost solely brought to and removed from the stratosphere by transport processes. Nevertheless, it takes part in a number of chemical processes and it is the primary source of the OH radical

in the UTLS (Hanisco et al., 2001). Some H_2O is generated in the middle and upper stratosphere via photo-oxidation of methane (CH_4). This represents an important atmospheric sink of methane which is itself a strong greenhouse gas (Revell et al., 2016).

The presence of stratospheric water vapor and temperatures below $-78\,°C$ are a prerequisite for the formation of polar stratospheric clouds, which support heterogeneous, chlorine-induced ozone depletion (Kirk-Davidoff et al., 1999). Therefore, increasing stratospheric water vapor potentially delays the recovery of the stratospheric ozone layer (Anderson et al., 2012).

1.1.3 Radiative Balance

The radiative balance, i.e., the budget between the incoming shortwave radiation from the sun and the outgoing, reflected and re-emitted longwave radiation from the Earth, is the driver of the Earth's climate. Imbalances ultimately lead to changes of the global temperature. Water vapor has an impact on both sides of this balance; while it leads to a warming of the Earth's surface due to the greenhouse effect, the formation of clouds has a cooling effect. Therefore, the determination of its abundance throughout the atmosphere is of high importance for reliable prediction of climate evolution.

The H_2O molecule is a strong longwave absorbent and exhibits multiple absorption bands throughout the mid and near infrared spectral region. Due to the high abundance of water vapor in the troposphere, it is *the* dominant GHG, contributing about $50\,\%$ to the total greenhouse effect (Schmidt et al., 2010). Despite the much lower abundance in the UTLS, strong dependencies have been identified between UTLS water vapor concentration and surface climate change (Soden, 2005; Dessler and Sherwood, 2009; Solomon et al., 2010). Sensitivity studies indicate that the water vapor concentration, especially in the upper tropopsphere, must be known with an accuracy of $3-10\,\%$ to avoid uncertainties in the radiative effect equivalent to a doubling of CO_2 (Harries, 1997). As a reaction to global warming triggered by increasing levels of anthropogenic GHG, the water vapor abundance is expected to increase throughout the troposphere and the lower stratosphere (Manabe and Wetherald, 1967; Held and Soden, 2000), leading to a positive feedback effect (Forster and Shine, 1997; Banerjee et al., 2019). This can lead to a temperature increase of more than twice the amount solely attributed to higher CO_2 levels (Dessler et al., 2013).

Water vapor in the UTLS not only absorbs longwave radiation, it also influences the flux of incoming solar shortwave radiation. In the upper troposphere, ice crystals can form by resublimation of water vapor (Gettelman and Sherwood, 2016). Thereby, the interaction characteristics of H_2O with visible light changes, leading to a variation of the Earth's albedo and to a removal of water from the UTLS. Cloud formation, however, involves complex microphysical processes and not necessarily occurs simply upon exceedence of $100\,\%$ relative humidity (Peter et al., 2006). Especially in the clean upper troposphere, the lack of condensation nuclei suppresses cloud formation. The detailed knowledge about nucleation mechanisms is crucial to understand the moistening of the stratosphere. Insight to the underlying processes can be gained by

in-situ measurements of the water vapor content at high spatial resolution and high accuracy.

1.2 Open Questions

Given the global impact of UTLS water vapor to the Earth's climate system, it is of high importance that our understanding of the involved processes advances to a level, at which theory and measurement are in good agreement. This level, apparently, is not yet reached: By combination of several datasets, evidence was found for a long-term increase in stratospheric H_2O by $1\,\%\,\mathrm{yr}^{-1}$ ($0.05\,\mathrm{ppmv}\,\mathrm{yr}^{-1}$) between 1964 and 2000 (Oltmans and Hofmann, 1995; Rosenlof and Kley, 2001; Nedoluha et al., 2003), which has ceased in the beginning of this century (Solomon et al., 2010) and resumed to increase after 2005 (Hurst et al., 2011). However, the expected correlated increase of TTL temperatures by $2-4\,\mathrm{K}$ was not observed (Seidel et al., 2001). Such inconsistencies not only cast doubt on the completeness of the theory, but an overestimation of the trend in water vapor concentration is also considered a possible explanation (Fueglistaler and Haynes, 2005). Despite the availability of satellite-based observations during the last three decades, persisting deviations among in-situ and remote measurements continue to limit the validation of theoretical concepts that describe the control of UTLS humidity (Fueglistaler et al., 2013).

The measurement of local supersaturations of 60 % outside and 30 % inside high-altitude cirrus clouds (Jensen et al., 2005; Peter et al., 2006) represents another observation that contradicts the current understanding of cloud formation processes and questions the accuracy of the underlying data (Krämer et al., 2009). The accurate description of cloud formation and dehydration processes is important for the comprehension of stratospheric humidity. In fact, the observed water vapor abundance in the stratosphere is generally too low to be solely explained by the zonally averaged TTL temperatures. This indicates preferential injection sites with exceptionally strong dehydration which need to be adequately parameterized in modeling codes (Rosenlof, 2015).

In summary, the main open questions concerning UTLS water vapor involve (*i*) the determination of the exact mechanisms that control the water vapor budget in the stratosphere and (*ii*) unraveling the distribution of humidity in and around cirrus clouds, due to its strong impact on stratospheric chemistry and radiative balance (Weinstock et al., 2009). However, unless the uncertainty of the measurement is significantly reduced, the understanding of the contributing processes is limited (Kley et al., 2000), causing relevant uncertainty to projections of the climate evolution (Harries, 1997).

1.3 Measurement of Water Vapor in the UTLS

Measurements of UTLS water vapor are either performed by in-situ or remote sensing techniques. Thereby, a trade-off between global coverage and vertical resolution

has to be considered: While ground based water vapour LIDAR reach an accuracy better than 10 % (Kley et al., 2000), they suffer from generally limited resolution in the upper troposphere and weather dependent probing distances (Kämpfer, 2013). Satellite-borne systems have a broad coverage, but generally limited vertical resolution. Highest spatial resolution can only be obtained by in-situ probing. However, accurate and high-resolution measurements in the UTLS are challenging. The main difficulty arises from the strong vertical profile of water vapor partial pressure in the troposphere that spans over five orders of magnitude. Water, as a highly polar molecule, tends to adsorb to surfaces, from where it eventually desorbs at lower pressure or increased surface temperature, potentially leading to contamination of the measurement. In addition, the harsh and rapidly changing environmental conditions ($1 > p > 20\,\mathrm{hPa}$ and $280 > T > 210\,\mathrm{K}$) may induce changes to the sounding system and, thus, to errors in the retrieved data.

1.3.1 In-situ Measurement Techniques

Currently, there are three techniques for the specific in-situ measurement of UTLS water vapor that provide acceptable performance.

Frost/dew point hygrometry detects the temperature corresponding to 100 % relative humidity (frost/dew point) by maintaining a constant layer of condensate on the surface of a chilled mirror. The mirror temperature is controlled by an optical feedback. From the mirror temperature and the ambient pressure, the specific humidity can be calculated using empirical relations for the saturation vapor pressure as function of the temperature. The technique relies on the assumptions that the condensation layer achieves equilibrium with the ambient water vapor, that the mirror remains uncontaminated, and that its temperature is known with high accuracy (Smith, 2015). In combination with an inherent delay of the temperature feedback, the response time of sudden humidity changes can amount up to tens of seconds at low partial pressures of H_2O (Busen and Buck, 1995). The instruments FPH (Mastenbrook and Oltmans, 1983) and CFH (Vömel et al., 2007) are specific integrations of this method, tailored for balloon-borne measurements in the UTLS. Significant efforts were made to understand, eliminate and correct all the error sources of this measurement technique (Vömel et al., 2016; Hall et al., 2016). An accuracy of 6 % in the stratosphere is reported, although, the nature of increasing humidity values above ca. 27 km altitude is currently a matter of debate (Brunamonti et al., 2018). The relatively low costs and the lightweight construction make FPH/CFH the preferred instruments for balloon-borne soundings. However, the liquid cooling agent (HFC-23, CHF_3) required for their operation is to be phased out due to its strong global warming potential of 14,800 (UNEP, 2016). Alternative approaches based on thermoelectric cooling are currently under development (Sugidachi, 2018; Jorge, 2019).

Lyman-α (fluorescence) technique. This approach uses ultraviolet radiation (UV; Lyman-α transition) to dissociate water molecules. Thereby, excited hydroxyl radicals (OH*) are produced. The fluorescence radiation emitted upon decay of this excitation is proportional to the amount of present H_2O molecules. This proportion-

ality constant, however, has to be determined empirically in a calibration procedure. If the UV-source is held stable and all other sources of transient UV-radiation are efficiently blocked, this method provides accurate and fast (>1 Hz) measurements even at high altitude (Smith, 2015). Since Lyman-α-based instruments are generally weight-expensive and power demanding, they are often deployed aboard of special aircrafts (Sargent et al., 2013; Meyer et al., 2015). FLASH-B is a lightweight, balloon-capable integration of the Lyman-α-technique (Lykov et al., 2011), providing an uncertainty of $< 10\,\%$. Its open-path detection mode, however, restricts the deployment to nighttime.

Laser absorption spectroscopy is widely used for the contact-free trace gas quantification at low concentration (McManus, 2010; Curl et al., 2010). Its principles are discussed in detail in Ch. 2. The advantage lies in the fast acquisition rates, the high molecular specificity and the possibility to measure without (frequent) calibration. The sensitive optics and electronics used in absorption spectrometers require high mechanical and thermal stability, which is challenging to maintain in the UTLS. Therefore, these instruments tend to be bulky, and due to their weight and power consumption, they are currently carried by aircraft (Silver and Hovde, 1994; Sonnenfroh et al., 1998; May, 1998; Diskin et al., 2002; Zondlo et al., 2010; Thornberry et al., 2015; Buchholz et al., 2017) or special high-volume balloons (Durry and Megie, 2000; Moreau et al., 2005; Gurlit et al., 2005; Durry et al., 2008). Hence, this technique is mainly deployed in the course of expensive and elaborate campaigns, which hinders the frequent data collection. Laser absorption spectrometer concepts can be divided into *open-path*, where the gas is sampled under ambient conditions, and *closed-path*, comprising a measurement cavity usually held at constant pressure. Given the enhanced stickiness of the H_2O molecule, closed-path concepts tend to suffer from increased reaction times and hysteresis (Rollins et al., 2014).

1.3.2 Performance

In the year 2000, a comprehensive assessment of water vapor observations revealed significant deviations among different techniques and instruments: In the UTLS, discrepancies of more than 20 % were found among several instruments (Kley et al., 2000). These deviations motivated the first AquaVIT-campaign in 2007, which was a blind intercomparison of multiple state-of-the-art in-situ water vapor instruments, all deployed in – or connected to – the same climate chamber (Fahey et al., 2014). Fair agreement was found among the defined ensemble of 'core-instruments', i.e. deviations of $\pm 10\,\%$ and $\pm 20\,\%$ in the range of $10 - 150\,\mathrm{ppmv}$ and $1 - 10\,\mathrm{ppmv}$, respectively, relative to the ensemble mean. The reported results led to the conclusion that, in principle, the accurate measurement of water vapor – especially by means of absorption spectroscopy – is feasible, although, special care must be taken upon integration of these devices into a portable system due to contamination resulting from desorbing H_2O. Indeed, the MACPEX in-flight intercomparison study in 2011 (Rollins et al., 2014) reported again higher differences of up to 20 % ($\pm 0.8\,\mathrm{ppmv}$) among the tested instruments at the tropopause, suggesting contamination and surface desorption to be a major source of uncertainty. However, the deviation may also be attributed to

differences in the calibration of the instruments, which is a delicate process: Due to the pronounced adhesion properties of H_2O, there is no SI-traceable transfer standard against which the instruments could be calibrated (Buchholz and Ebert, 2018). Thus, uncertainties of the calibration reference can limit an otherwise highly precise measurement.

Lack of an established reference method, numerous comparison campaigns were conducted within the last decades (Kämpfer, 2013, p. 263 et seqq.). Due to persisting disagreements and yet no obvious candidate for a standard instrumentation, the fourth edition of AquaVIT is scheduled for September 2020. The recurring activities for comprehensive intercomparisons underscores both the importance and the difficulty of acquiring comparable and accurate water vapor measurements in the UTLS.

1.4 Aim of this Project

Progress in clarifying the open questions stated in Sec. 1.2 requires frequent and accurate in-situ water vapor measurements with high spatial resolution in the UTLS (Whiteman et al., 2011; Müller et al., 2016). With regard to the current ambiguities in the trend and feedback analysis of UTLS water vapor and the open questions concerning the formation of high-altitude cirrus clouds, an in-situ water vapor instrument that fulfills the following requirements would provide valuable data for additional insights:

(*i*) The acquired data must be free of instrumental drift to allow long-term comparability and trend analysis (precision).
(*ii*) In addition to a relative consistency, the quantitative investigation of, e.g., the radiation budget or cloud formation processes, requires the knowledge of the absolute concentration. Therefore, the H_2O abundance should be measured with high accuracy – best contemporary instruments reach uncertainties of $5-10\,\%$ (i.e. $0.2-0.4\,\mathrm{ppmv}$) in the UTLS (Kämpfer, 2013). Ideally, this performance is achieved by calibration-free and fully SI-traceable measurements. This requires that the amount of water vapor is derived using only measurable quantities within the framework of the SI-unit system, without the need to introduce empirical constants to match the result with a reference.
(*iii*) The temporal resolution should be 1 Hz or faster, which enables a vertical resolution of a few meters even upon descent on a parachute.
(*iv*) The instrument should be compact and lightweight to enable frequent and flexible deployments aboard of low-volume meteorological balloons without the need for special permission. This constrains the total mass of the payload according to the local legislation, e.g., $\leq 4.5\,\mathrm{kg}$ in Germany, $\leq 2\,\mathrm{kg}$ in Switzerland (VLK Art. 16, 1994).

This work is intended to contribute to the understanding of UTLS water vapor and its long-term variation by the development of an instrument that fulfills the requirements (*i*)-(*iv*). It challenges the currently available instrumentation by the combina-

tion of accuracy, traceability, and deployment flexibility – properties that appeared exclusive in the past. This is achieved by exploring the potential of miniaturization in laser absorption spectroscopy, aiming towards an autonomous balloon-borne instrument for highly accurate and high-resolution UTLS water vapor measurement. Such instrumentation likely supplements – and potentially substitutes – the currently most often used method of frost point hygrometry.

1.4.1 Strategy

This target is accomplished by developing a compact quantum cascade laser (direct) absorption spectrometer (QCLAS), since this technique is known for achieving high accuracy, high temporal resolution, long-term comparability, and the possibility of calibration-free operation. However, a fully autonomous balloon-borne deployment requires an unprecedented miniaturization, temperature stabilization as well as the integration of the necessary electronics. This is achieved by reconsideration of the setup compared to traditional laboratory-based spectrometer designs. So far, no direct absorption spectrometer has ever been deployed in the stratosphere aboard of a low-volume meteorological balloon. Given the particular difficulty to accurately measure water vapor in the UTLS ($8 - 20\,\mathrm{km}$ altitude), this region is defined as a first priority and the instrument is designed accordingly.

The spectrometer is constructed for open-path measurement, i.e., at ambient conditions without the use of a closed pressure-stabilized sample volume. This not only reduces weight, it also minimizes the surface contact of the measured air, e.g., with tubing, pump, etc., thereby inhibiting potential contamination by desorbing H_2O molecules. Additional compactness is achieved by measuring in the mid-infrared spectral region, where H_2O exhibits strong fundamental transitions. H_2O absorption lines in the mid-IR are about 20 times stronger than transitions in the near-IR, which is commonly used for H_2O measurements (e.g., Durry et al. (2008)). The inexistence of adequate multipass cells (MPC), led to the development of a novel class of multipass optics, called the *segmented circular multipass cell* (SC-MPC), which is especially suited for compact and lightweight spectrometers. To ensure stable operation of the electronics even at UTLS conditions, a thermal stabilization system is integrated, based on a combination of phase-change material (PCM) and thermoelectric cooling (TEC). Moreover, dedicated data acquisition hardware and software are incorporated, including custom-developed laser driving electronics that enable the autonomous and energy-saving operation.

Laboratory-based characterizations are conducted to reveal the performance of the instrument at various conditions. These experiments finally culminate in the balloon-borne deployment of the QCLAS in the stratosphere alongside of a CFH instrument.

1.4.2 Structure

This thesis commences with an introduction to direct laser absorption spectroscopy. With regard to the importance of suitable multipass cells (MPC) for the accurate and miniaturized trace-gas detection, Chapter 3 focuses on the development and

evaluation of compact and lightweight MPCs. This work has been published in peer-reviewed journals (Graf et al., 2017, 2018). Chapter 4 describes the incorporation of the established concepts into an integrated, autonomously operating instrument for balloon-borne measurements of water vapor in the UTLS. Chapter 5 discusses the laboratory-based characterization experiments as well as the first flight campaign. Suggestions for further improvements are closing this chapter. In the final chapter, the findings of this work are summarized and classified.

Chapter 2

Laser Absorption Spectroscopy

The physical phenomenon of *absorption* due to the interaction of light and matter is widely used for the measurement of gas quantities. This chapter briefly reviews the technique and the theoretical foundations of *direct absorption spectroscopy* using tunable lasers. Moreover, it describes the application of this method for calibration-free trace gas measurements.

Individual sections of this chapter are published in the peer-reviewed journal *Atmospheric Measurement Techniques* (EGU, Copernicus), Graf et al. (2020).

2.1 Radiative Transfer and the Beer-Lambert Law

When light quanta travel through matter, they are scattered or absorbed by molecules or particles along their trajectory. The mathematical formulation describing the effective transmission of radiation through a gas or material is known as the *radiative transfer equation* (Chandrasekhar, 1960). The calculation is often complicated and requires numerical methods. Its time-independent form in one dimension is given by

$$\frac{1}{n}\frac{\mathrm{d}I}{\mathrm{d}z} = -(\kappa + \alpha)I + j \tag{2.1}$$

where I is the specific intensity of the light, κ and α denote absorption and scattering coefficients, respectively; and j is the emission coefficient of the material at non-zero temperatures.

For monochromatic light, negligible thermal emission of the material, and for gases with homogeneously distributed molecules acting as absorbents ($\alpha = 0$, $\kappa(z) = \text{const.}$), Eq. 2.1 has a simple solution known as the *Beer-Lambert law*:

$$I_z(\tilde{\nu}) = I_0(\tilde{\nu}) \exp(-nz\sigma(\tilde{\nu})) \tag{2.2}$$

where $n\sigma(\tilde{\nu}) = \kappa$ and z denotes the optical path length (OPL) within the absorbing medium. Hence, the attenuation of radiation occurs exponentially with distance and is dependent on the number of absorbing molecules per volume ($n = N/\tilde{V}$; number density) and their ability to absorb radiation at the particular wavenumber $\tilde{\nu}$ of the incoming radiation. This 'ability' is parameterized by the monochromatic absorption coefficient $\sigma(\tilde{\nu})$. Thus, if the wavelength of the incoming radiation and $\sigma(\tilde{\nu})$ of the absorbing molecules are known, their number density can be determined by comparing the incoming intensity $I_0(\tilde{\nu})$ at $z = 0$ with the transmitted intensity $I_z(\tilde{\nu})$ after an interaction path length of z. Furthermore, if pressure p and temperature T of the analyzed gas are known, the *amount fraction* χ_s of the absorbing molecule of type s can be calculated using the ideal gas law $n_{\text{tot}} = N/\tilde{V} = p/(k_B T)$:

$$\chi_s = \frac{n_s}{n_{\text{tot}}} = \frac{k_B T}{pzS} \int \ln \frac{I_0(\tilde{\nu})}{I_z(\tilde{\nu})} \mathrm{d}\tilde{\nu} \tag{2.3}$$

with the absorption line intensity $S = \int \sigma \mathrm{d}\tilde{\nu}$. The amount fraction χ_s is dimensionless denoting µmol of absorbents per mol of total molecules – the pseudo-unit *parts-per-million by volume* (ppmv) is commonly used.

It is important to note that Eq. 2.3 establishes a fully defined relation between the (unknown) amount fraction and the (measured) integrated absorbance $\int \ln \frac{I_0(\tilde{\nu})}{I_z(\tilde{\nu})} \mathrm{d}\tilde{\nu}$. The relation only comprises physical constants (k_B), directly measurable quantities (T, p, z, I_z), and molecular properties (S; see next section). This renders tunable laser direct absorption spectroscopy a potentially *calibration-free* method to determine the amount fraction of trace gases.

2.2 Rovibrational Transitions

A crucial parameter for the quantitative interpretation of absorption phenomena is the monochromatic absorption coefficient $\sigma(\tilde{\nu})$, generally defined as

$$\sigma(\tilde{\nu}) = S\Phi(\tilde{\nu} - \tilde{\nu}_{ij}) \tag{2.4}$$

In order to understand its magnitude S and distribution Φ, some details about molecular absorption of photons (photoexcitation) are required which are discussed in this section.

Apart from the translational motion of an entire molecule, its individual atoms exhibit intramolecular motion, i.e., vibration and rotation, due to thermal energy. The latter movements are quantized, thus, having specific energy levels, as schematically depicted in Fig. 2.1(a). Molecules with nonzero dipole moment can change their rotational or vibrational energy level by the absorption of a photon. Such an excitation obeys the quantum mechanical selection rules and requires the photon energy to exactly match the difference between the actual and a higher energy level. Otherwise the photon is transmitted without interaction. This explains the isolated dips in a transmission spectrum of e.g., a CO-molecule, as presented in Fig. 2.1(b). The individual dips are referred to as *absorption lines*. Even though the transition

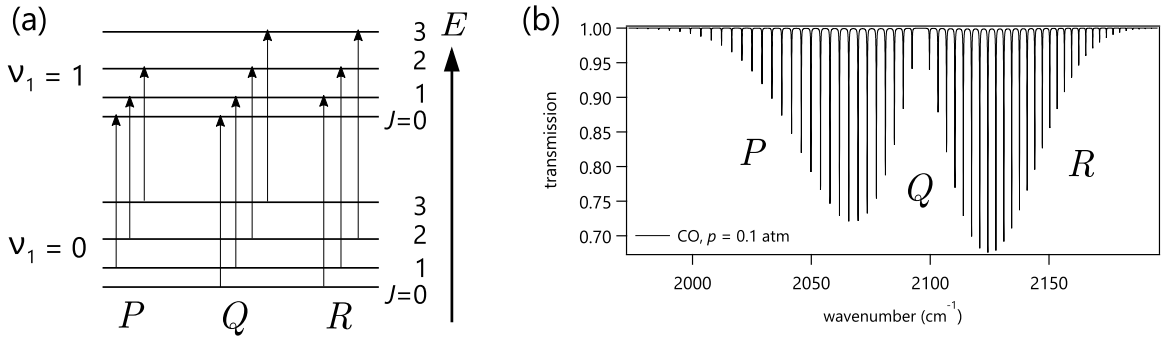

Figure 2.1: (a) Rotational and vibrational states denoted with the quantum numbers $\nu_1 = 0, 1...$ and $J = 0, 1...$, respectively. Transitions with $\Delta J = -1$ give rise to the P-branch, $\Delta J = +1$ to the R-branch, and $\Delta J = 0$ to the Q-branch. (b) Broadband rovibrational spectrum of carbon monoxide (CO) at low pressure. According to the symmetry of the CO-molecule and the corresponding selection rules, transitions with $\Delta J = 0$ are impossible, thus, no Q-branch is observed.

happens between two formally discrete energy levels, the absorption feature is not strictly monochromatic. The reason for the absorption features not being infinitesimally narrow lies in several broadening mechanisms:

Natural/lifetime broadening. As a result of the quantum nature of a molecule, the excited state has an energy uncertainty ΔE inversely proportional to its lifetime $\tau \approx \hbar/\Delta E$. Lifetime broadening can be described by a Lorentzian function of width

$\gamma = \tau/(2\pi)$. Unperturbed rovibrational excitations have lifetimes in the order of milliseconds (Kneubühl and Sigrist, 2013), leading to negligible energy uncertainty relative to other broadening mechanisms.

Doppler broadening. The translational motion of the molecules leads to a slight change of the effective wavelength seen by the molecule in its rest-frame. This phenomenon does not impact the effective energy levels of the molecule, but it nevertheless broadens the absorption feature: A photon with wavelength slightly above the effective transition energy, is blue-shifted for molecules moving towards the light source potentially being absorbed. Following Maxwell-Boltzmann statistics to describe the velocity distribution of the molecules, this results in a Gaussian broadening of the absorption line with a half width at half maximum (HWHM, α) proportional to the square-root of the gas temperature.

Collisional broadening. Intermolecular collisions lead to shifts in the molecular energy levels due to influences of the atomic potentials onto the collision partner. To first order, this broadening has Lorentzian distribution with a broadening parameter which is pressure-dependent. Different energy levels are influenced differently by collisions, therefore, the broadening parameter varies among the transitions. Moreover, the broadening is dependent on the collision partner: The impact is different for collisions with molecules of the same kind (self-broadening) than for collisions with molecules from the gas matrix (foreign-broadening). For trace gas spectroscopy, self-broadening is usually neglected due to the low amount of absorbing species; however, for H_2O, this is not always a valid simplification. The HWHM of the Lorentzian describing the collision-related broadening is composed by

$$\gamma(p,T) = \left(\frac{T_{\text{ref}}}{T}\right)^{n_{\text{air}}} ((p-p_p)\gamma_{0,\text{air}} + p_p\gamma_{0,\text{self}}) \tag{2.5}$$

with the factor $\left(\frac{T_{\text{ref}}}{T}\right)^{n_{\text{air}}}$ describing the gas temperature dependence, p the gas pressure, and p_p the partial pressure of the species under study. The broadening parameters $\gamma_{0,\text{air}}$ and $\gamma_{0,\text{self}}$ are found in a spectral database (e.g., HITRAN (Gordon et al., 2017)) for $p_{\text{ref}} = 1013.25$ hPa and $T_{\text{air}} = 296\ K$ and are linearly scaled with pressure.

2.2.1 Voigt Profile

Given the above effects, the line broadening function Φ for a rovibrational transition can be described by a convolution of a Gaussian and a Lorentzian distribution, generally referred to as a Voigt profile. Efficient strategies for its numerical calculation can be found in the literature (Humlíček, 1982). Alternatively, the Faddeeva-function $w(z)$ is utilized, which makes use of the complex error-function, and is available in the Python-SciPy-library (SciPyCommunity).

$$V(\tilde{\nu};\alpha,\gamma) = G(\tilde{\nu};\alpha) * L(\tilde{\nu};\gamma) = \sqrt{\frac{\ln(2)}{\pi}}\frac{\text{Re}[w(y)]}{\alpha} \quad \text{with} \quad y = \frac{\sqrt{\ln(2)}}{\alpha}(\tilde{\nu} - \tilde{\nu}_{ij} + i\gamma) \tag{2.6}$$

Therefore, the monochromatic absorption coefficient σ can be written as

$$\sigma(\tilde{\nu}) = S_{ij}(T)V(\tilde{\nu}; \alpha(T), \gamma(p,T)) \quad \text{with} \quad \int V(\tilde{\nu})\,\mathrm{d}\tilde{\nu} = 1 \tag{2.7}$$

The spectral line intensity $S_{ij}(T)$ is a measure for the probability of the transition $i \leftarrow j$ to take place and defines the magnitude of the absorption coefficient, i.e. the area underneath the absorption feature. $S_{ij}(T)$ is proportional to the Einstein-coefficient A_{ij} for spontaneous emission, assigned to a particular transition. $S_{ij}(T)$ is moreover scaled with the statistical weight and degeneracy of the involved states. This includes the population of the involved states at a given gas temperature T, defined by the partition function. Detailed mathematical formulation can be found in the literature (HITRAN, 2020). Parameters $S_{ij}(T_{\mathrm{ref}}), \gamma_{\mathrm{self}}, \gamma_{\mathrm{air}}$, the spectral line position ν_{ij}, as well as the partition function are listed in the HITRAN database. Hence, if p, T are known, the absorption coefficient σ is fully defined.

2.2.2 Higher Order Line Profiles

With increasing resolution of the spectrometers, inadequacies of the Voigt profile have been revealed, implying the existence of additional broadening effects that are not included in the above description: Changes of molecular velocity due to collisions reduce the Doppler broadening, resulting in collisional (or Dicke) narrowing (Dicke, 1953). Moreover, the collisional broadening parameter exhibits a speed-dependence that alters the Lorentzian line shape (Ngo et al., 2013).

In pressure-stabilized closed-path spectrometers, such a mismatch of the Voigt profile with respect to the measured spectrum is generally eliminated by a calibration measurement of a known reference gas. However, in the context of an open-path instrument, which is exposed to gradually changing pressures, this strategy is not applicable. Therefore, the accurate interpretation of the spectra should include these higher order effects. In the literature, more sophisticated line profiles are described (Galatry, 1961; Rautian and Sobel'man, 1967; Berman, 1972) that take into account the effect of collisional narrowing and speed-dependence. However, the associated coefficient(s) that parameterize these phenomena need to be determined experimentally beforehand, and are not (yet) available for H_2O in the spectral region under study. Until this is done, the uncertainty induced by the limited complexity of the Voigt profile, has to be included in the error budget. By using the Voigt profile, Lisak et al. (Lisak et al., 2015) have identified deviations in the retrieved integrated absorbance by up to 5 % with respect to more sophisticated line profiles. The authors compare the fitting results with various profiles for H_2O perturbed by N_2 in the near-IR for different partial pressures of the matrix gas. They furthermore found the deviations to depend on the involved energy states of the transition, which makes it difficult to estimate the uncertainty in other spectral regions based on these results.

2.3 Direct Absorption Spectroscopy

The absoption of radiation due to rovibrational transitions can be directly probed by tuning a narrowband laser source across an absorption line while measuring the transmitted light intensity. Spectral tuning of the laser is achieved by changing the operating current or the heat-sink temperature. During this scan, the output of the laser neither shows constant emission intensity $\frac{dI_0}{dt}$ nor constant tuning rate $\frac{d\tilde{\nu}}{dt}$. This has important consequences for spectroscopic analysis: In order to convert the raw detector signal $I_z(t)$ shown in Fig. 2.2(a)) into an absorption spectrum, several preparation steps are required. This section reviews the generic procedure. Depending on the experiment, additional actions may apply, which are discussed in more details in the corresponding sections of Ch. 5.

Given the variable intensity and tuning rate, but constant sampling rate, the Beer-Lambert law (Eq. 2.2) is extended to contain the intensity as measured on the detector as function of *time* $I_z(t)$:

$$\int \ln\left(\frac{I_z(t)}{I_b(t)}\right) \frac{\mathrm{d}\tilde{\nu}}{\mathrm{d}t}\mathrm{d}t = -nz \int \sigma(\tilde{\nu}; p, T)\, \mathrm{d}\tilde{\nu} \tag{2.8}$$

$\frac{\mathrm{d}\tilde{\nu}}{\mathrm{d}t}$ denotes the spectral tuning rate and translates the spectrum from the time domain into the wavenumber domain. The tuning rate is determined by the evaluation of the Airy-signal generated by guiding the laser beam through a Fabry-Pérot etalon (Fig. 2.2(a)). The resulting self-interference yields intensity oscillations equidistant in wavenumbers. The distance between two maxima, the free spectral range $\Delta\tilde{\nu}_{\mathrm{FSR}}$, is defined by: $\Delta\tilde{\nu}_{\mathrm{FSR}} = (2Ln_g)^{-1}$ with n_g being the group refractive index and L the length of the etalon. After determining the exact position of the extrema, the relative tuning curve $\frac{\mathrm{d}\tilde{\nu}}{\mathrm{d}t}$ can be determined by a polynomial of sufficiently high order. $I_b(t)$ denotes the zero-absorption baseline (termed *baseline* in the following) corresponding to the measured intensity *without* any target species. In closed cell setups and for gases which can be effectively removed from the sampling volume, I_b is regularly recorded after evacuation, or flushing of the sample cell with absorbent-free gas. In open-path configuration, however, I_b is not directly accessible. Therefore, $I_b(\tilde{\nu})$ is reconstructed as part of the fitting procedure. Although it may be challenging to separate the baseline $I_b(\tilde{\nu})$ from the data in some cases, it has a major advantage: Compared to the initial intensity $I_0(\tilde{\nu})$ in Eq. 2.2, $I_b(\tilde{\nu})$ already includes broadband intensity losses due to aerosols, particles, or limited reflectivity of mirrors. Hence, only the absorption due to H_2O molecules contributes to the *effective absorbance* $\ln(I_z/I_b)$.

In this work, the fitting of the absorption feature is performed using the Levenberg-Marquardt least-squares algorithm. To parameterize the monochromatic absorption coefficient $\sigma(\tilde{\nu}; p, T)$, a Voigt profile (Eq. 2.6) is utilized. The corresponding intensity and broadening parameters are taken from the HITRAN2016 database (Gordon et al., 2017), whereas the gas pressure p and temperature T are measured. Measured values are either kept constant or constrained within their measurement uncertainty. This leads to only one remaining free parameter associated with absorption line, i.e.,

the number density n. Additionally, $I_b(\tilde{\nu})$ is reconstructed by a polynomial $P_N(\tilde{\nu})$ of the order three to six, depending on the spectral range to be fitted. Therefore, the determination of the baseline $I_b(\tilde{\nu})$ adds further free parameters to the fit.

According to Eq. 2.8, the relevant spectral information used to retrieve the amount fraction, is contained in the effective absorbance, i.e. $\ln(I_z/I_b)$. Thus, the limiting aspect for the detection of very small effective absorbances is the signal-to-noise ratio (SNR). For a given absorption line, the SNR can be enhanced either by a reduction of the noise, or by enlarging the OPL, e.g, by the use of a multipass cell (MPC).

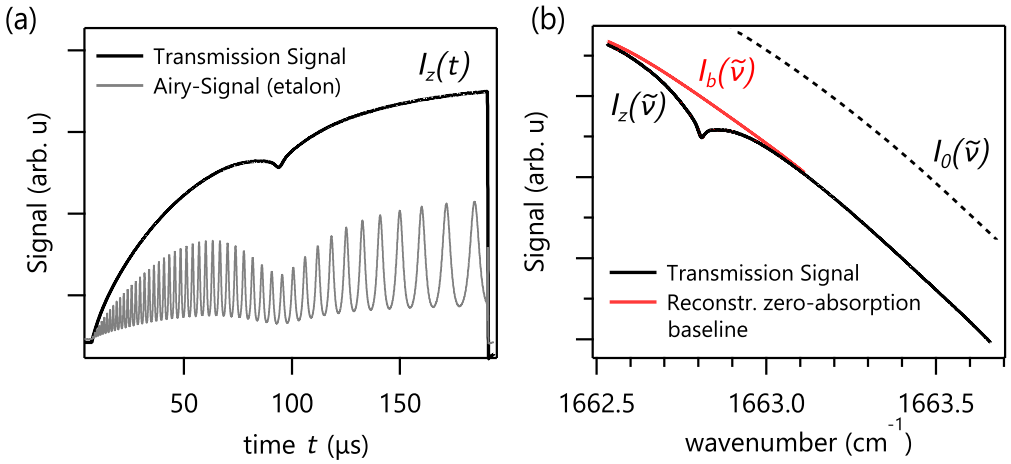

Figure 2.2: (a) The raw radiation intensity signal as seen by the detector through the MPC (black) and through a Fabry-Pérot-etalon (gray). The Airy signal is used to calibrate the wavenumber scaling. (b) After application of the wavenumber scaling, the absorption line is fitted onto a subset of the data. Thereby, the baseline $I_b(\tilde{\nu})$ is reconstructed, which, in contrast to the laser output intensity $I_0(\tilde{\nu})$, already includes broadband absorption losses.

Chapter 3

Multipass Cell Design

For the detection of very low concentrations of a target molecule, the optical interaction path length of an absorption spectrometer is usually enhanced by a multipass cell (MPC). Various designs and concepts exist to accomplish this task, however, very few of those are suitable for lightweight and mobile applications. Within an MPC, it is of highest importance that the beam remains well-confined and the generation of stray light is minimized. Given the long coherence length of the laser radiation, such spurious portions of radiation can superpose with the main beam on the detector, thereby creating interference. As the wavelength is tuned, the varied phase difference between the stray light and the main beam manifests as oscillations on the measured signal. These oscillations are referred to as *fringes*, having a negative impact on the precision of a spectrometer. Therefore, a significant part of this project is dedicated to the research and development of a suitable multipass cell that allows the optically stable and efficient path length enhancement even under harsh environmental conditions.

3.1 Beam Folding Analysis and Optimization of Mask-Enhanced Toroidal Multipass Cells

Mask-enhanced toroidal MPCs, as proposed by Tuzson et al. (2013), have been applied in relatively compact devices (Mangold et al., 2016; Hundt et al., 2018). However, the efficient coupling of a laser beam to these MPCs is very sensitive: Mismatches in the beam shaping and alignment strongly affect the transmitted intensity. Even more problematic is the use of a beam-clipping mask within the sampling volume: For a strongly adhesive molecule like water vapor, this is a serious limitation.
While developing a more fundamental solution to the problem of controlled beam folding, the idea of toroidal MPCs was pursued as a fallback scenario. The idea was to substitute the internal mask by selective coating of absorbing zones on the reflective surface, or even by removal of the non-reflective sections. In order to efficiently use such toroidal MPCs and to optimize the design process, this concept has been investigated in-depth, both in theory and by explicit simulation.

The content of this section is based on the manuscript published in the peer-reviewed journal *Optics Letters* (OSA), Graf et al. (2017).

3.1.1 Abstract

We present computational and experimental investigations of the beam folding properties and fringe suppression capabilities in monolithic toroidal multipass cells when combined with absorption masks. Coherent field simulations based on Fresnel-Huygens theory were performed to understand the effect of multiple field truncations in such an optically semi-unstable mirror arrangement. The explicit numerical calculation of the radiation field at each reflection allows detailed optimization and performance analysis. We experimentally verified the evolving irradiance distributions and identified optimal initial field configurations. Furthermore, we suggest a proxy to estimate the noise level for specific initial conditions. These insights pave the way to a better optical performance and thus to even more lightweight and compact designs of this multipass cell type.

3.1.2 Introduction

Trace gas analysis by means of direct absorption spectroscopy is a widely used technique and currently advances towards highly compact and mobile applications. High precision measurements at low mixing ratios require the extension of the optical path through the sampling volume, typically by means of a multipass cell (MPC). Driven by their mechanical simplicity, the most frequently applied concepts are all based on a coaxial arrangement of two mirrors (Herriott et al., 1964), while specific mirror curvatures enhance the beam folding density (McManus et al., 1995; Silver, 2005). Motivated by the demand for portable and lightweight instrumentation, the concept of monolithic toroidal MPC has been proposed (Tuzson et al., 2013). These cells can

be designed very compact and versatile. Moreover, they are expected to operate well even under harsh environmental conditions, as their rotational symmetry enhances the tolerance against optical misalignment and pattern variation. In addition, the monolithic construction makes this concept exceptionally attractive for both mobile and mass-critical applications. Recently, toroidal MPCs were successfully applied in high precision atmospheric NO_2 measurements (Mangold et al., 2016; Hundt et al., 2018) and real-time breath gas analysis (Ghorbani and Schmidt, 2017). The reported sub-ppb analytical precision, however, could only be achieved by inserting an aperture mask in the cell volume as schematically depicted in Fig. 3.1(a). Empirical investigations of such mask-enhanced toroidal multipass cells (MET-MPC) showed that this approach effectively reduces the optical fringe-noise. However, neither the physical reasons for this noise-suppression nor any strategies for further improvement and optimization have yet been reported.

This work presents a computational approach to investigate the beam folding properties of such MET-MPCs. Extensive numerical simulation are performed to elucidate the key factors determining the optical performance of this type of MPC. We discuss the intensity evolution characteristics for varying initial conditions as well as their potential impact on the noise level.

3.1.3 Mask-Enhanced Toroidal MPC

The constructional concept of a toroidal multipass cell has been described in detail elsewhere (Mangold et al., 2016). Therefore, only the relevant elements for the subsequent stability discussion are briefly summarized here. The principle of toroidal MPCs is based on the emergence of a N-star polygram when a geometrical ray enters the cell under an angle θ with respect to its radial line (Fig. 3.1b). However, due to their coherent nature, physical laser beams differ from geometrical rays as they have both finite spatial extent and nonzero divergence. Thus, the mirror arrangement of a MPC must be suitable to conserve the beam shape upon many reflections. To investigate the beam stability, the subsequent reflections within a toroidal cell may be considered as a spatially distributed resonator, where each reflection is a few degrees rotated with respect to the center of the MPC. Applying paraxial matrix-methods, one finds the relation between curvature and displacement of mirrors that allows the stable propagation of light over many reflections (Siegman, 1986). The beam stability can be analyzed separately in two perpendicular planes (Li et al., 1966): the horizontal (or tangential, xz) and the vertical (or sagittal, yz) plane as indicated Fig. 3.1(a). The mirror curvature along the vertical axis is unconstrained and can be freely chosen e.g., to fulfill the beam stability criterion, which states that the mirror separation L and their curvature radius R_y must compare as $L < 2R_y$ (e.g., confocal: $R_y = L$). In contrast, the curvature in the horizontal plane is given by the continuous revolution around the central axis of the cell. Hence, in the horizontal plane, the mirror curvature R_x is equal to the cell radius R_c and the distance between the mirrors L of an equivalent resonator is *always* given by $L = 2R_c$. This corresponds to a *concentric* mirror arrangement, which is located at the border of the set of stable solutions in the resonator stability diagram (Siegman, 1986). As a result, Gaussian

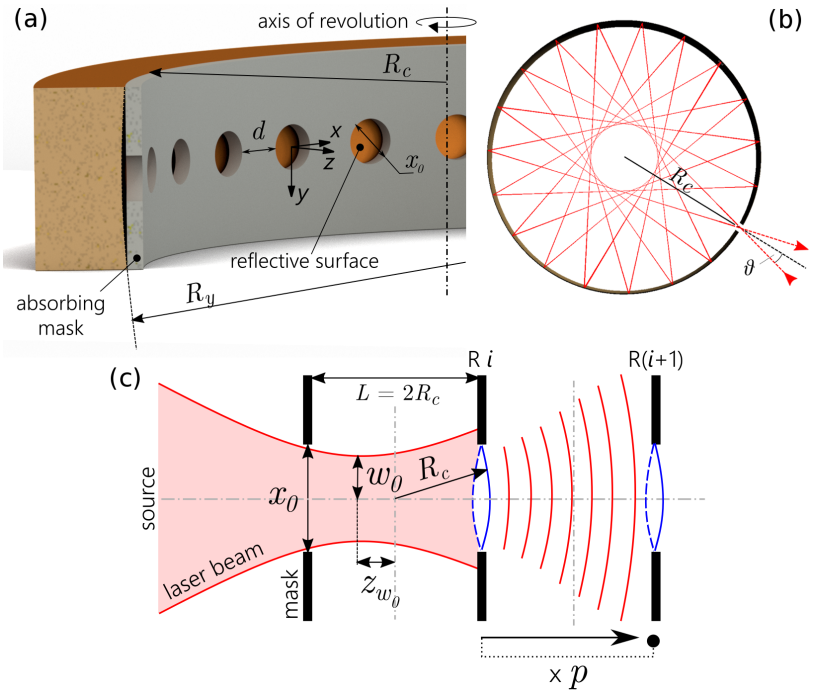

Figure 3.1: (a) Cut through a toroidal cell indicating the main dimensions as well as the local coordinate system at the apertures. (b) Top-view onto the horizontal plane of a toroidal MPC where a geometric ray-trace simulation visualizes the beam path. (c) A schematic of the coherent wave propagation simulation, showing only the horizontal plane. For computation, the reflections in the cell are sequentially unfolded along a single axis: The initial Gaussian beam is focused such that the waist w_0 is located z_{w_0} away from the center of the first pass. After a potential clipping at the very first aperture, the radiation propagates to the opposite side of the cell where it is evaluated. Subsequently, the complex field is reflected on the toroidal mirror as well as truncated at the aperture of diameter x_0, followed by a propagation through free space of length L. The latter steps (truncation – reflection – propagation) are successively repeated p times in order to compute the complex radiation field at each reflection. Each time, the previously calculated field serves as initial distribution for the next pass.

beams of any kind will diverge in the horizontal plane as they are reflected within this geometry. Thus, even after a small number of passes, single reflections cannot anymore be distinguished. In this case, the radiation that is leaving the cell towards the detector corresponds to a superposition of beam components which have experienced different numbers of reflections and thus traveled unequal distances. The resulting phase difference of these components manifests as undesired intensity modulations of the observed signal (fringes) as the laser wavelength is tuned. This effect has been observed experimentally (Tuzson et al., 2013) and it was significantly diminished by the insertion of an aperture-mask, which truncates the beam at each reflection (Mangold et al., 2016). Such a beam truncation not only reduces the transmission, but the successive generation of complicated diffraction patterns limits the ability to calculate beam characteristics and spectroscopic performance.

3.1.4 Explicit Field Simulation

To optimize the relevant dimensions of such a cell, as well as to find the optimal initial field, we simulated the propagation of coherent radiation within the toroidal geometry including a cylindrical mask of circular apertures. This problem is similar to an astigmatic resonator cavity with finite mirror size. Investigation of unstable resonator cavities (Li et al., 1966; Siegman, 1974) revealed the emergence of steady-state solutions after many round-trips, characterizable by the Fresnel-number of the resonator (Fox and Li, 1961). For toroidal MPCs, however, the number of reflections is often too small for a stable mode to establish, and the energy-losses during this convergence process are more important than the properties of the steady state solution itself. Since the field structure depends significantly on the initial wave distribution during convergence, the complex field after each pass has to be calculated explicitly. To simulate the wave propagation within MET-MPCs, we used the com-

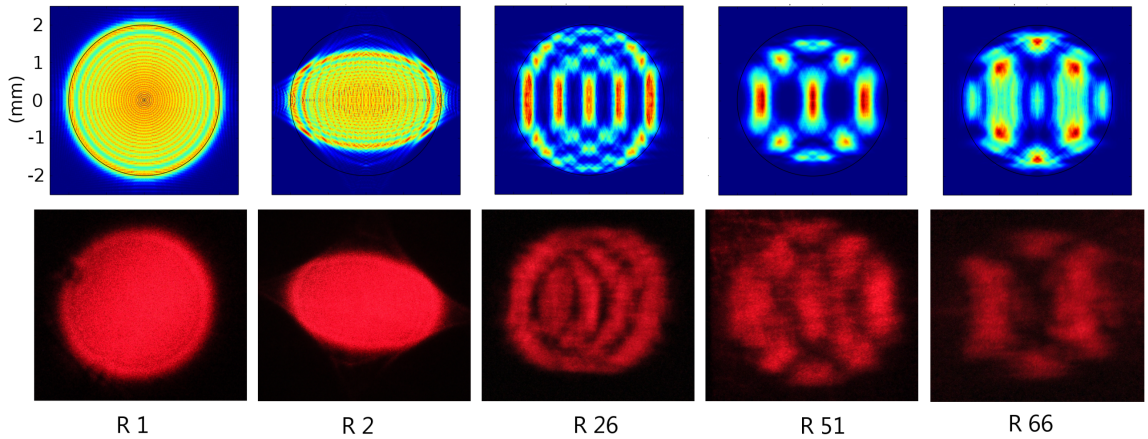

Figure 3.2: (a) Comparison of the calculated (top) and the experimentally observed (bottom) irradiance distributions after different numbers of passes R i. The slight skew and rotation on the photographs is due to the non-perpendicular camera angle.

bination of Fresnel-Huygens (FH) theory with the paraxial ABCD-matrix formalism, allowing the propagation of arbitrary radiation fields within the limits of the Fresnel-approximation (Siegman, 1986). Since both cell- and aperture-diameter are large compared to the wavelength λ, the Fresnel-approximation is generally fulfilled for any geometry of practical interest. According to the FH-principle, the complex radiation field u_{i+1} is described as the superposition of waves emerging from each point of an earlier wavefront u_i:

$$u_{i+1}(\mathbf{r}_2) = \frac{i}{|\mathbf{B}|^{1/2}\lambda} \int_{-x_0/2}^{x_0/2} K(\mathbf{r}_1, \mathbf{r}_2) u_i(\mathbf{r}_1) \mathrm{d}\mathbf{r}_1 \tag{3.1}$$

The effective optical distance of each of these waves is accounted for by adapting the FH-kernel $K(\mathbf{r}_1, \mathbf{r}_2)$ with the entries of the ABCD-matrix for the corresponding optical system. The astigmatic mirror curvature in two dimensions is described by a 4×4-matrix consisting of the four 2×2-matrices $\mathbf{A}$, $\mathbf{B}$, $\mathbf{C}$, $\mathbf{D}$, each containing the entries for both dimensions on their diagonal (cf. Eq. 3.2) (Siegman, 1986; Nazarathy and Shamir, 1982). The numerical solving of the FH-integral (Eq. 3.1) for arbitrary systems on a Cartesian grid was implemented in Python.

Within MET-MPCs, the radiation is reflected on the concave astigmatic mirror with $R_x = R_c$ and R_y. At the same time, the aperture truncates the field, which is realized by setting the absorbed field-values to zero. Subsequently, the remaining radiation propagates through free space of length L, as illustrated in Fig. 3.1(c). Therefore, in one dimension, the ABCD-matrix describing this optical system is given by

$$M = \begin{bmatrix} 1 & L \\ 0 & 1 \end{bmatrix} \begin{bmatrix} 1 & 0 \\ -2/R_x & 1 \end{bmatrix} = \begin{bmatrix} 1 - \frac{2L}{R_x} & L \\ -\frac{2}{R_x} & 1 \end{bmatrix} \tag{3.2}$$

Except for the very first mask-interaction, where the field experiences only a clipping and no phase variation, these steps are repeated p times to acquire the radiation field at each reflection. Single-mode Gaussian beams were taken as initial fields. For clarity and unless otherwise stated, the reflectivity of the toroidal mirror was set to 100 %. Generally, we assumed the incoupling angle θ to be small such that 3$^{\mathrm{rd}}$ order astigmatism is negligible.

For the experimental assessment of this approach, we used a gold coated toroidal cell of horizontal radius $R_c = 72$ mm and vertical radius $R_y = 131.6$ mm. The incident angle θ was chosen to yield an optical path length of 9.9 m. The reflected light was clipped by a mask comprising 69 apertures of diameter $x_0 = 4$ mm. On this setup we also compared the calculated irradiance pattern with the experimental observation using a red trace laser ($\lambda = 660$ nm). Fig. 3.2 shows the excellent agreement between simulation and experiment after different numbers of reflections.

3.1.5 Results and Discussion

The successful verification allows to use this method for optimization calculations. Generally speaking, MPCs are designed to reach high transmission, long optical path

length, and a low fringe-noise level. For mobile and compact instrumentation, this should be achieved with minimal weight and within a small volume. Often, these requirements are inherently exclusive: For instance, the overall transmission becomes higher if the apertures are larger, but at the cost of fewer reflections within a cell of equal diameter. These conceptual trade-offs have to be considered within the given constraints of the specific application. Therefore, we firstly focus on optimizations for a fixed representative geometry by assessing the impact of the initial field. In

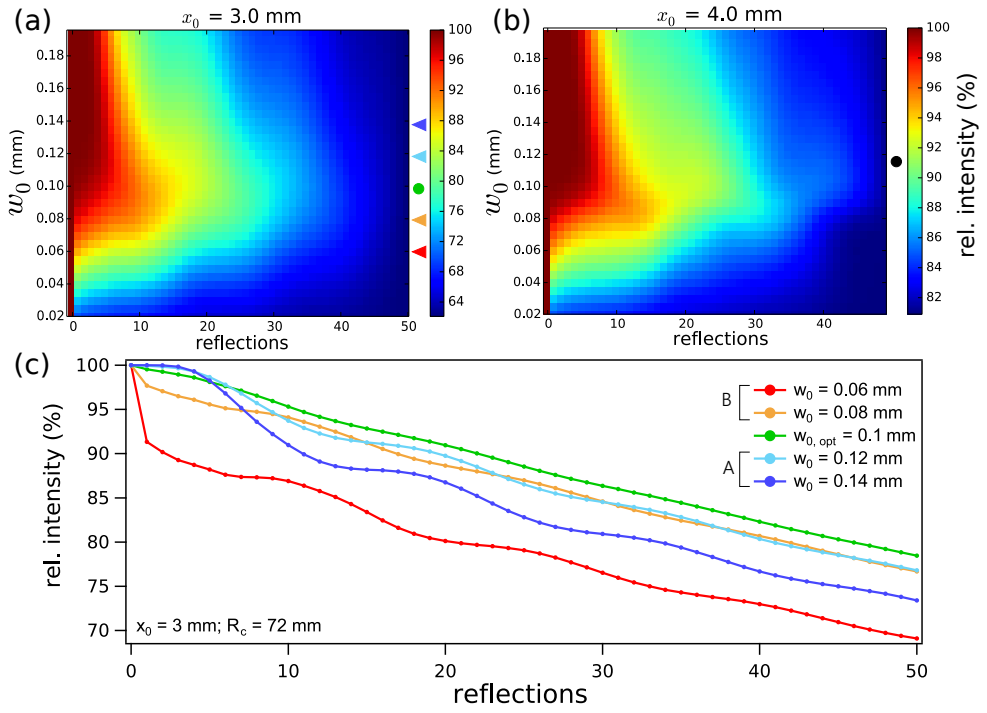

Figure 3.3: Evolution of the relative residual intensity for different initial Gaussian beams as the radiation is successively reflected and truncated within the MET-MPC. For this one dimensional calculation of the unstable horizontal plane we assumed a cell with 72 mm radius and an aperture size of (a) 3 mm and (b) 4 mm for 6 µm wavelength of the laser. The optimal initial field, i.e. the one which leads to lowest intensity loss, is indicated with a bullet. (c) Horizontal slices (indicated by a triangle) through the left colormap highlight the intensity evolution structure for the two non-optimal regimes A and B.

the stable vertical plane, the initial field can be chosen to match the eigenfunction of the corresponding geometry in order to minimize the clipped portion of the field. In contrast, finding optimal settings in the unstable horizontal plane is not trivial, since beam truncation cannot be avoided and the effect of any deviation from such an optimal case is non-intuitive. The intensity evolution is illustrated for two aperture sizes in Figs. 3.3(a) and (b) as a function of differently diverging Gaussian beams. Thereby, the initial field is fully defined by the laser wavelength and the beam-waist size, which is located at the center of the first pass. In order to highlight the influence of the unstable horizontal direction, the calculation was performed in one dimension,

comprising only the horizontal axis. As expected, the transmission is generally higher in Fig. 3.3(b) than in Fig. 3.3(a) due to the 1 mm larger aperture-diameter. In addition, the dependence of the intensity evolution on the chosen initial field changes remarkably. However, similar tendencies are observed: Generally, we can identify two regimes of distinct loss-structure within the set of differently diverging Gaussian beams $u(w_0, \lambda)$ characterized by

$$\text{A) } w_0 > w_{0,opt} \quad \text{and} \quad \text{B) } w_0 < w_{0,opt} \tag{3.3}$$

The specific Gaussian initial field $u(w_{0,opt}, \lambda)$ yields the highest relative intensity for large numbers of reflection and decreases almost linearly. Furthermore, we expect $u(w_{0,opt}, \lambda)$ to minimize the fringe-level, since the diffraction-caused field spillover onto neighboring apertures is reduced. Therefore, it is referred to as the optimal initial field. The corresponding intensity evolution is labeled with a bullet in Fig. 3.3(a) and (b), and it is clearly dependent on the aperture-size. It turns out that the irradiance field $|u(w_{0,opt}, \lambda)|^2$ at the first aperture is most similar to that of the eigenfunction of an equivalent resonator and converges to it within a few reflections. If the initial Gaussian field deviates into range A, where the beam diameter is smaller than the first aperture, the intensity-loss follows a damped oscillation as the field converges to the steady state solution. In range B, the stronger divergence leads to a significant intensity-loss already at the very first aperture. This initial clipping at the input aperture can lead to an accentuated widespread diffraction at the first pass. Overall, the results clearly suggest that the beam waist w_0 should be chosen as $w_{0,opt}$ for best performance of the MPC. However, $w_0 > w_{0,opt}$ may be acceptable since the intensity loss and thus the diffraction-caused spillover are only slightly larger in total. For arbitrary dimensions of a toroidal cell, the optimal initial field at the first aperture can be estimated as *the* Gaussian beam with the smallest w_0 that yields an irradiance field most similar to the steady state solution. This resonator eigenmode may be found e.g., by the herein used successive approximation method, or the method of kernel expansion (Li et al., 1966).

Another significant impact on the intensity evolution can be attributed to the beam waist position of the first pass. Classical geometrical considerations suggest the focus to be optimal if placed at the center between the entrance-aperture and the first reflection. The explicit simulation quantifies this dependence, and it furthermore reveals the self-similarity of the intensity evolution curves upon a waist displacement of $|z_{w_0}|$ (Fig. 3.4). If the waist is located *behind* the center (i.e. closer to the first reflection, $z_{w_0} = -5\,\text{mm}$) a few reflections are needed to widen up the beam until the aperture interaction becomes dominant. While this leads to significant differences in the field shape at early reflections (cf. irradiance fields of R7, Fig. 3.4 insets left), the fields become indistinguishable after many round-trips (R70, insets right). Thus, the transmission of MET-MPCs can be optimized by centering the focus position, thereby avoiding unnecessary intensity-losses at early reflections.
By applying the computationally deduced optimal Gaussian beam configuration in the experimental setup mentioned above, we were able to lower the fringe-noise level from 4 % (Mangold et al., 2016) to 0.14 %.

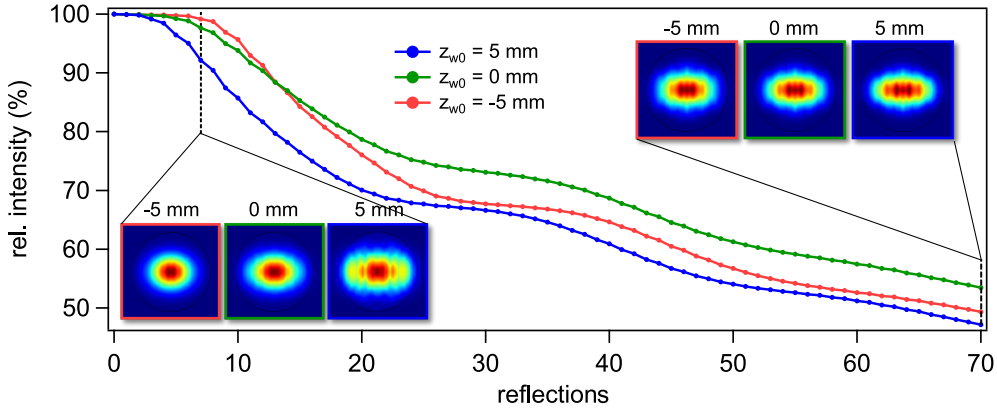

Figure 3.4: (a) Normalized intensity evolution from a two dimensional calculation with $\lambda = 4.3\,\mu\text{m}$, $R_c = 72\,\text{mm}$, and circular apertures with diameter $x_0 = 4\,\text{mm}$. The initial Gaussian field has a fixed waist size ($w_0 = 0.1\,\text{mm}$) but is placed at three different positions z_{w_0}. Additionally, the irradiance patterns are compared for reflections R7 and R70.

A complete geometrical optimization of MET-MPCs – including the optical path length as a variable – requires the quantification of the expected noise level and its dependence on the cell dimensions, particularly on the aperture-distance d. Multipass cells for absorption spectroscopy are often limited by optical fringes attributable to radiation falling onto the detector after having passed a different path length (McManus and Kebabian, 1990). Although fringes typically occur between parallel semi-transparent surfaces in the optical path (etaloning), diffracted radiation leaking onto neighboring apertures causes a comparable effect within MET-MPCs. To a certain extent, these spillovers exist at each reflection. However, an absolute treatment by tracing all leaking radiation is not feasible. Therefore, we estimated the expected fringe-induced noise level considering the interference on the outgoing radiation by the neighboring fields. This was done by simulating all complex fields explicitly and superposing the last field together with the radiation spilling over from its direct neighbors onto the terminating aperture. Fig. 3.5(a) shows the calculated last field as well as the ones to its right and left, i.e. reflection 28 and 41, for the experimental setup described above. In general, the intensity of two superposed fields is given at each point by

$$I(\mathbf{r}) = I_1(\mathbf{r}) + I_2(\mathbf{r}) + 2\sqrt{I_1(\mathbf{r})I_2(\mathbf{r})}\cos(\phi_2(\mathbf{r}) - \phi_1(\mathbf{r})) \tag{3.4}$$

and the total intensity is retrieved by integration over the entire aperture. As the wavelength is tuned, the local phase difference $\phi_2(\mathbf{r}) - \phi_1(\mathbf{r})$ changes, leading to an intensity modulation referred to as fringe-noise. Along these lines, we estimated the fringe level as the maximal intensity difference obtainable by an independent phase-variation of both interfering fields. This is plotted in Fig. 3.5(b) as function of the aperture distance d. Prior to this calculation, the relative intensity of the involved fields was scaled according to their reflection number, whereby a mirror reflectivity of

98 % was assumed. We observe the intensity variation to decrease quickly and level off as the aperture distance increases. This is not only due to low peripheral intensity, in addition, the high spatial frequency of the phase far from the center leaves the total intensity almost unchanged upon variation of the phasor. For the experimental aperture distance $d = 2.6\,\mathrm{mm}$ and diameter $x_0 = 4\,\mathrm{mm}$, this method predicts a fringe-induced relative variation of the integrated intensity of 0.7×10^{-4}, which cannot fully account for the measured optical noise level in the corresponding experiment (1.4×10^{-3}) as discussed above. This leads to the conclusion that the spillover at other apertures in the cell significantly contributes to the total observed fringe level. Nevertheless, the data suggest that for this particular setup and wavelength, a similar noise level can be expected for much smaller spacing of the apertures. Therefore, a corresponding adaption of the mask could increase the optical path length by more than a factor of two for the same cell size.

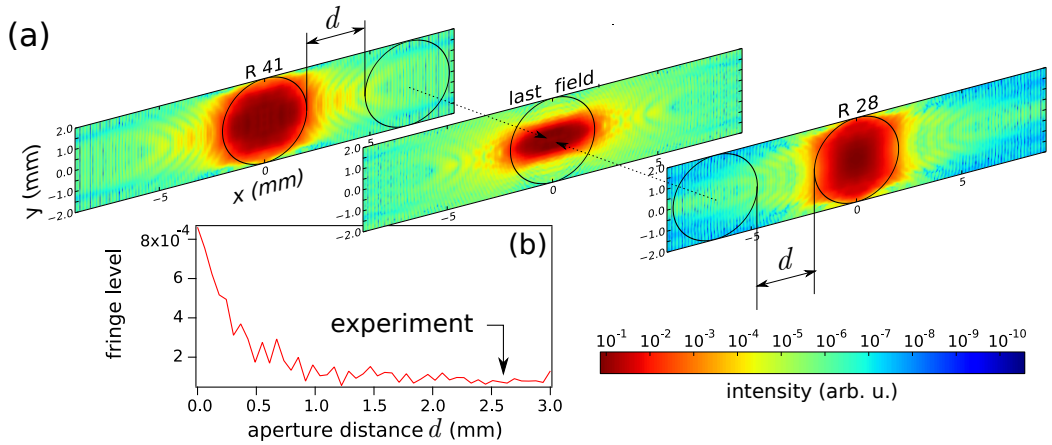

Figure 3.5: The last irradiance field (R69) and its neighbors (R41 and R28) in logarithmic scale. To estimate the interference induced by diffracted radiation from neighboring fields, the superposition of these three fields is calculated within the last aperture. An independent phase variation of both interfering fields allows to retrieve the maximal intensity modulation upon laser wavelength tuning and is therefore a proxy for the fringe-caused noise level. This maximal modulation, normalized by the average intensity, is shown in (b) for different aperture distances d.

In conclusion, we discussed the inherent optical instability and demonstrated a strategy to optimize the performance of mask-enhanced toroidal multipass cells (MET-MPC). By explicit simulation of the complex radiation fields after each reflection, we showed the pseudo stabilization of the laser beam as a result of the successive clipping at the aperture mask. The influence of this truncation on the transmitted energy is presented for exemplary cases, and the simulation is used to predict optimal initial field configurations. We finally assessed the mutual interference of diffracted radiation from neighboring apertures as an important source of optical fringes. Thereby, we revealed further optimization potential towards more compact constructions. This supports MET-MPCs as lightweight and efficient alternatives to established strategies of beam folding.

3.2 Segmented Circular Multipass Cell

Despite the thorough understanding of the toroidal mask-enhanced MPC concept and the ability to simulate the impact of specific dimensions, major drawbacks are persisting: The need for beam-shaping and the high sensitivity to misalignment are perhaps the most substantial disadvantages especially with regard to mobile applications. However, the idea of using the internal surface of a rotationally symmetric body that intrinsically contains the reflective surfaces, remained appealing.
Therefore, the aim was to structure the internal surface such that the shape of the laser beam is preserved even upon multiple reflection. As a result, the beam-clipping mask becomes obsolete and the transmission practically independent of beam-shaping and alignment. This comes at the cost of slightly more complicated manufacturing process due to the non-continuous rotational symmetry of the internal surface. This section describes the concept of the *segmented circular multipass cell* (SC-MPC) starting with the theoretical framework, the design of the first prototype, as well as initial validation experiments.

The content of this section is based on the manuscript published in the peer-reviewed journal *Optics Letters* (OSA), Graf et al. (2018).

3.2.1 Abstract

Compact and lightweight laser absorption spectrometers for accurate trace gas measurements are of great scientific and commercial importance. In these instruments, the multipass cell (MPC) represents a critical element in terms of achievable size and sensitivity. Herein, we introduce a versatile MPC-concept that unifies compactness, mechanical rigidity, and optical stability. Relying on fundamental cavity design principles and modern diamond turning techniques, we have developed a segmented circular MPC that allows efficient and interference-free beam folding. A prototype cell is presented featuring up to 10 m optical path length at a total mass of less than 200 g. Incorporated in a highly compact setup without additional beam pre-shaping optics, we demonstrate a normalized noise level of low 10^{-4} (2σ) at 1 Hz.

3.2.2 Introduction

Non-destructive and contact-free gas analysis by laser absorption spectroscopy is a powerful and widely applied measurement technique (Curl et al., 2010). Nowadays, we face an increasing demand for compact and lightweight spectrometers to be deployed e.g., aboard of cars, UAVs, and balloons, or as part of planetary exploration missions (Gurlit et al., 2005; Webster and Mahaffy, 2011; Richter et al., 2015; Villa et al., 2016). Such mobile settings are of growing importance in a multitude of disciplines as they offer enhanced spatial and temporal sampling flexibility. With the advent of quantum cascade lasers (QCL), interband cascade lasers (ICL), and thermoelectrically cooled MCT-detectors, compact and portable mid-infrared sensors became feasible. However, high-precision measurements of molecular compounds require the

extension of the optical path length (OPL) to improve the signal-to-noise ratio. In direct absorption spectroscopy, this is usually achieved by the incorporation of a multipass cell (MPC). Currently, this key element is the major limiting factor towards miniaturization, because the established designs do not satisfyingly combine both compactness *and* interference-free beam folding. To date, best documented precision and most efficient beam folding are reached in astigmatic Herriott cells (McManus et al., 1995) or variations thereof. However, these solutions are very sensitive to the relative positioning of the mirrors, so that a considerable mechanical effort is required to realize and maintain their alignment. Moreover, the beam waist size and location must be accurately adjusted by additional optical elements to ensure low-noise operation. As a result, corresponding optical setups are bulky and heavy, limiting their applicability on portable platforms. Therefore, the design of suitable MPCs for mobile instruments has to be fundamentally reconsidered.

Depending on the specific target gas and deployment conditions, the requirements on an MPC can be very diverse. Nevertheless, common criteria for mobile in-situ spectrometers can be summarized as follows: (*i*) For compactness, a long OPL is desired at low overall mass and size. As these properties are mutually exclusive, the volume-normalized optical path length $\delta = \mathrm{OPL}/V$ is an important figure of merit. (*ii*) Low effective volumes are advantageous for high temporal sampling resolution. (*iii*) Mobile systems require mechanically robust cells to preserve their functionality upon thermally or mechanically induced stress. This can be achieved by either enhanced rigidity or by tolerance against misalignment. (*iv*) In order to benefit from the larger absorption signal, interference related optical noise must be suppressed. Therefore, it is crucial that the laser beam remains well defined upon multiple reflections. (*v*) In case of reactive or adhesive molecules, the exposed cell surface area should be kept low in order to reduce chemical interaction and memory effects. (*vi*) Finally, parasitic biases due to ambient air absorption can be avoided by minimizing the OPL outside the sampling volume.
In this Letter, we introduce a novel MPC-concept that takes into account all of the above criteria. We describe its design principles and present benchmark experiments acquired with a first prototype cell.

3.2.3 Importance of Stable Beam Confinement

Recently, Tuzson et al. (2013) presented the toroidal MPC as a lightweight alternative to collinear, two-mirror based cells or circular arrangements of individual mirrors (Thoma et al., 1994). The emergence of an N-star polygram when coupling a laser beam under an oblique angle to the inner surface of a cylindrical or toroidal surface, was shown to be a versatile optical path extension concept. Indeed, the monolithic circular geometry results in a mechanically robust and lightweight optical element, having optimal properties for open-path measurements and high flow rate applications. However, according to basic resonator theory, the inherently concentric mirror configuration in the radial plane of any toroidal surface inevitably leads to a divergence of laser beams upon multiple reflections (Li et al., 1966). Hence, the outgoing radiation consists of a superposition of various beam components, causing strong op-

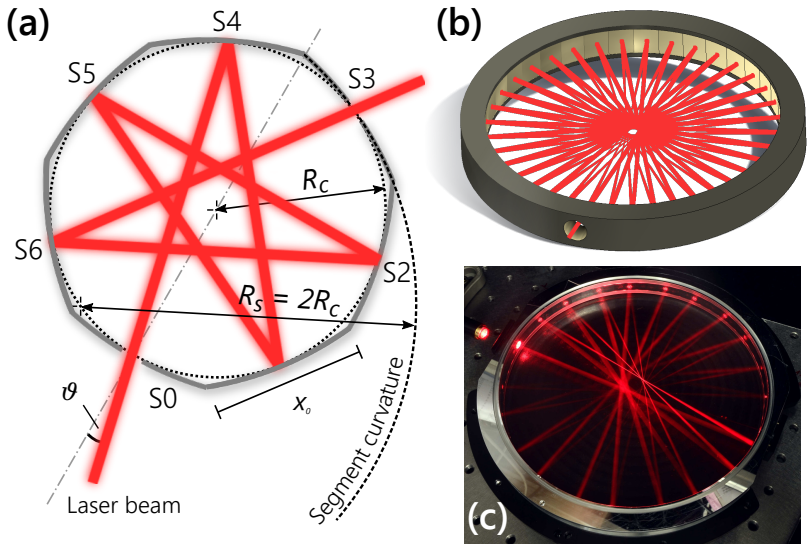

Figure 3.6: (a) Schematic drawing of the inner surface of an SC-MPC, here with $p = 7$ confocal segments. The coupling angle ϑ of the beam defines the reflection pattern by the rules of an N-star polygram. (b) Concept model and ray trace simulation. (c) Photograph of the cell prototype. The beam folding principle is visualized by a red trace laser and the alternating beam envelope can easily be observed. The angle ϑ was selected to realize 22 reflections, that is, a reduction of the maximally supported OPL to one third.

tical fringes in the signal. As a workaround, the integration of an aperture mask has been proposed that constrains the reflective inner surface and thereby truncates the divergent radiation at each reflection (Tuzson et al., 2013; Mangold et al., 2016). While this measure leads to a reduction of the optical fringes, the successive generation of diffraction patterns at each aperture yields a significant complication of the design, optimization, and alignment process (Graf et al., 2017). In the concept proposed here, we combine the mechanical advantages of the circular symmetry with inherent optical stability.

Within the framework of paraxial resonator theory, the criterion to confine light between equally curved concave mirrors in a *stable* manner can be derived as $R > L/2$, i.e. the radius of curvature R of the mirrors must be greater than half their separation distance L (Li et al., 1966). It is obvious that this criterion cannot be fulfilled by any object that obeys continuous rotational symmetry. Thus, the only possibility to incorporate the above requirement into a circular geometry is to renounce the central axis of rotation and thereby breaking the continuous symmetry. This leads to a segmentation of the reflective inner surface (see Fig. 3.6(a)), where each segment is allowed to have a larger radius than the cell itself. As shown in Figs. 3.6(b, c), the emerging segmented circular multipass cell (SC-MPC) successfully prevents beam-divergence. The beam spot radius w_i on each mirror segment i can be calculated for given R and L (Siegman, 1986). To avoid spillover and beam-branching, the size of the mirror segments has to be dimensioned according to the largest occurring

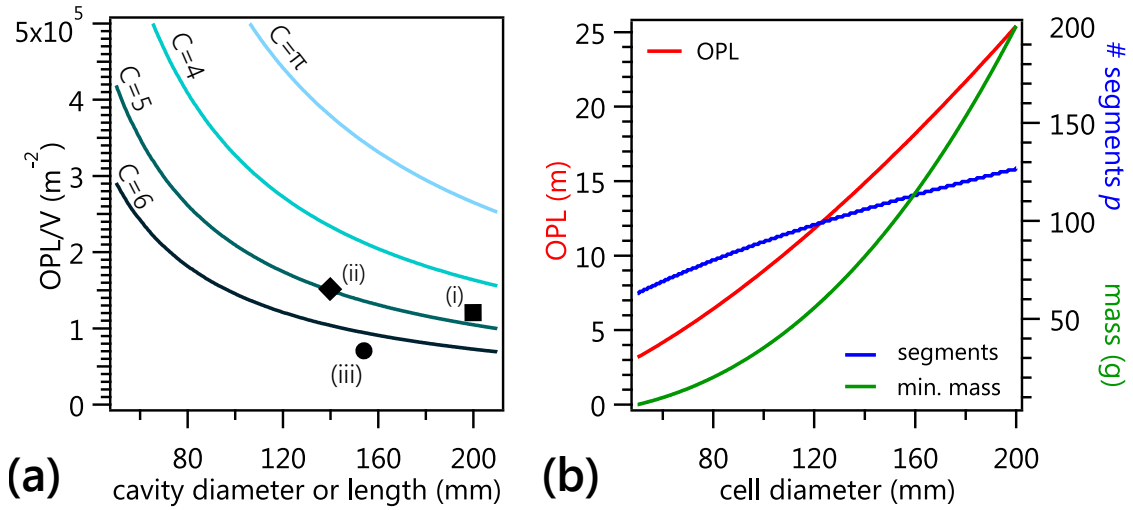

Figure 3.7: (a) Calculated beam folding efficiency as function of the cell diameter for different segment scaling factors. Literature values from existing solutions are added as reference: *(i)* astigmatic Herriott (McManus et al., 1995), *(ii)* mask-enhanced toroidal (Mangold et al., 2016), *(iii)* herein presented prototype. (b) The maximal OPL (left scale), the minimal mass and the number of reflections (both right scale) are shown as a function of the cell diameter for $C = 4$ and $\lambda = 6\,\mu\text{m}$. The mass calculation assumes quadratic segments and a full aluminum body with wall strength-to-radius ratio of 1:9.

beam spot. Thus, we may define the full side length of the quadratic segments as $x_0 = 2C\max(w_i)$, while the scaling factor C should be chosen grater than π to prevent leakage. Among all mirror arrangements fulfilling the stability criterion, the *confocal* arrangement ($R = L$) is especially suitable for this application, since it supports the smallest beam spots ($w^2_{i,conf} = L\lambda/\pi$). Therefore, provided that the beam is pre-shaped to match the lowest-order Gaussian eigenmode, the cell reaches maximal compactness. For this case, we can derive the theoretical dependence of the cell diameter d to its supported OPL. Under the assumption of small incoupling angles ϑ (i.e. dense patterns), which legitimates the approximation $d \simeq L = d\cos\vartheta$, the OPL is given by

$$\text{OPL} = p \cdot d = \frac{(d\pi)^{3/2}}{2C\sqrt{\lambda}} \tag{3.5}$$

with λ being the wavelength of the laser and p denoting the number of segments. According to this equation, the maximal OPL, minimal mass, and the corresponding number of segments are shown in Fig. 3.7(b) as a function of the cell diameter for a range of realistic examples. Figure 3.7(a) highlights the outstanding potential of the SC-MPC towards miniaturization. For small cell diameters, the beam folding efficiency is enhanced due to the small beam spot radii in such cavities. The comparison

shows that the compactness of our current prototype (see below) is already close to state-of-the-art MPCs, even though the segment size was designed very conservatively.

A larger segments size, i.e. selection of a higher C-factor, yields increased tolerance against misaligned, imperfect or misshaped beams – at the expense of a somewhat larger cell diameter. Especially when coupling arbitrarily focused beams, the segment dimensions must account for larger and variable beam spot sizes. In a perfectly confocal arrangement, however, only two alternating beam shapes occur, which remain constant for any number of reflections (cf. Fig. 3.6(c)). Therefore, a *confocal* SC-MPC accepts any beam, whose spots completely fit onto two consecutive segments – regardless of the exact waist size and position. This is a key advantage because tedious pre-cell beam shaping becomes obsolete. In essence, collimated laser sources, as commercially available, can be directly attached to the cell. This possibility not only enables highly compact setups, but also increases the stability and avoids an optical path outside the sampling volume.

3.2.4 Prototype Design

We designed and developed a prototype cell in order to validate the performance of the proposed concept in a spectroscopic application. The SC-MPC consists of a monolithic aluminum-ring with inner radius $R_c = 77.25\,\mathrm{mm}$. The segmented inner surface has been realized by single-point diamond turning (LT Ultra-Precision Technology GmbH, Germany). Thereby, the servo-controlled lathe tool is periodically modulated in coordination with the cell revolving around its main axis. Such machining requires two-axis flexibility (axial and radial), potentially resulting in increased surface roughness compared to simpler geometries. The corresponding effects are discussed in more detail below. Sixty-five quadratic, spherically curved segments were shaped into the ring, each with a 7.47 mm side length and a radius of curvature $R_s = 2R_c = 154.5\,\mathrm{mm}$. The width and height of the segments is chosen to offer appropriate alignment tolerance ($C = 6.9$). To enhance the surface quality, the segments are machined into a 0.2 mm thick chemically deposited nickel-phosphor layer. A galvanic gold plating (Epner Technology, U.S.) provides high mid-infrared reflectivity.

The in- and output apertures are placed at opposite sides (segments 0 and 33), providing a maximum of 64 passes. This configuration has been selected to ensure enough space for optical components to be placed directly at the cell. The laser beam enters under an angle $\vartheta = \frac{\pi}{2}(1 - 2q/p)$, with q denoting the pattern-density. By selecting q close to $p/2$, we minimize the creation of an astigmatic beam upon reflection and ensure a high-density pattern. Thus, a maximal OPL of 9.89 m is reached for $q = \lfloor p/2 \rfloor = 32$ resulting in $\vartheta = 1.38°$. By variation of ϑ, a different first segment can be selected, leading to a reduction of the OPL, e.g., by a factor 1/3, as shown in Fig. 3.6(c). For low-pressure measurements, the cell can be closed with two anodized aluminum lids and tilted CaF_2-windows at the apertures. Thereby, the effective sampling volume becomes 140 ml, implying a beam folding efficiency of $\delta = 0.7 \times 10^5\,\mathrm{m^{-2}}$. The mass of the cell itself amounts to 198 g.

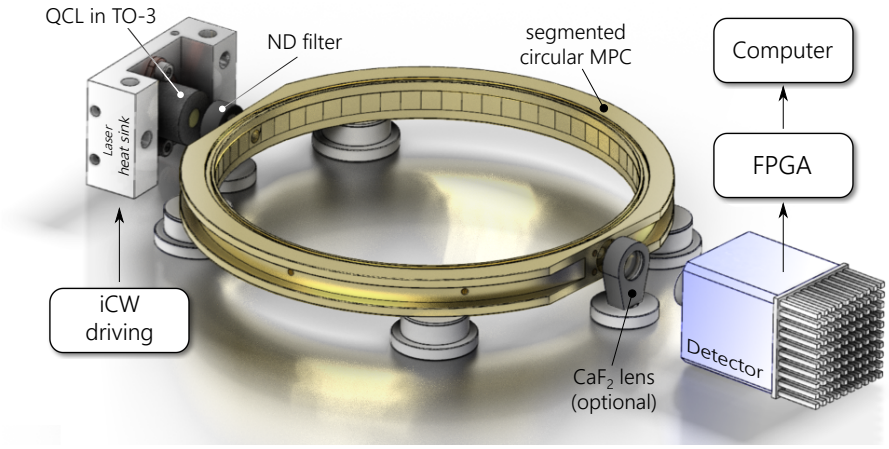

Figure 3.8: Highly compact setup for spectroscopic benchmark experiments and noise characterization. Besides laser, SC-MPC, and detector, the setup features only two additional optical elements: a focusing lens and an ND filter. Alternatively, an individually curved last segment allows direct focusing onto the detector to gain further compactness of the system.

3.2.5 Validation Experiments

Benchmark experiments were performed by direct laser absorption spectroscopy using a cw-DFB-QCL (Alpes Lasers, Switzerland) emitting at 7.83 µm. The laser is packaged in a TO3-housing with built-in collimation-lens. By placing the laser directly at the input aperture of the cell, the OPL outside the sampling volume is drastically reduced. Due to the high optical power up to 30 mW, a neutral density filter (ND, OD = 1.0) was inserted between the laser and cell to prevent detector saturation. The special curvature of the last segment ($R_{S64} = 320\,\text{mm}$) enables in-cell beam focusing onto a directly attached detector. However, best noise levels were obtained by adding a CaF_2 lens ($f = 20\,\text{mm}$) in front of the MCT-detector (Vigo Systems, Poland), as depicted in Fig. 3.8. Intermittent continuous-wave (iCW) laser driving (Fischer et al., 2014) and data acquisition was realized by in-house developed FPGA-based hardware (Liu et al., 2018). Spectra were recorded at 1 kHz and averaged to a 1 Hz data stream.

For spectroscopic characterization, we selected a strong and isolated rovibrational transition of methane (CH_4) at $1275.04\,\text{cm}^{-1}$. Fig. 3.9(a) shows the recorded low pressure ($p = 280\,\text{hPa}$) transmission spectrum of dry atmospheric air, containing 1.92 ppmv CH_4. The absorption lines are fitted by a Voigt profile considering the parameters from the molecular database (Rothman et al., 2013). The very low normalized noise level of $2\sigma = 2.64 \times 10^{-4}$ at an averaging time of 1 s even makes the N_2O-transitions at $1274.99\,\text{cm}^{-1}$ clearly observable. Measuring CH_4 at ambient pressure, we achieved sub-ppb precision after 1 s, corresponding to an absorption-noise of 2×10^{-6}. This noise level is similar to state-of-the-art values reported for Herriott-type systems (McManus, 2010). It should be noted that we obtained these results without applying fringe-suppression measures such as piezo-modulation of optical components.

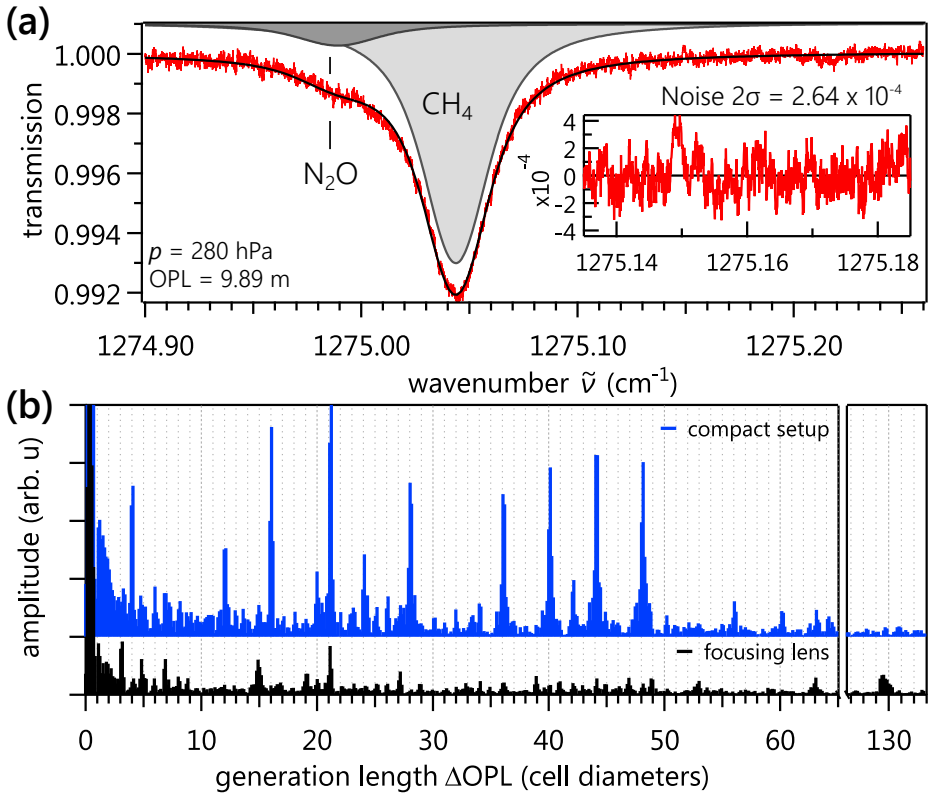

Figure 3.9: Measured transmission spectrum of CH_4 (1.92 ppmv) and N_2O (323 ppbv) in dry atmospheric air at 280 hPa. The inset shows the local noise on the baseline. The optical path length of 9.89 m is achieved by 64 passes through the SC-MPC prototype. (b) A Fourier transform of the spectral noise signal displays the occurring fringe frequencies as a function of their generation length. While the bottom trace is calculated from the data set in (a), the top trace is obtained from a spectrum acquired without the use of an additional focusing element after the cell.

Whilst an excellent noise performance is achieved, further insight about the optical behavior of the SC-MPC design is gained by the detailed investigation of the residual noise level. Besides a dark noise contribution of $2\sigma_{\mathrm{dark}} = 1.66 \times 10^{-4}$ at 1 Hz, the existence of optical interference fringes is revealed. These fringes are caused by beam fractions that travel different distances with respect to the main beam. In air, the fringe generating length, i.e. the path length difference ΔOPL between two interfering beam fractions, is related to the spectral fringe period by $\Delta\tilde{\nu} = \frac{1}{\Delta\mathrm{OPL}}$, in cm^{-1}. Therefore, as shown in Fig. 3.9(b), the individual fringe frequencies found by Fourier transforming the spectral noise signal can be displayed as a function of ΔOPL (McManus et al., 2011). Along these lines, the peak located somewhat above 2×OPL (at 130 passes) denotes classical Fabry-Pérot-etaloning between the laser and detector. In contrast, noise frequency components generated at distances shorter than $(p-2)$ passes can only originate from interference by stray or scattered light. Diffraction

measurements on the diamond-turned surface indicate minor surface structures of 7.9 µm periodicity in axial direction. This surface imperfection is a possible source of stray light within the cell. However, improper alignment or strong deviations from Gaussian beam shapes can also lead to undesired beam-branching. For instance, by deflection at the input aperture, some radiation can reach the detector already after one pass. The interference of such a beam-portion with the main beam after a full round-trip gives rise to a peak at 63 passes (see Fig. 3.9(b), bottom trace). The fringe frequency spectrum is sensitively dependent on alignment changes, suggesting that the stray light generally follows much more complex traces within the cell. Additional information about the origin of stray light is obtained by using the SC-MPC without a focusing lens. The approximately four times higher normalized noise level contains dominant frequencies at integer multiples of the cell diameter, as shown in the top curve of Fig. 3.9(b). The increased noise level can be explained by the focusing lens that spatially separates different directional components at its focal plane, thereby acting as a filter for undesired alternative passes. Additionally, interference-noise is induced by reflections at optical components situated after the cell that fall back into the MPC (e.g., from detector chip or window). A focusing element projects such reflections back onto the last segment, proceeding backwards and eventually creating classical etaloning. Indeed, the absence of a lens leads to a clear attenuation of the 2×OPL-frequency while the now undirected back-reflections generate numerous alternative passes. Therefore, the appropriate positioning of post-cell optical components is important – anti-reflection coatings, which were not used in our setup, are expected to further improve the noise performance. Hence, especially if back-reflections are rigorously suppressed, the incorporation of even more segments should be possible. This might be realized in a variety of creative progressions beyond the herein proposed configuration. Most relevantly, by specific tilting of particular segments, multiple round-trip patterns can be combined within the same cell. Further options are the stacking of multiple SC-MPCs or the off-plane beam coupling to create two layers of axially offset reflections, which allows a denser arrangement of segments. Consequently, SC-MPCs can successfully compete with established solutions, also with respect to the maximal OPL.

In summary, we have presented a novel type of multipass cell that combines crucial requirements for mobile and mass-critical spectrometers. The monolithic circular arrangement of concave mirror segments ensures optically and mechanically stable beam folding, significantly improving the interference noise performance. This design renders pre-cell beam shaping obsolete, giving rise to very compact setups and minimal optical path length outside the sampling volume. High versatility is provided by the freedom to adjust the optical path length and the cell diameter according to individual constraints, while the dimensioning follows simple mathematical relations. We have demonstrated very low noise levels in a direct absorption spectroscopic setup and the possibility of high precision methane-measurements at ambient conditions. The segmented circular multipass cell (SC-MPC) is thereby confirmed as a suitable tool for a variety of future applications in compact and lightweight absorption spectroscopy.

Chapter 4

Instrumentation

Building a high-precision quantum cascade laser absorption spectrometer (QCLAS), which is lightweight *and* suitable for harsh environmental conditions, is a highly demanding task. This chapter focuses on the constructional details of the instrument and describes the integration of the aforementioned ideas and concepts into a field-deployable system. Starting with spectroscopy-related considerations, which define important aspects and dimensions of the instrument, the details of mechanical design and construction are discussed. Subsequently, the data acquisition, laser driving strategy, the electronics, and the involved software are presented.

Individual sections of this chapter are published in the peer-reviewed journal *Atmospheric Measurement Techniques* (EGU, Copernicus), Graf et al. (2020).

4.1 Targets and Conditions

Various decisions are directly influenced by the environmental conditions under which the instrument is supposed to work in. For design and simulation purposes, an atmospheric model is considered, comprising the altitude-dependence of the relevant values, i.e., pressure p, temperature T, and the amount fraction of water vapor χ. The definitions are guided by the international standard atmosphere (ISA) as summarized in Fig. 4.1(a). With an assumed ascent rate of $5\,\mathrm{m\,s^{-1}}$, the instrument should be designed for at least 5000 s of autonomous operation to fully cover the target region at least during ascent. Longer operation time also enables the measurement during descent. Despite the definition of a target region, the burst altitude of a meteorological balloon is difficult to foresee and may be at altitudes up to 32 km. Hence, in contrast to the *spectroscopic* target region, the *mechanical* range of requirements is broader (e.g. $p < 10\,\mathrm{hPa}$) and includes high peak accelerations at landing.

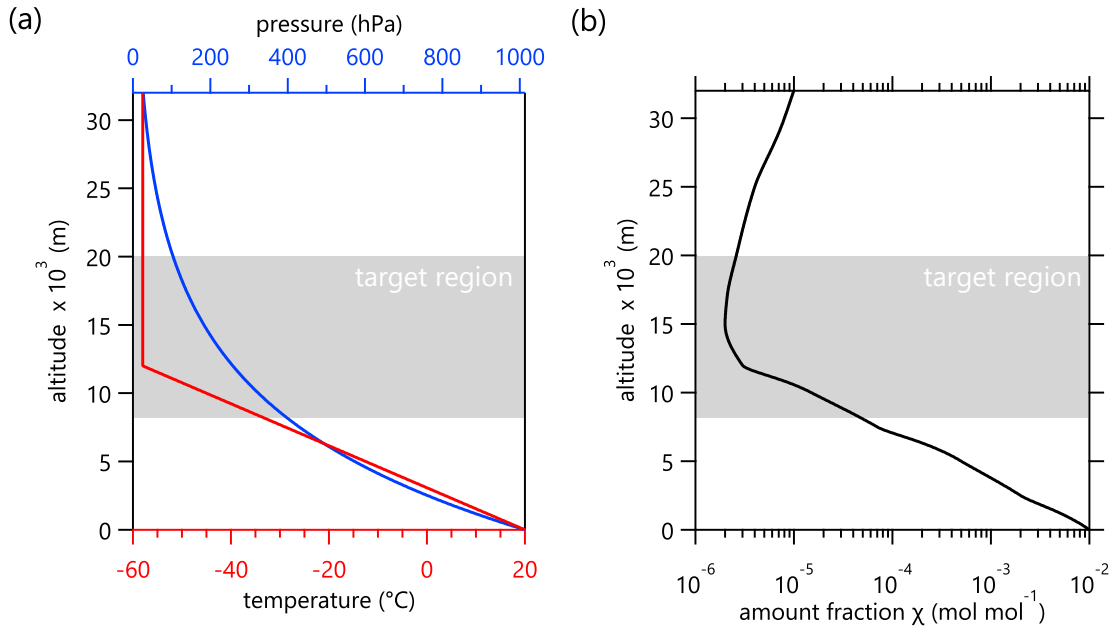

Figure 4.1: (a) Temperature and pressure curves as function of the altitude. The pressure follows an exponential decay whereas the temperature curve is dominated by the lapse rate of $-6.5\,\mathrm{K\,km^{-1}}$ below the tropopause. (b) Typical water vapor amount fractions throughout the troposphere and the lower stratosphere.

4.2 Quantum Cascade Lasers

The measurement of entire absorption spectra requires the temporal or spatial separation of radiation depending on the wavelength. Spatial separation is usually applied for broadband light sources using dispersive optical elements or gratings. In tunable

laser spectroscopy, the separation happens temporally, by sweeping the narrowband emission wavelength of the laser source. As a consequence, its detection is only required at one single spot.

Quantum cascade lasers are operating in the mid-IR spectral region (Faist, 2012), where many small molecules show strong fundamental transition. Distributed feedback (DFB) QCLs deliver continuous wave (CW) output power in the order of many tens of mW at an electrical power consumption of a few W, and can be encapsulated in matchbox-sized housings that include both a collimating lens and a TEC. A QCL device consists of a vertical stack of materials with alternating dielectric constant ϵ. This periodic structure gives rise to subbands in the electronic band-structure. An applied DC voltage forces electrons to cascade down these subbands under the emission of coherent radiation. A periodic Bragg grating on top of the active region is responsible for the mode selection and assures single-mode output. Any change of temperature leads to a variation of ϵ and thus the refractive index, leading to the emission of higher-energy photons at lower temperatures (about $-0.1\,\mathrm{cm^{-1}\,K^{-1}}$). Applying a current to the laser inherently leads to resistive heating of the active region and thus to a change of the emitted wavelength. Periodic current ramps can therefore be used to generate wavelength sweeps over $1-2\,\mathrm{cm^{-1}}$ with repetition rates up to 10 kHz. These fast scanning rates suppress the electronics-related $1/f$-noise to a level below the optics-induced noise. This scanning approach yields similar noise suppression as the often applied wavelength modulation technique (e.g., Silver and Hovde (1994); Paige (2005)).

The starting wavelength of the tuning process is selected by the laser's base temperature. A given QCL device usually covers a range of about $20\,\mathrm{cm^{-1}}$, which is configurable by changing its base temperature from -30 to 40 °C. The base temperature is maintained by a PID-controlled TEC in contact with the laser device.

4.3 Spectroscopic Considerations

The selection of the measured water transition is of highest relevance, since its choice directly influences many other decisions, such as the laser source, the optical path length and the surface material of the multipass cell (MPC), or the characteristics of the detector.

Due to the intense fundamental transitions of the H_2O molecule found in the mid-IR spectral region, this is an ideal range to probe low concentrations without the need of extreme enhancements of the optical absorption path length (OPL). The strong absorption band around $1600\,\mathrm{cm^{-1}}$, shown in Fig. 4.2, is due to the excitation of fundamental bending vibrations. In addition, none of the other abundant and absorbing atmospheric constituents exhibit relevant transitions between 1300 and $2000\,\mathrm{cm^{-1}}$ (7.7-5 µm) that could cause interference.

The selection of the specific absorption line within this range is further constrained by the following considerations: At extreme conditions for UTLS measurements ($p = 60$ hPa, i.e., 20 km altitude; $T = 220$ K, $\chi = 1$ ppmv), the absorption strength of the chosen transition should still result in a sufficient signal-to-noise ratio (SNR)

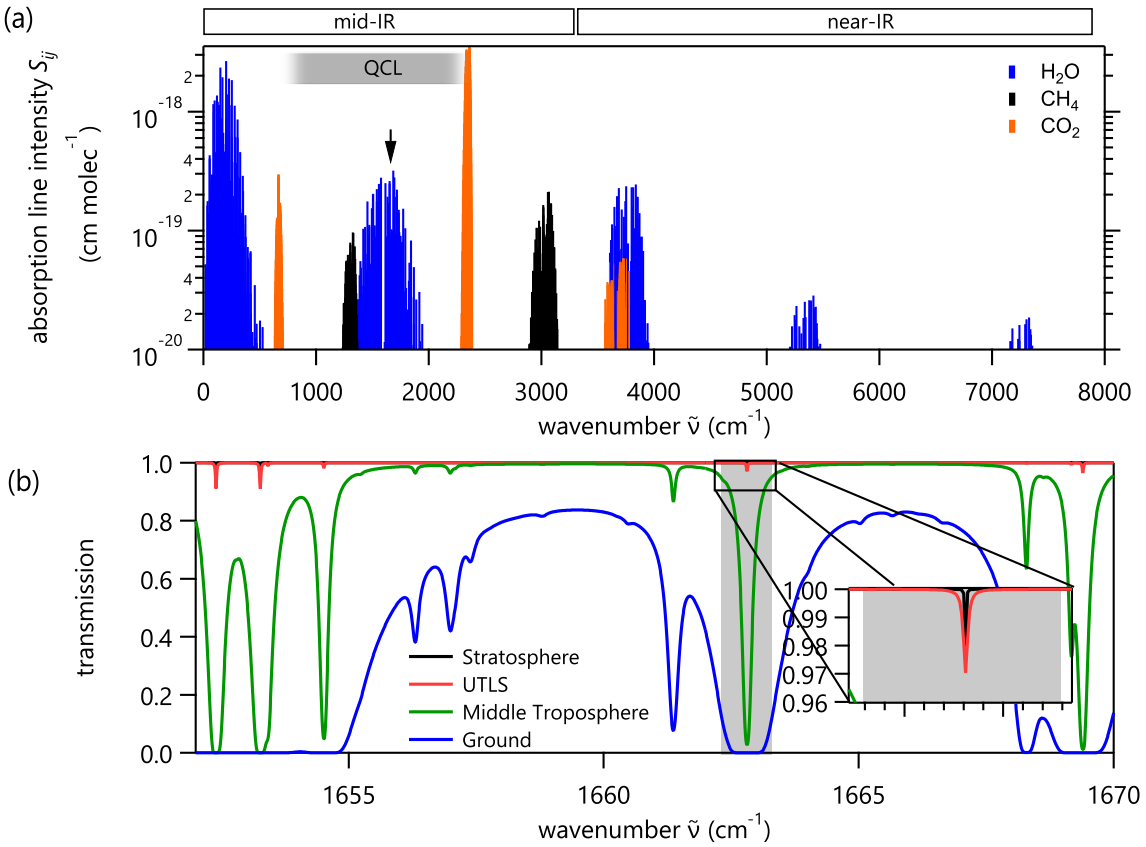

Figure 4.2: (a) Absorption line intensities for H_2O and potentially interfering atmospheric species. The arrow indicates the selected wavelength for the spectrometer. (b) Calculated spectra of the selected transition for different altitudes. The shaded area denotes the tuning range of the laser.

at the presumed sampling rate of 1 Hz. In contrast, at the low-altitude limit of the spectroscopic target region, the transition should still be unsaturated. This condition makes the selection more subtle, as it constrains the line intensity from above. In addition, the candidates should be isolated transitions with neighboring lines relatively far apart, such that the zero-absorption baseline is accessible in the vicinity.

In principle, the dimensions of the MPC, and thus the OPL can be used to adjust the measured absorbance. However, it is intuitive that a smaller MPC has many advantages: It is more rigid and stiff, more compact, and has a lower mass. Following the dimensioning guidelines for SC-MPCs as described in Ch. 3.2, a cell of 6 m OPL has an inner diameter of 10 cm, while each cm added to (subtracted from) the diameter increases (reduces) the OPL by approximately 1 m.

Finally, a suitable laser device must be available for the selected spectral region. In this context, *suitable* refers to: (*i*) Operation temperature between 5 °C and 30 °C. (*ii*) Sufficient spectral tunability $\Delta\tilde{\nu} > 1\,\mathrm{cm}^{-1}$. (*iii*) Sufficient radiant power (10-40 mW). (*iv*) Clean, Gaussian emission beam profile. (*v*) Free of internal reflections that cause interference.

The selection of the appropriate laser device and the scanned absorption lines was assisted by a simulation study: Artificially generated spectra at different wavelengths were evaluated under the expected conditions. This explicit simulation helped to elucidate the influence of neighboring lines and the SNR on the precision and fitting stability. In addition, the requirements in accuracy for the pressure and temperature measurement could be explored. Based on these findings, the basic parameters of the spectrometer were selected, as summarized in Tbl. 4.1.

Property	Details
Laser	DFB-QCL in HHL housing
Tuning range	$1.1\,\mathrm{cm^{-1}}$
Scanned transition	$1662.809\,\mathrm{cm^{-1}}$ (6 µm); H_2O: 221 ← 212 (J, K_a, K_c)
Average T_{Laser}	24 °C
Output Power P_{out}	20 mW
MPC	SC-MPC according to Graf et al. (2018)
OPL	609.4 cm
Segments	57 ($6 \times 6\,\mathrm{mm^2}$); spherical, $R_{\mathrm{curv}} = 108.820\,\mathrm{mm}$
Dimensions	$d_i = 108.862\,\mathrm{mm}$, $h = 15\,\mathrm{mm}$
Material	Rapidly solidified Al 6061 (uncoated)
Production	fast tool diamond turning
Weight	160 g

Table 4.1: Selected properties concerning the optical setup.

4.4 Hardware and Construction

4.4.1 Optical Setup

Given the harsh conditions the instrument will be exposed to, the optical setup is optimized for simplicity and robustness. Its basic concept underlying the optical setup, as discussed in Ch. 3.2, essentially consists of only the laser, the SC-MPC, and the detector. Fig. 4.3 shows this concept integrated as an autonomous instrument.

The optical setup is attached to a **carrier board** of a 4 mm thick carbon fiber/aramid honeycomb composite structure with very high stiffness at low mass (ca. $550\,\mathrm{g\,m^{-2}}$). The attachment of the individual components is realized by custom-positioned thread-inserts glued with epoxy resin. The spectrometer is built around its optical setup: The **MPC** with its open sampling volume is located in the center. On either side of the MPC, the laser and the detector are mounted with a few millimeters distance between them. Even though it would be desirable that the optoelectronic components are directly attached to the cell, a little gap is required to thermally decouple these sensitive devices from the MPC, which is directly exposed to the outside temperature changes. The **laser device**, packaged in a standard HHL housing (Alpes Lasers SA, Switzerland), is enclosed upside down in a 3D printed enclosure for easy mounting, insulation, and cooling. In a joint effort with the laser manufacturer, the

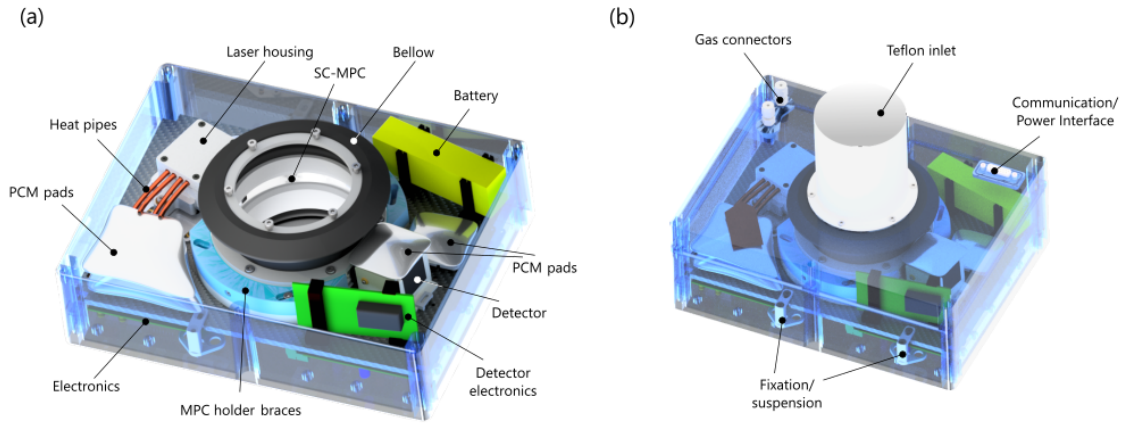

Figure 4.3: CAD renderings of the instrument (a) without lid and (b) in final configuration.

internal collimation lens (6-8 µm custom AR-coated $Ge_{28}Sb_{12}Se_{60}$-lens, $f = 1.8$ mm) was positioned to provide optimal beam shaping. This includes lateral positioning of the lens to ensure a clean Gaussian intensity distribution. The longitudinal shaping is rather insensitive: The beam waist should be located at a distance much greater than the cell diameter (quasi-collimated beam). This ensures the laser beam is finally focused onto the detector by a specially shaped last segment of the SC-MPC. As a result, additional optical beam-shaping components can be omitted. A custom-fabricated aluminum **laser alignment stage** allows high-precision positioning of the laser in five axes – only the translation along the beam axis is not supported. The vertical axis of rotation is designed to intersect the aperture of the cell, which simplifies the alignment. Having all necessary degrees of freedom covered at the laser side, the mounting of the detector can be kept simple, since the alignment can be accomplished by adjusting the laser. Thus, the **detector** is enclosed by a 3D printed holder which is directly clamped onto the board. The detector holder, which further acts as insulation, is covered by an aluminum plate in direct contact with the detector below. This plate is equipped with heat pipes and serves as a heat exchanger, as it is in contact with pads filled with phase-change material (PCM).

The efficient and compact construction permits the optical plane to be located only 1.75 cm above the board surface. The MPC is held in position by 3D printed **braces**. At the interface of the braces and the cell, a heating wire is integrated, which allows temperature-control of the cell to prevent icing or condensation.

4.4.2 Internal Optical Path

As the balloon-borne instrument ascends, it passes air masses with increasingly less moisture. In the UTLS, the amount fraction of H_2O is four orders of magnitude lower than on the ground. The extreme stickiness of H_2O leads to a continuous outgassing of water from surfaces and porous materials as the pressure decreases. This impor-

tant source of contamination in UTLS water vapor measurements is minimized by the open-path configuration of the instrument as the correspondingly high flow of air through the sampling channel effectively dilutes possible contamination. However, the air inside the instrument, which is isolated from the outside for thermal reasons, accumulates humidity. This eventually results in significantly higher H_2O concentrations inside the instrument than outside. The laser beam passes through this water vapor within the gap between the cell and the laser/detector. Although this internal path length is very short, the internal humidity content can still generate a considerable contribution to the total absorption signal, especially under stratospheric conditions. The initially chosen strategy to amend this problem was to maintain a pressure difference between the instrument box and the outside atmosphere by suppressing equilibration. This leads to unequal pressure broadening from the absorption contributions inside and outside the cell, respectively. Simulations have shown that, in order to disentangle these lines with a precision of $< 5\,\%$ under tropopause conditions, a $\Delta p > 200\,\mathrm{hPa}$ is required. This has various implications: Firstly, the enclosure of the instrument must mechanically resist this overpressure. Secondly, its leakage rate must be lower than the pressure difference due to the ascent i.e. $\frac{\mathrm{d}p}{\mathrm{d}h}\frac{\mathrm{d}h}{\mathrm{d}t} = 0.186\,\mathrm{hPa\,s^{-1}}$ at 10 km altitude. Unfortunately, using the actual enclosure, the required tightness cannot be achieved. As an alternative approach the internal path length is minimized: Specifically designed window holders, shown as inset in Fig. 4.4, shift the windows closer to the laser/detector, thereby reducing the internal OPL to 9 mm (0.14 % of the total OPL) and slightly extending the external, open-path length. Clearly, this measure only *reduces* the problem without providing a fundamental solution. To correct for the residual wet bias on the retrieved data, the internal humidity is measured by a capacitive sensor (TE, MS8607-02BA01), which is specified with an uncertainty of $\pm 3\,\%$ down to 300 hPa. Beyond this pressure, no information about the performance exists for this particular device. An extrapolation of the specifications yields an uncertainty up to 20 % as a conservative estimate. Low temperature is a more critical source of error for capacitive sensors (Lorek, 2014). However, given the stabilized temperature inside the instrument, this is of minor concern.

4.4.3 Mechanical Design

The key challenge of the mechanical design lies in the dilemma of *robustness* and *rigidity* vs. *low weight*. In a mobile and portable system, this is even more critical, since increased external stress and strain must be expected, which can influence the optical system. For example, displacements of optical components may induce intensity variations as well as changes in the laser baseline structure due to low frequency etalon fringes originating from transparent optics such as windows. These variations can potentially influence the retrieved amount fraction. Therefore, it is mandatory that external stress is decoupled from the optics. Fig. 4.3(b) shows further details of the mechanical construction: Four aluminum profiles are holding the carbon composite base plate – each being mounted excentrically on rubber suspensions. For the reason of thermal stabilization, the instrument is fully enclosed to prevent cold air from the outside entering the system during ascent. In principle, the bare spectrometer is sim-

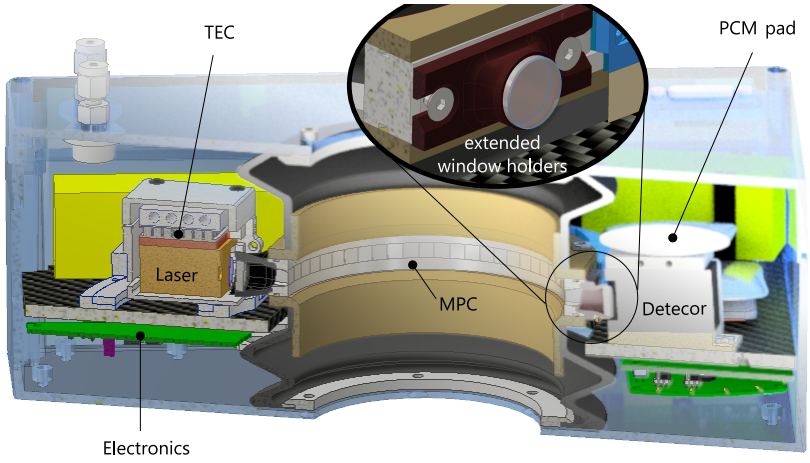

Figure 4.4: Schematic vertical cut through the instrument.

ply enclosed in a box, however, the realization of the open-path measurement funnel renders it more complex: The inner surface of the MPC must be exposed to ambient air, involving a direct connection between the enclosing box and the MPC. This is depicted in the vertical cut through the instrument in Fig. 4.4. In order to decouple the optical setup from the stress exerted on the enclosure, the connection is realized by a pair of flexible nitrile bellows. Connecting adapters are implemented with PEEK, a lightweight polymer with low porosity and rigidity properties similar to aluminum. This way, the air inside the instrument is isolated from the outside atmosphere. The enclosing box is a modified off-the-shelf polycarbonate box (Fibox, Switzerland); for diagnostic purposes with a transparent lid. The lid contains a 15-pin D-Sub connector as data (TCP/IP) and power interface (18 V DC). Additionally, the lid features two $^1/_4$-inch tube connectors, which are used to purge the instrument with dry air or N_2 prior to liftoff. Concentric to the MPC, a 100 mm long Teflon (PTFE) cylinder prevents air, contaminated by the instrument's surface, from streaming through the measurement zone. In the final assembly, the duct sticks out by 60 mm over the insulation, which is, with regard to the geometric and diffusive properties, considered sufficient to exclude self-contamination. The duct has a diameter of 86 mm, – slightly less than the SC-MPC itself (d = 108.9 mm). Teflon is chosen because of its low porosity and its low outgassing rate under reduced pressure (Weissler and Carlson, 1980). In addition, it is hydrophobic and generally non-adhesive, thus preventing the deposition of hydrometeors or condensate at the inlet. For balloon-borne deployment, the instrument is enclosed in 40 mm expanded polystyrol (XPS) as shown in Fig. 4.5(b) and has a total weight of 3.9 kg.

4.4.3.1 Modes of Operation

While this chapter mainly describes the instrument in its airborne configuration, the device is conceived for different operation modes (Tbl. 4.2). Given the difficulties to simulate stratospheric conditions in the laboratory, adaptations on the

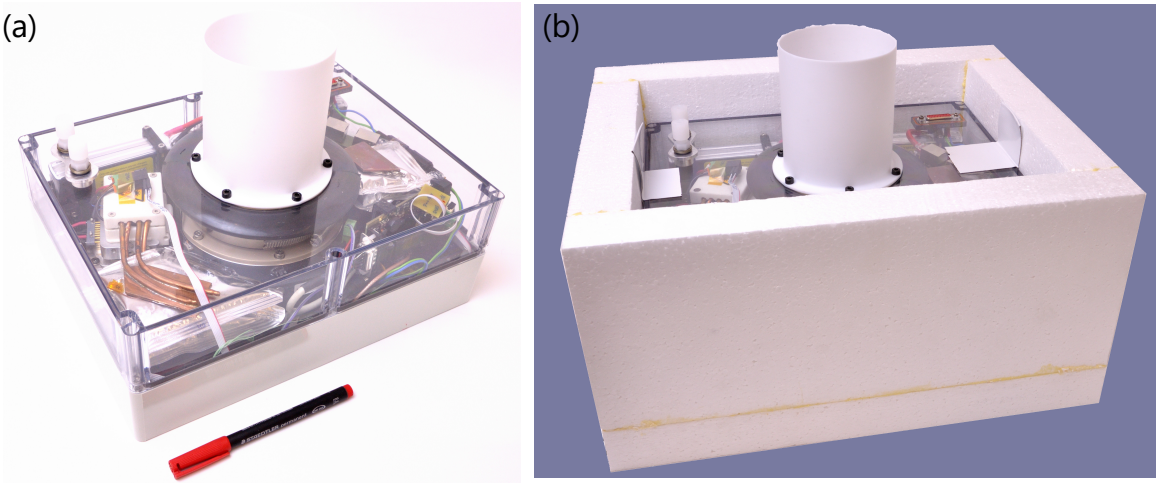

Figure 4.5: (a) Fully assembled QCLAS instrument. (b) In airborne configuration, the instrument is enclosed in XPS insulation (top lid of the insulation is removed for better visibility).

setup are required depending on the experiment. We distinguish between the (*i*) laboratory/simulation configuration used for long-term spectroscopic characterization experiments at the limit of detection; and the (*ii*) airborne/field configuration for balloon deployments with limited duration. The instrument is designed in such a way that a change in configuration only requires little effort.

Laboratory configuration	Airborne/field configuration
closed cell (coated lids)	open-path
water cooling	phase-change material (PCM)
grid power	battery power (2×4 Cell LiPo, 1800 mAh)
open enclosure	closed enclosure (pressure equilibration possible)

Table 4.2: Supported operating configurations of the instrument.

4.5 Thermal Stabilization

Thermal control and stabilization are of highest importance for laser-based spectrometers. Various strategies have been evaluated in the course of this project. A combination of actively-controlled thermoelectric cooler (TEC) and passive phase-change material (PCM) as thermal reservoir was identified to be the most suitable choice. The thermally most sensitive component is the QCL: Its active region needs to be stabilized within a few mK to avoid variation in the tuning characteristics and emission wavelength. Therefore, within the HHL housing, the laser device is

mounted directly on top of an internal TEC, which is actively PID-controlled. Although this solution efficiently dampens the surrounding air temperature fluctuations by two orders of magnitude, it is not sufficient to fully suppress temperature-induced wavelength drifts of the laser. Therefore, the HHL housing is insulated and its base plate temperature is additionally stabilized by another PID-controlled TEC.

The major difficulty is to manage the approximately 15 W excess heat produced by all electronic components. A passive coupling to the outside atmosphere through a radiator of fixed size is problematic due to the large temperature variation. It would lead to uncontrollable changes in cooling power. In fact, a passive coupling to the outside air would require a variation of the heat transfer coefficient by one order of magnitude during ascent, in order to keep the heat source at a constant temperature: While at ground conditions (as well as above ca. 20 km) efficient *cooling* is required, in between these altitude levels, a good *insulation* should protect the internal temperature from a decrease. Such a 'variable insulation' is complex and intuitively requires movable parts, which are prone to failure, especially at low temperatures.

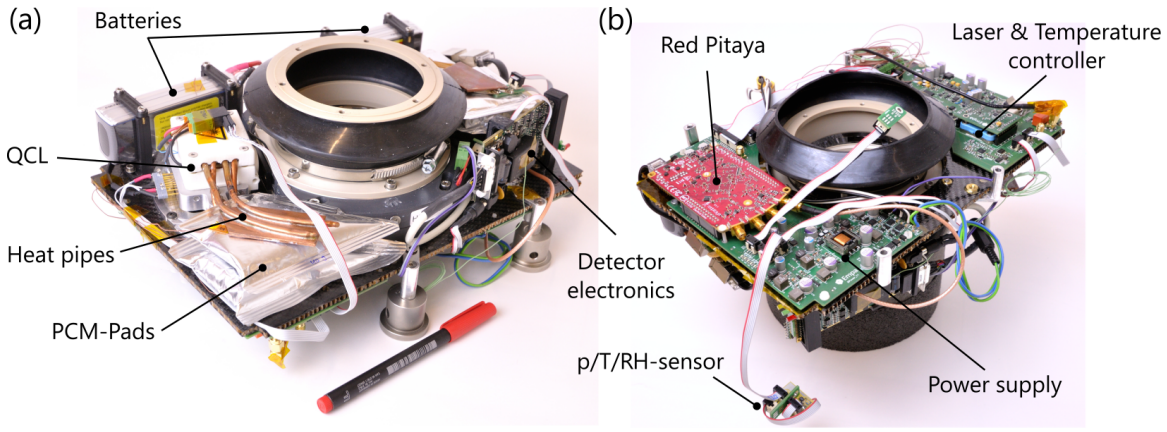

Figure 4.6: (a) Upper side of the spectrometer including the optical setup and PCM-filled pads for temperature control. (b) Bottom side featuring the custom designed electronics.

Considering the fact that the instrument has to be stabilized for a limited amount of time ($\Delta t \approx 2\,\mathrm{h}$) and the direction of heat flow changes during flight, the following approach is chosen: The instrument and the electronics are largely decoupled from the outside temperature by 40 mm of XPS. Internally, sensitive electronic devices are additionally insulated at all interfaces except one well-defined area of heat exchange. This area is coupled to a buffer medium – either directly or via sets of heat pipes in combination with a soldered copper plate to increase the area of contact to the buffer medium (cf. Fig. 4.6(a)). In order to maximize the heat capacity, the buffer medium is an organic PCM with a phase transition close to the operating temperature of the laser ($T_c = 18\,°\mathrm{C}$; RT 18 HC, Rubitherm, Germany). This adds nonlinear thermal inertia, which works bidirectionally without active control. With a combined heat capacity of 260 kJ kg^{-1} (72 Wh kg^{-1}; latent and specific heat between 11 °C and 26 °C) 416 g of PCM is required to fully take up 15 W during 2 h. Assuming a completely bidirectional use,

the amount of PCM can be halved. Depending on their heat production and their tolerable temperature range, the various electronic components are equipped with a total of 160 g of PCM, divided in adequate portions (details in Tbl. A.1). The PCM is encapsulated in custom-made pads, in form of thermally sealed aluminum plastic composite foil, containing 10–20 g and 30–40 g of PCM for the large and the small pad sizes, respectively. Under low pressure, the pads slightly expand, but no leakage has been detected during 24 h at $p < 10$ hPa. The positioning of these pads within the instrument must allow their quick and simple replacement, whereas the expansion should not lead to misalignment of the optics. To achieve this, the pads are clamped by the copper heat exchange plates in connection with the heat pipes. The pipes are stiff enough to hold the pads, but deform upon expansion of the latter such that the optical alignment remains unchanged. Tests that demonstrate the effectiveness of this thermal stabilization method are discussed in Sec. 5.3.1.

4.6 Electronics and Software

Reliable operation requires a coordinated interplay of the involved (opto-)electronic components. As depicted in Fig. 4.6(b), most of the electronic circuitry boards (PCBs) are mounted on the bottom side directly at the carbon baseplate. The core of the electronics system forms the partly open source, commercial single-board computer 'Red Pitaya' (STEMLab, 2020) featuring a field programmable gate array (FPGA) as well as microcontroller unit (MCU) able to run a GNU/Linux operating system. The FPGA on Red Pitaya has been reconfigured to provide the functionalities for high-resolution absorption spectroscopy (Liu et al., 2018).

The data management architecture within this DAQ system distinguishes between fast spectral data acquisition (125 MHz) and slow environmental data acquisition (1 Hz). Python-programmed software that ensures fail-safe operation and controlled termination runs simultaneously on the MCU. Fig. 4.8 shows the involved hardware and the data streams; Fig. 4.9 depicts the software functionalities.

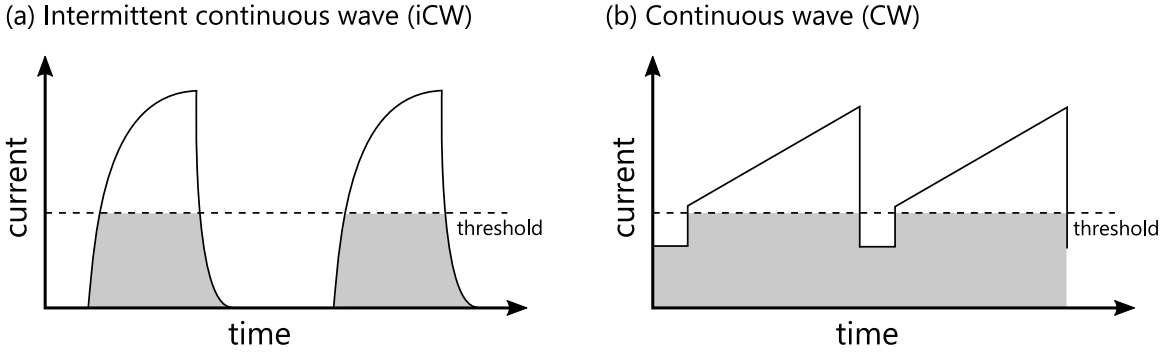

Figure 4.7: (a) 'Intermittent continuous wave' driving scheme as an economic alternative to generic 'continuous wave' operation (b), saving up to 90 % of the energy.

4.6.1 Laser Driving and Spectral Data Acquisition

The spectral sweeping of a QCL is achieved by the temperature variation of the active region, as described in Sec. 4.2. The temperature change is caused by the laser driving current, which usually consists of periodic ramps. An especially economic strategy is referred to as *intermittent continuous wave* (iCW) (Fischer et al., 2014), shown in Fig. 4.7(a): Each current ramp, supplied by the discharging of a capacitor, is followed by a moment of complete shut-down of the laser for recovering its initial temperature. In comparison to the generic CW driving scheme (Fig. 4.7(b)), iCW driving drastically reduces the energy consumption and, thus, the production of excess heat. Moreover, iCW driving extends the scanned wavelength range within one cycle. The current ramps are generated by custom-developed analogue electronics.

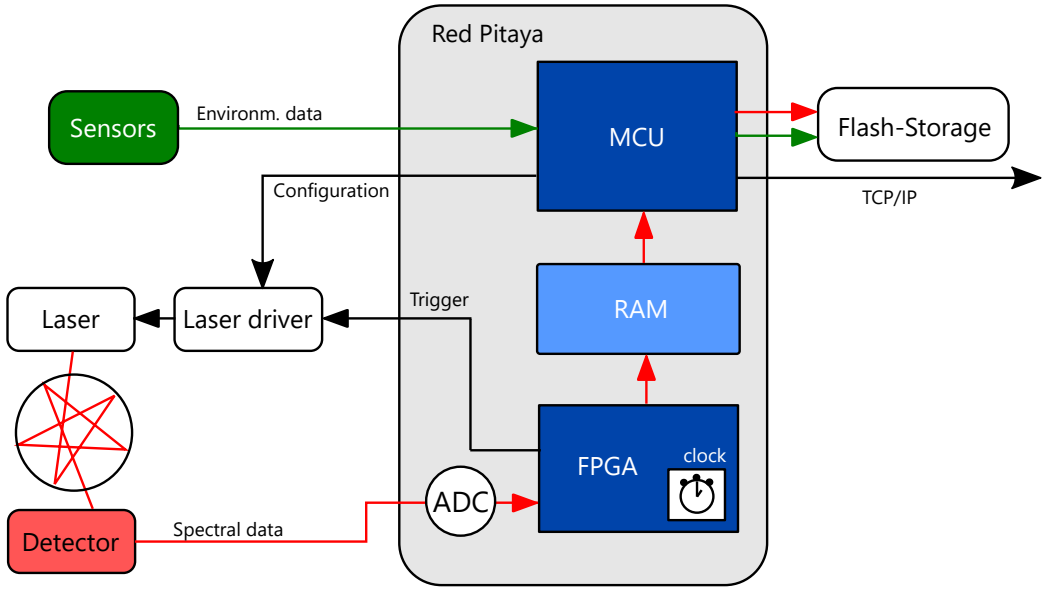

Figure 4.8: Schematic of the controlling and driving system and the involved data and communication links.

Scanning-mode operation requires fast infrared detectors. For this project, a commercially available, TEC-controlled detector based on the narrow bandgap semiconductor Mercury/Cadmium/Telluride (MCT) is used (PVM-2TE-8, Vigo System, Poland). The detector, with an active area of 1 mm^2, is encapsulated in a TO-8 housing and coupled to a small footprint preamplifier (SIP-DC-20M) with a bandwidth of 20 MHz.

The preamplified raw signal from the detector is digitized by a 14-bit analog-digital-converter (ADC) at 125 MHz, which is integrated on Red Pitaya (Fig. 4.8). Since the FPGA also provides the trigger signals for the laser-driving unit, the acquired values can be synchronized with the laser tuning and grouped to single spectra. The dedicated FPGA functionality sums up a predefined amount of individual spectra – normally a few thousand spectra within one second – in order to improve the SNR.

After completion of the spectral summation, the data is transferred to the MCU using the internal RAM in a ring-buffer scheme. The available data can be sent to an external computer in real-time via a TCP/IP-interface. For autonomous operation during flight, the data are stored on a flash memory for post-processing. The onboard saving generates about 0.2 MB s^{-1}, which is well beyond the available bandwidth for the radio-downlink as used by the radiosondes (Wendell and Jordan, 2016).

4.6.2 Environmental Data Acquisition

Internal communication for the slow environmental data acquisition is realized via the 'inter-integrated circuit' bus (I^2C). The implemented sensors either contain the relevant interface or they are grouped by a suitable microcontroller. Laser and temperature controllers are also accessed using this protocol.
Python-based software collects all relevant parameters at 1 Hz and writes the values to the flash memory. In addition to the spectroscopically relevant parameters p and T, this includes the monitoring of internal and external air temperature (T-type thermocouples), various internal diagnostic temperatures, pressure, battery-voltage, power consumption, etc. The software is designed for the simple extension to additional sensors.

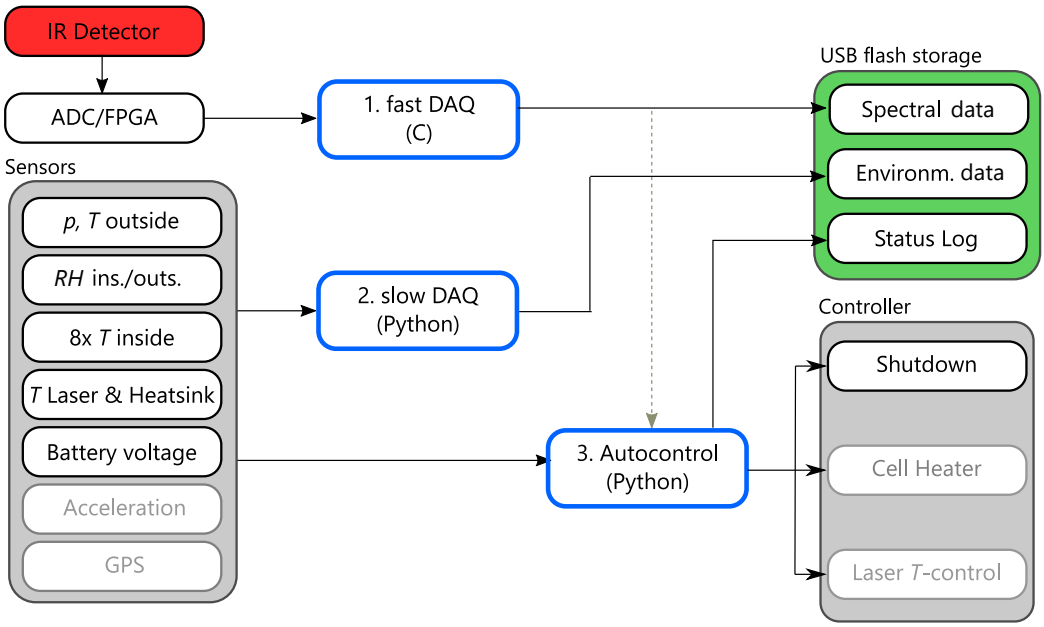

Figure 4.9: Schematic of the software running on the onboard computer consisting of 1. (fast) spectral data acquisition, 2. (slow) environmental data acquisition, and 3. the controlling unit, which directly considers certain measured quantities as input. Each of these units creates a file on the flash storage with new entries each second. Grayed out functionalities are integrated, but not yet tested in-flight.

4.6.3 Autonomous Instrument Control

In addition to the passive recording of diagnostic values, the operation of the instrument also requires some actively controlled elements. Software was developed that allows the following functionalities:
(a) A **shutdown control** turns off the instrument upon (*i*) battery under-voltage and (*ii*) pressure above 500 hPa, which prevents damage due to condensation during descent.
Further concepts have been integrated, but not activated during the first test flights:
(b) **Cell heating** can be activated to prevent icing and condensation of the MPC. A relative humidity measurement can serve as a trigger for its activation.
(c) **Spectral laser temperature locking.** The laser temperature is actively controlled by a PID-controlled TEC. This solution is sufficient in most cases, but large ambient temperature variations can still cause slight drifts of the laser emission frequency. An even tighter control can be realized by monitoring the laser emission frequency and using this parameter as feedback signal to the laser TEC controller. This approach involves a real-time spectral evaluation and absorption line position determination. However, the results obtained during the first test flights revealed that frequency stability of the laser is sufficient without additional spectral controlling.

Chapter 5

Testing and Characterization

The acceptance and the classification of any novel instrument requires rigorous testing and characterization to assess the quality of the measured data in terms of precision and accuracy. While *precision* is a measure for the agreement between independent measurements and depends on the distribution of random errors, the *accuracy* refers to the closeness of agreement with a reference value (ISO-5725, 1994). To be significant, these measurements must be performed under representative conditions. Given the wide span of temperature, pressure and water vapor concentration found during balloon flights, this is a complicated task: Simulating the full target parameter space in the laboratory requires highly demanding infrastructure. Due to the pronounced adsorption properties of H_2O, amount fractions of 10 ppmv and less, are very challenging to produce accurately. Temperatures down to −70 °C and pressures below 100 hPa can only be maintained in dedicated climate chambers. Due to the inability to cover the entire space of p, T, χ in a controlled fashion at once, a subspace of these target conditions are assessed in individual experiments.

The demanding environment that the instrument will be exposed to, leads to a trade-off between 'well-controlled' and 'realistic' conditions: In order to perform spectroscopic assessments at low χ, the instrument is used in a 'laboratory-configuration', i.e., with a closed MPC and stabilized p and T, which is only partly reflecting field-conditions. In contrast, a test-flight offers access to realistic conditions, without the ability to control any of the parameters. Therefore, a scientific approach to a rigorous characterization consists of an ensemble of experiments with incremental complexity and 'closeness' to real deployment condition. In this way, the magnitude and importance of the various influencing parameters can be identified, disentangled, and quantified.

Individual sections of this chapter are published in the peer-reviewed journal *Atmospheric Measurement Techniques* (EGU, Copernicus), Graf et al. (2020).

5.1 Closed-path Measurements

A first experimental series targets the measurement of water vapor amount fractions as observed in the UTLS at the corresponding pressure, i.e., $1 - 50$ ppmv of H_2O at $p < 250$ hPa, which enables the performance assessment of the QCLAS instrument at lower-limit conditions. For such experiments, the carrier gas must be extremely dry, and cell and gas-tubing must be completely leak-tight, since any leakage of ambient air creates significant contamination of the sample gas. Due to the surface stickiness of H_2O, gas cylinders are not suitable to store and provide stable reference mixtures. Hence, they must be generated dynamically. Therefore, the experiments were performed at the Swiss Federal Institute for Metrology (METAS) in Bern-Wabern. There, an SI-traceable gravimetric mixing unit allows to generate gas mixtures of H_2O in N_2 or air with an amount fraction below 20 ppmv at an accuracy better than 1 %. Mixtures at different concentrations and pressures were analyzed in order to evaluate the calibration-free spectroscopic retrieval, i.e., only based on measured p, T and the absorption line parameters from the HITRAN database.

5.1.1 Setup

Given the difficulties accompanied with very low concentrations of H_2O, the instrument is operated in 'laboratory-configuration': The multipass cell (MPC) is closed with two aluminum lids, creating an effective sampling volume of 100 ml. The lids, as well as all tubes in contact with the gas mixture, are SilcoNert®-coated. SilcoNert® (SilcoTek, USA) is a highly inert coating that minimizes the adsorption of molecules on the surface, thereby shortening the response time and reducing hysteresis. The

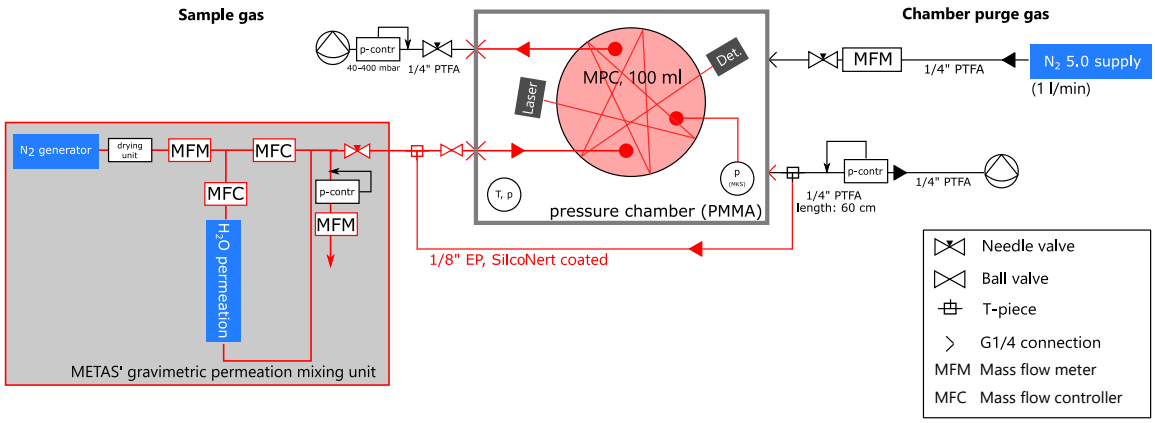

Figure 5.1: The highly accurate water vapor reference is supplied by the gravimetric mixing unit (left) and carried directly into the closed MPC, which is located within a pressure chamber. This chamber is purged by dry N_2 (right) in order to stabilize the absorption contribution outside the cell.

laser beam is coupled into the MPC through CaF_2-windows which are sealed with nitrile O-rings. For long-term stable operation, a water-cooling system keeps the laser

heat-sink, detector, and electronics at a constant temperature. In addition, the entire system is mounted within a hermetically sealed pressure chamber (cf. App. B) to reduce fluctuations of temperature and pressure. Fig. 5.1(a) shows the experimental setup as used at METAS. The core part of the gravimetric mixing unit consists of a semipermeable tube containing H_2O. This tube is attached to a high-precision balance, which detects the decrease of mass. At stable pressure and temperature, the permeation-rate is constant, thus, water vapor is continuously admixed to the gas that streams past the permeation tube. Through variation of the gas flow, exact mixtures can be generated (Haerri et al., 2017).

5.1.2 Spectral Evaluation

The generic approach to evaluate the absorption spectra, as measured by the QCLAS, is described in Sec. 2.3. In this experiment, however, the spectra are more complex due to the additional absorption outside the closed MPC (Fig. 5.2(a)). The different pressure broadening leads to the observed spectrum, which is a superposition of a broad and a narrow absorption line. While the narrow part originates from the 6 m OPL within the MPC at low pressure and low concentration, the broad part is due to the 2.7 cm OPL outside the MPC held at high pressure. The placement of the entire setup within the pressure-controlled chamber enables a stabilization of this contribution. However, the lowest achievable χ within the pressure chamber is 2000 ppmv.

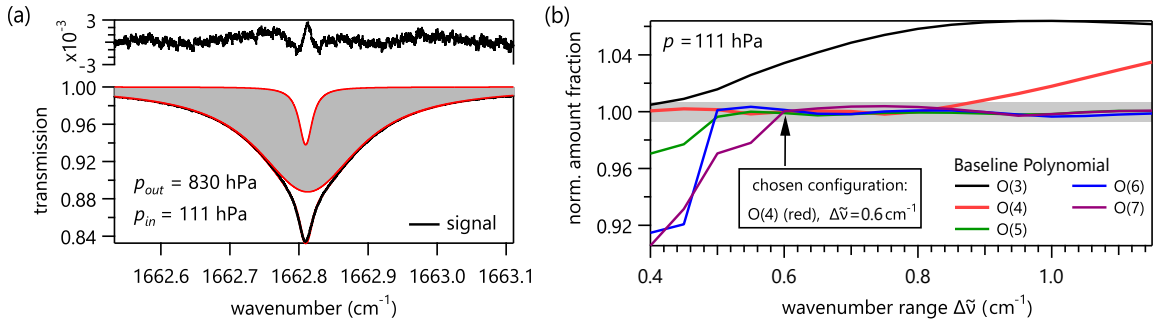

Figure 5.2: (a) Typical spectrum with a small and narrow absorption line from inside the MPC (low pressure) superposed with a broad absorption feature originating from 2.7 cm path length between laser/detector and MPC (high pressure, gray). The local residual noise level on the data amounts to $2\sigma = 5.8 \times 10^{-4}$. (b) Investigation of the robustness of various fitting configurations. The retrieved amount fraction, normalized to the result of the finally chosen configuration, is shown as a function of the fitting range. This is done for different polynomial orders used to describe the baseline. The gray area denotes the $\pm 0.7\,\%$ range.

As long as the pressures inside and outside the MPC differ significantly, the two absorption contributions are separated accurately by the fitting algorithm without any further constraints. In contrast, the size of the spectral fitting window and the

order of the baseline-polynomial are not a priori defined. However, the choice of these parameters has a clear impact on the retrieved amount fraction: Polynomials of too high orders on narrow spectral sections potentially interfere with the absorption feature, while too low order polynomials fail to adequately reconstruct the curvature of the baseline. To examine the dependence of polynomial order and spectral range, this parameter space is analyzed for each pressure encountered in this experiment. For $p = 111\,\mathrm{hPa}$, the situation is shown in Fig. 5.2(b). The retrieved χ is robust and lies within $\pm 0.7\,\%$ for a broad range of fitting presets, as indicated by the gray area. Furthermore, a 4^{th} order polynomial yields the same result irrespective of the full width of the fitting window within $0.4 < \Delta\tilde{\nu} < 0.8\,\mathrm{cm}^{-1}$. Since this applies to all pressures used in the following experiments, a combination of $P_4(\tilde{\nu})$ and $\Delta\tilde{\nu} = 0.6\,\mathrm{cm}^{-1}$ was used to evaluate the spectral data.

5.1.3 Precision

Precision refers to the random variation among individual measurements and is a requirement for accurate data. In laser spectroscopy, an important source of randomness is the noise of the spectral data. In this experiment, the precision is assessed at low SNR, i.e., at conditions similar to the UTLS in pressure and concentration. An expressive means to quantify precision of a spectrometer is the calculation of the Allan-deviation (Allan, 1966; Werle et al., 1993), where the evolution of precision as a function of the averaging time is quantified. For this measurement, the sampling volume is held at $\chi = 18.5\,\mathrm{ppmv}$, $p = 0.108\,\mathrm{hPa}$, and $T = 296\,\mathrm{K}$ by continuous purging. For H_2O measurements, obtaining drift-free conditions is extremely challenging due to sorption-effects: Even for high flows and low sampling volumes, it can take hours for the asymptotic behavior to cease. Therefore, the raw data in Fig. 5.3 is corrected for this trend by an exponential regression. Single values for the amount fraction χ are acquired at 1 Hz, after co-averaging of 3000 individual spectra. After 1 s, an Allan-deviation of 5.5 ppbv (0.03 %) is obtained. The instrument is stable enough such that the Allan-deviation decreases upon averaging over many tens of seconds. For sake of comparison with other spectrometers, the precision may be expressed in terms of *absorption noise* σ_{AN}, as defined by

$$\sigma_{\mathrm{AN}} = \frac{\sigma_{\mathrm{Allan}} \cdot A}{\chi} \tag{5.1}$$

where A denotes the spectral absorption maximum and χ the measured amount fraction. In the present system, $\sigma_{AN} = 1.18 \times 10^{-5}$ which corresponds to $1.94 \times 10^{-8}\,\mathrm{cm}^{-1}$ if normalized with the absorption path length of the MPC.

Two additional aspects were characterized in the above setup: (*i*) The linearity of the QCLAS measurements and (*ii*) the effect of variations in the sample pressure. Fig. 5.4(a) shows measurements at four different gravimetrically generated amount fractions and at four different sample pressures. The systematic and constant offset is caused by contamination of the reference gas due to diffusion, as discussed in the next section. Therefore, the results can only be compared relative to each other. The slope of a linear fit onto these data points is plotted in the inset of Fig. 5.4(a), showing a

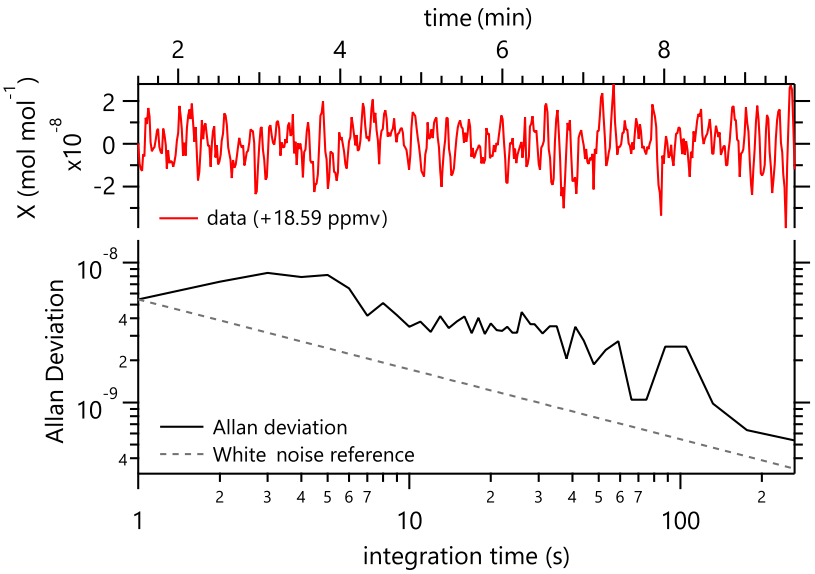

Figure 5.3: Allan-deviation plot after removal of an exponential trend at p, T-conditions similar to the UTLS ($\chi = 18.5\,\text{ppmv}$, $p = 0.108\,\text{hPa}$). At one second acquisition time, the precision is 5.5 ppb (0.03 %) and it further decreases upon longer averaging. The measurement shows an oscillation with a period of 9 s, likely originating from the mass flow controller in the generator, leading to a local increase of the Allan deviation.

minor but correlated deviation from unity. This deviation is explained by a pressure dependence of the measurements, as shown in Fig. 5.4(b). We find the retrieved χ to deviate by up to 16 % in correlation to the sample pressure, compared to their high-pressure asymptote. Similar effects are documented in literature: Buchholz and Ebert (2018) reported an overestimation of spectroscopically measured amount fractions at low p of the order of 10 %. They assign the effect to the known limitations of the Voigt profile to describe absorption lines at low pressure. However, the magnitude of the observed deviation in the present data exceeds the error that is expected from the absorption line profile. Therefore, I hypothesize a pressure dependence of the observed contamination effect to explain the surplus of deviation.

5.1.4 Accuracy

The goal of this project is to *accurately* measure water vapor amount fractions on an absolute scale. Accuracy is a combination of precision (s. above) and *trueness*, which denotes the deviation from the measured value to the unknown, *real* one or, at least, an accepted reference (ISO-5725, 1994). In the context of water vapor measurements, the assessment of trueness is especially challenging, since both, the measurement as well as the generation of unperturbed reference mixtures are extremely difficult.

In principle, the gravimetric mixing unit at METAS delivers H_2O amount fractions with an accuracy better than 1 %. However, to assure this level of accuracy,

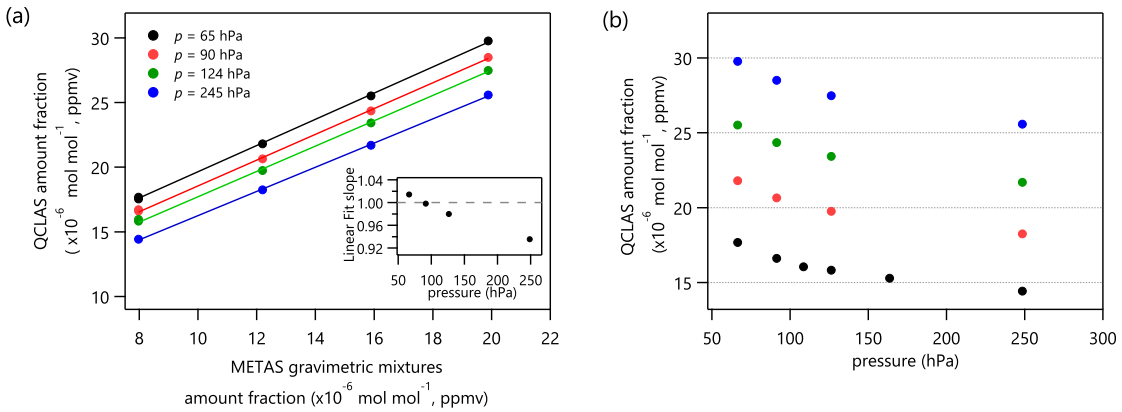

Figure 5.4: (a) Water vapor amount fractions measured by the QCLAS as a function of the gravimetrically generated mixture. The inset shows the slope of a linear fit through the data points, each with a coefficient of determination $0.9993 < R^2 < 1$. Error bars – denoting the precision of the individual measurement – are smaller than the size of the markers. (b) QCLAS measurements of constant H_2O mixtures at different pressures.

a perfect and leak-tight sealing of the attached sampling volume, i.e., the MPC in this case, is required. Despite considerable efforts to enhance its tightness, the lowest achievable leakage rate of the MPC was 10^{-5} mbar l min^{-1}. Given the five orders of magnitude higher partial pressure of H_2O in the surrounding air, the reference gas becomes rapidly contaminated. Even the evacuation of the enclosing pressure chamber to pressures below the one of the MPC did not prevent H_2O to diffuse into the sampling volume. As a result, the measured amount fraction is systematically wet-biased compared to the reference value and exhibit a sample flow-dependence. As a consequence of this permeation-based mixing concept, the sample flow through the MPC and the level of dilution are not independent, which likely caused the observed deviation in linearity.

Therefore, a bottom-up uncertainty budget (Tbl. 5.1) provides an estimate for the expected accuracy, assuming uncorrelated and linear dependence of the measured amount fraction χ on the individual parameters. This is an approximation insofar as the (uncertain) broadening parameter ($\gamma_{\mathrm{air}}(p)$) is used as input for the fitting procedure, potentially leading to an unpredictable and non-linear distortion by forcing the fit to a wrong minimum. For instance, the fitting procedure may try to compensate for a slightly wrong a priori width of the profile by assimilation of the baseline-polynomial, eventually resulting in a wrong number density. This is especially problematic for strongly broadened absorption lines that cover large parts of the fitting range. A comparison of the obtained amount fraction for different fitting configurations, as shown in Fig. 5.2, can reveal such inconsistencies. However, the ultimate quantification of this dependence requires the comparison with a reference gas of known concentration. To estimate the uncertainty induced by the fitting procedure in this experiment, we take the confidence interval of $\pm 0.7\,\%$ found in Fig. 5.2

Parameter	uncertainty of parameter	distrib.	std. uncertainty on χ, σ_χ (%)
Line intensity S_{ij}	$< 2\,\%$	tri.	0.82
Broadening parameter γ_{air}	$< 1\,\%$	tri.	0.41*
Temperature T	$\pm 1\,\text{K}$	rect.	0.18
Pressure p	$1\,\%$	rect.	0.58*
Fitting configuration	$0.7\,\%$	rect.	0.41
Voigt profile (relative)	$2\,\%$	norm.	2*
Combined standard uncertainty $\sigma_{c,\chi}$			$2.4\,\%$

Table 5.1: Uncertainty budget for the closed cell experiment measuring dynamically generated reference mixtures of H_2O in N_2. The uncertainty on the line parameters are taken from the HITRAN2016 database. The error due to the fitting configuration is estimated from fitting studies as shown in Fig. 5.2. T and p uncertainty is taken from the specification of the corresponding sensor. The marked (*) uncertainty directly influence the fitting quality, potentially leading to non-linear deviations of χ. Further contributions below $0.1\,\%$ are omitted.

and consider it a rectangular distribution. Thus, it enters the uncertainty budget of standard deviations after division by $\sqrt{3}$ (BIPM, 2008). Each contribution to the uncertainty is converted into standard uncertainty according to its probability density distribution. The potential deviation caused by the limited complexity of the Voigt profile is estimated to $2\,\%$ within the considered pressure range Lisak et al. (2015). The combined uncertainty is found by taking the square-root of the summed variances. In conclusion, the observed pressure-dependent deviation cannot be explained by the estimated uncertainty, which is another indication for a variable contamination in the system.

5.2 Open-path Measurements

5.2.1 Setup

Given the aforementioned difficulties to establish stratospheric conditions within the closed MPC, the setup is adapted: In this experiment, the spectrometer is now used in open-path configuration and placed in a custom-made pressure chamber of 60 l volume, described in App. B. The pressure within this chamber can be reduced below 5 hPa, allowing the simulation of altitudes higher than 30 km. In order to support operation during many hours, the temperature of the most sensitive electronics is stabilized by an external water-cooling system. The pressure chamber can be flushed with dry gas or specific water vapor mixtures at different pressures.

Within this chamber, the analyzed air is exposed to a large surface area, mostly from materials with suboptimal properties with respect to water adsorption, such as PMMA (chamber surface) or 3D-printed plastics. Thus, the lowest achievable amount fraction of water vapor is 2000 ppmv, only reached by flushing with dry N_2 for several hours. At such concentration, the absorption line, selected for measurements at the UTLS ($\nu_{ij} = 1662.8\,\mathrm{cm}^{-1}$), is fully saturated and, therefore, not suited for the accurate retrieval of amount fractions (Fig. 5.5(a)). This limitation can be circumvented by using a different absorption line: In direct vicinity of the originally selected transition, a series of smaller absorption lines exist that are accessible by a slight adjustment of the laser operation temperature. These lines are about 1000 times weaker than the one at $1662.8\,\mathrm{cm}^{-1}$. Therefore, at lowest achievable humidity within the pressure chamber, their absorbance is similar to the originally selected line at UTLS conditions (Fig. 5.5, inset). Thus, even though the effective H_2O concentration is three orders of magnitude higher, the measurements have similar SNR as in the UTLS. As a result, stability and precision assessments are representative. The transition at $1665.7\,\mathrm{cm}^{-1}$ is used for the analyses within this section.

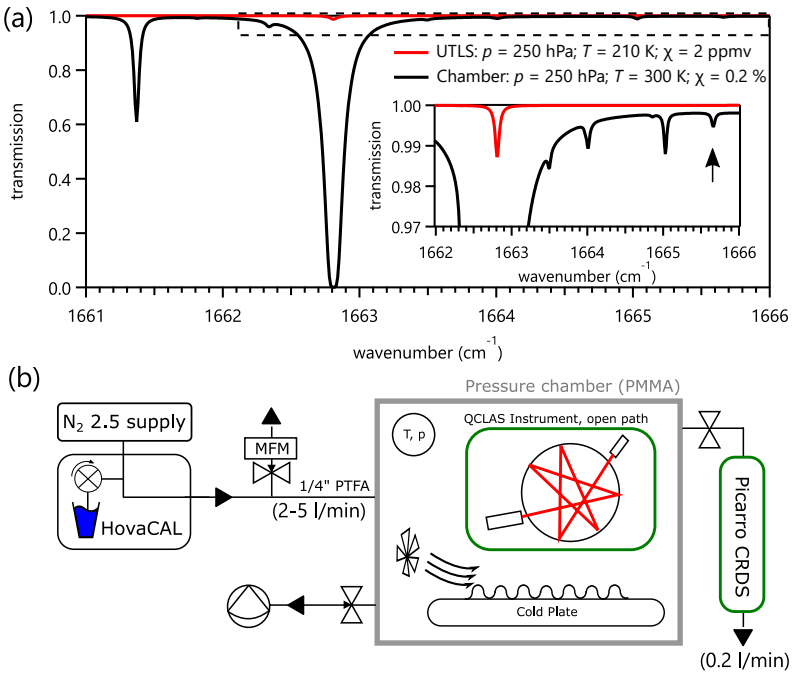

Figure 5.5: (a) Water vapor spectrum for UTLS conditions (red) and for minimal achievable concentration in the pressure chamber (black), shown as survey and close-up (inset). Due to the Lorentzian tails of neighboring lines, the narrow features are offset, which complicates the evaluation. The chosen transition is marked with an arrow. (b) The setup offers two methods of controlling the humidity inside the pressure chamber: A gravimetric generator (HovaCAL) and a TEC-controlled cold plate.

5.2.2 Reference Methods

Active and passive strategies were applied to achieve control over the water vapor concentration within the chamber.

5.2.2.1 Active Methods

In a first series of experiments, well controlled H_2O/N_2 mixtures are provided by a dynamical generator unit (HCD311, HovaCAL, IAS GmbH, Germany). The setup is illustrated in Fig. 5.5(b): The basic idea is identical to the experiments at METAS, except that the MPC is now open and the entire instrument exposed to the sample gas. The permeation source used at METAS is replaced by a HovaCAL-generator, which uses a peristaltic pump to dose liquid water to an evaporator (170 °C) where it is admixed to a controlled flow of carrier gas (Tuzson et al., 2017). The setup was configured to deliver H_2O amount fractions between 0.2 and 6 % calculated with respect to *wet* carrier gas.

In a second series of experiments, a cold plate, which is integrated in the pressure chamber, is used to control the humidity (Fig. 5.5(b)). The cold plate is equipped with fins to increase its surface area and a fan provides internal convection. Mounted on Peltier elements, the plate can be cooled down to -11 °C. Provided that there is sufficient moisture, the cold plate temperature can constrain the water vapor content of the air to 100 % relative humidity, since no gas exchange is allowed during the experiment. If the saturation vapor pressure is exceeded, water is removed from the air by forming a condensate on the cold surface. The amount fraction χ as a function of the cold plate temperature T_p can be calculated by

$$\chi(T_p) = \frac{e_s(T_p)}{p_c} \tag{5.2}$$

where e_s is the saturation vapor pressure and p_c the pressure inside the chamber. Various empirical approximations exist for $e_s(T_p)$. Here, the Buck-equation (Buck, 1981) is used; its accuracy is reported to be better than < 0.02 % in the applied temperature-range.

Even though the surface of the cold plate is enlarged by metal fins, the mixed air temperature is not significantly altered, due to the lack of thermal insulation of the chamber. Thus, an air-parcel, dried at the cold plate may already be re-moistened by water outgassing from all other surfaces, before being measured. Additionally, the determination of the effective cold plate temperature, i.e., a metal surface exposed to strong forced convection, is prone to errors. Due to the exponential dependence of the saturation pressure on T, the assumed temperature error $\sigma_T = 0.25$ K manifests in a significant uncertainty of $e_s(T)$ as denoted by the error bars in Fig. 5.7.

5.2.2.2 Passive Methods

Alternatively, the passive monitoring of the amount fraction by a second instrument can yield a reference value. Two instruments were used: A dew point hygrometer

(DPH; 973S, MBW Calibration AG, Switzerland) and a cavity ring-down spectrometer (CRDS; Model G2401, Picarro Inc., USA) containing a pressure-controlled cavity held at 200 hPa under continuous flow. Thus, with the CRDS, chamber pressures below 200 hPa are inaccessible. The instrument has been calibrated against a LI-COR 610 generator ($\chi_{\mathrm{ref}} = 1.0315\chi_{\mathrm{CRDS}}$). Since the DPH failed to deliver stable results especially at low pressures, the range of available conditions for the cross-validation is very limited.

5.2.3 Spectral Evaluation

For both experiments, the QCLAS spectra are evaluated by a Voigt fit onto a spectral window ranging from 1665.46 to 1665.91 cm^{-1}. The fitting procedure takes into account all 272 transitions between 1600 and 1700 cm^{-1} with an intensity $S_{ij} > 10^{-24}$ cm molec^{-1}. This is required to accurately reconstruct the absorption background due to the strong neighboring absorption lines at these high H_2O concentrations (cf. Fig 5.5(a)). In addition, the trace gas approximation, which assumes that the amount fraction of the measured gas is small, is no longer valid. Therefore, self-broadening has to be taken into account in the fitting process.

5.2.4 Results and Discussion

For most experiments, the above methods were combined: While controlling the humidity, using either the HovaCal-generator or the cold plate, the CRDS was measuring simultaneously. In a first experiment, QCLAS and CRDS measured H_2O amount fractions at a constant chamber pressure for different water vapor mixtures generated by the HovaCAL instrument. The relative deviation of the measured values χ_{meas} from the gravimetrically controlled set value χ_{set} is plotted in Fig. 5.6(a). These results show considerable deviation among the generated concentration and the CRDS measurement. Therefore, the consistency among the generator and the CRDS is assessed in a cross-validation: The pressure chamber is bypassed and the generator is directly attached to the inlet of the CRDS analyzer. In contrast to the above deviations, a linear fit reveals excellent agreement:

$$\chi_{\mathrm{CRDS}} = 0.9889(5)\chi_{\mathrm{HovaCal}} \quad \text{with} \quad R^2 = 1.0013$$

This high level of agreement implies considerable perturbation of the generated mixture due to sorption or condensation effects within the chamber or the tubing. Based on this fact, the CRDS is taken as a reference for this experiment. Comparing the QCLAS measurements with the calibrated CRDS at 253 hPa, a deviation of 1.9(4) % is found, as shown in Fig. 5.6(b). The error bars denote the precision given by the standard-deviation (0.4 %) of the averaged amount fraction as measured at each χ_{set} at 1 Hz.

To achieve even lower pressures and to circumvent losses of humidity within the tubing, a second experiment employs the in-situ moisture-control using the internal cold plate. The starting water vapor concentration is chosen sufficiently wet such

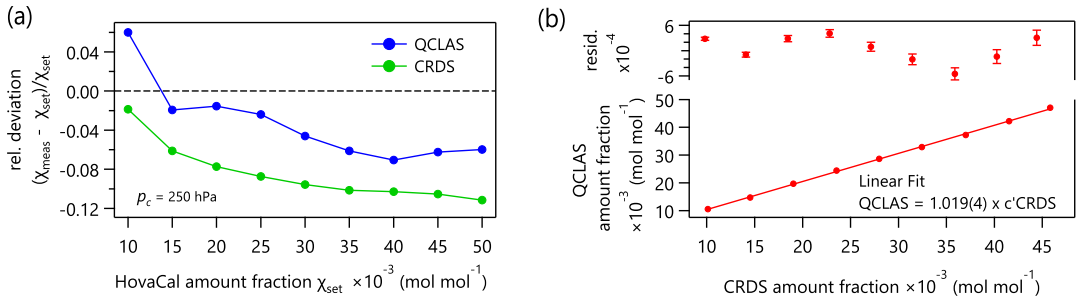

Figure 5.6: (a) Relative deviations of the values measured by the QCLAS and the CRDS with respect to the amount fraction provided by the generator at $p_c = 253\,\mathrm{hPa}$ (b) Linear fit ($R^2 = 1.018$) to the QCLAS humidity measurements plotted against CRDS, which is taken as a reference.

that enough water is present to keep 100 % RH at any time for a given cold plate temperature T_p. Fig. 5.7(a) shows the deviation of the measured amount fractions χ_{meas} from the calculated amount fraction assuming 100 % RH at T_p. The error bars in both dimensions are due to the uncertainty on the calculated humidity given by the uncertainty related to the measurement of T_p. The deviation between CRDS and QCLAS are considerably higher than in the previous experiment, suggesting inhomogeneous moistening with the chamber – therefore, the CRDS measurement is not a suitable reference for this experiment. This is underscored by the direct comparison in Fig. 5.6(b), revealing a deviation of 15 % between CRDS and QCLAS. Thus, a direct validation of the cold plate method is not possible with this setup, however, since the cold plate is located close to the measurement zone of the QCLAS, the use of the calculated amount fractions based on T_p appears trustworthy within the stated uncertainty.

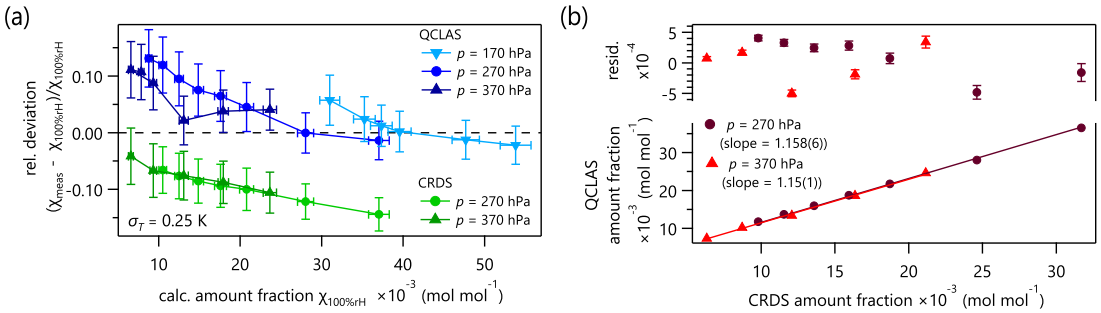

Figure 5.7: (a) Relative deviation of the measured amount fraction by QCLAS ad CRDS with respect to the cold plate reference. The uncertainty of the cold plate temperature σ_T is estimated to $\pm 0.25\,\mathrm{K}$, represented by the error bars. (b) Direct comparison between QCLAS and CRDS reveals considerable disagreement among the methods for this experiment.

In accordance with the generator-based experiment, the relative deviation curves all show a similar slope (Fig. 5.6(a)), suggesting a certain concentration dependence. Since this effect is consistent among the measurement methods and the reference methods, it seems systematic, likely caused by sorption phenomena within the chamber. Correcting the QCLAS data for the contamination dependence identified with the CRDS, under the assumption that the humidity is least perturbed at high values, the QCLAS data lie within 6 % of the reference – which is within the uncertainty of the reference value, as denoted by the error bars in Fig. 5.6(a).

These experiments impressively demonstrate the difficulties with regard to providing accurate water vapor mixtures at conditions comparable to the UTLS. In conclusion, we find the water vapor amount fraction, as retrieved by calibration-free measurement, to deviate by 1.9(4) % from the calibrated reference instrument for pressure conditions at the upper edge of the target region. In-situ humidity control enhances the range of accessible pressures, however, the limited accuracy of the corresponding reference value strongly limits the detailed analysis of the involved uncertainties.

5.3 Assessment in Climate Chambers

In the above-presented experiments, the instrument's performance is assessed by comparing the humidity measurement to reference mixtures or reference measurements. However, this strategy cannot be followed in the entire range of expected conditions, lack of suitable references. At extreme conditions, the behavior of the instrument is examined by temperature measurements at various locations within the device. The system is exposed to UTLS-comparable temperatures in a climate chamber which does not allow to control pressure or humidity. Therefore, low-pressure experiments have been conducted in a separate chamber that is described in Sec. 5.2 and App. B.

5.3.1 Temperature

The temperature resilience of the QCLAS instrument is assessed in a climate chamber that allows cooling of the air below −60 °C (VCS 7033, Vötsch). The instrument is prepared in its airborne configuration (cf. Sec. 4.4) including the XPS insulation and PCM pads. The temperature sequence is programmed in accordance to the expected conditions during a balloon ascent. The climate chamber does not support the variation of pressure. Since the reduced pressure at higher altitude alters the heat transfer properties of the air, this effect is accounted for by a correction of the minimal temperature ($T_{\mathrm{min}} = -45\,°\mathrm{C}$ instead of $-60\,°\mathrm{C}$) based on a heat transfer calculation. Internal fans create turbulent convection within the chamber. Fig. 5.8 shows the temperature evolution at specific spots within the instrument as well as the surrounding air during the experiment. Temperature-critical components (denoted with an asterisk) are thermally connected to PCM to increase their thermal inertia. The temperature measurement at these objects shows a characteristic kink due to the phase transition of the PCM. For instance, the temperature increase of the onboard

computer is successfully limited by its contact to ca. 45 g of PCM. More critical is the stabilization of the laser heat-sink: In addition to the laser device itself, the baseplate temperature T_{LaserHS} of the laser housing is actively controlled by a TEC. The excess heat, produced by this TEC, is drained into a PCM-pad; the temperature at this interface is plotted in Fig. 5.8 (black curve). The maximal $\Delta T_{\mathrm{LaserHS}}$ of 5 °C leads to a variation of the laser device temperature of $\Delta T_{\mathrm{Laser}} = 14.2\,\mathrm{mK}$ during the entire duration of the experiment i.e., over 1.5 h. Thus, the efficient coupling to PCM in combination with two stages of actively controlled TECs suppresses the variation of the laser temperature by 35 dB. The remaining variation of T_{Laser} translates into a laser drift of $1.6 \times 10^{-3}\,\mathrm{cm}^{-1}$. If uncorrected, this detuning would lead to an error of the retrieved water vapor amount fraction of 0.44 %.

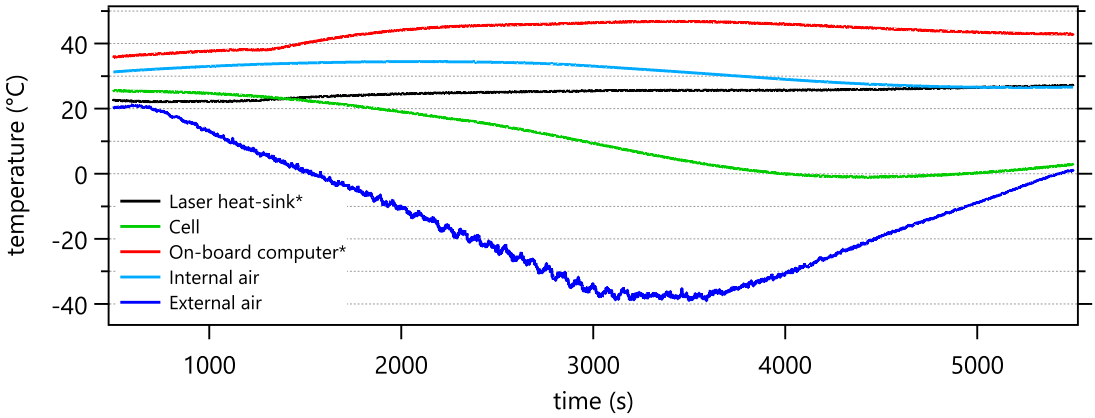

Figure 5.8: Temperature evolution at different locations and devices within the spectrometer for a simulated ascent to UTLS in a temperature chamber at normal pressure. Objects with an asterisk are thermally connected to a PCM reservoir, therefore showing a characteristic kink, which is caused by the phase transition of the PCM.

5.3.2 Pressure

The focus of this experiment lies mainly on investigating the mechanical stress exerted by a pressure reduction. Temperature and humidity remain uncontrolled. For instance, low pressures lead to an expansion of the PCM pads, potentially causing misalignment on the optical system. In addition, pressures below 10 hPa are beyond the certified specifications of many electronic devices, either because of their constituents (e.g. electrolyte capacitors) or lack of adequate cooling by the restricted natural convection at low pressures.

The tests reveal that the incorporated electronic devices and the PCM pads resist pressures of 10 hPa for the duration of a UTLS balloon flight. In addition, the expansion of the PCM pads is absorbed by the bending of the connecting heat pipes, leaving the optical alignment unchanged. In fact, the experiments at low pressure

demonstrate that the instrument shows stable operation for up to 2 h even at room temperature, which exacerbates the thermal situation. This proves the usability of this system under a wide span of conditions.

5.4 Test Flights

As a final assessment and culmination of this project, two test flights with the QCLAS instrument were conducted from the Meteorological Observatory Lindenberg (MOL), Germany, in collaboration with the German Weather Service (DWD). The DWD-station in Lindenberg is the lead centre of the *GCOS Reference Upper-Air Network* (GRUAN), launching radiosondes on a daily, and cryogenic frost point hygrometers (CFH) on a semimonthly basis, having therefore highly experienced personnel in balloon deployments and instrument recovery. MOL has permanent clearance for payloads up to 4.5 kg. In addition, the site is surrounded by flat terrain which facilitates recovery. The deployments of the QCLAS were accompanied by quasi-simultaneous ascents of a CFH instrument, serving as reference for the measured humidity.

5.4.1 Targets

These test flights finalize the series of characterization experiments ranging from *well-controlled* to *realistic* conditions, as described in the course of this chapter. For the first time, the QCLAS is simultaneously exposed to extreme p, T, and χ. The comparison with a CFH instrument provides an important quality measure, as CFH represents the currently accepted standard method. The focus is set on the UTLS as the defined 'high priority' range (350–60 hPa, i.e. 8–20 km altitude). In addition, it is important to check the performance and reliability of all subsystems (e.g. DAQ, temperature control, etc.) under extreme conditions.

5.4.2 Flight Details and Setup

On 17$^{\text{th}}$ and 18$^{\text{th}}$ of December 2019, the QCLAS was brought up to 28.3 km and 27.4 km, respectively; aboard of a helium-filled weather balloon (TX 1200, $V = 3\,\text{m}^3$; cf. App. A.3 for more details). The payload was attached 45 m below the balloon and combined with a radiosonde (RS41, Vaisala) and a GPS locator. A second balloon, carrying the CFH instrument, was launched 37 min and 7 min before lift-off of the QCLAS for Flight I and Flight II, respectively. The QCLAS instrument was set to its airborne configuration as described in Sec. 4.4.3.1. The instrument is optimized for ascending measurements: The MPC opening is extended in upward direction by a Teflon duct of 86 mm diameter to avoid contamination by the insulation, sticking out 60 mm over the surface. No such extension was added on the downward facing side, i.e., contamination by the insulating material may be of concern during descent. The internal volume was purged with dry air until a few minutes before launch. Spectral data were recorded at 1 Hz, corresponding to 3000 co-averaged single spectra during ascent and descent. The system was automatically shut down after the exceedence

of $p = 500\,\mathrm{hPa}$ (below 5 km altitude). Shortly before scheduled shutdown, a loss of signal was observed, due to dew formation on the MPC. Strong westerly winds carried the balloon over 200 km eastwards, as shown in Fig. 5.9. After Flight I, the instrument was recovered undamaged and reused the next day without modification.

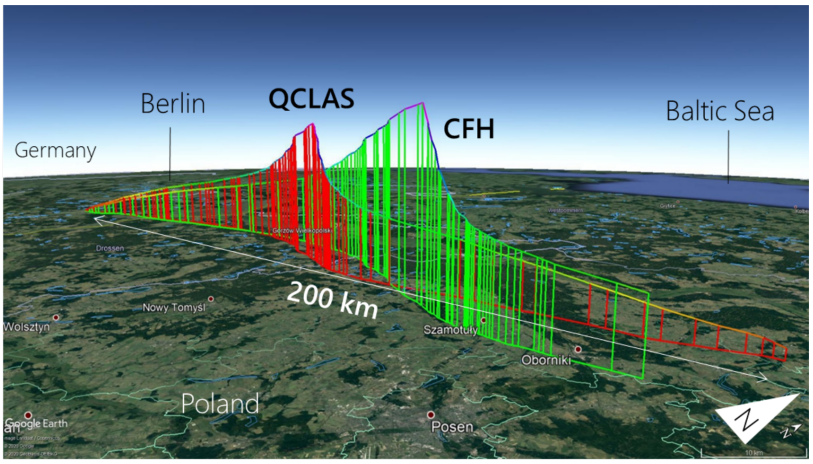

Figure 5.9: Flight trajectories of the QCLAS (red) and CFH (green) during Flight I. The starting time delay was 37 min between CFH and QCLAS.

5.4.3 Evaluation of Spectra

Examples for measured spectra are given in Fig. 5.10(a). At low pressure two main features are clearly recognizable: A sharp one, originating from the atmospheric measurement, and a broad component, which is not influenced by the outside pressure and remains constant during flight. According to its linewidth, the absorption happens within a gas portion at $p \approx 1000\,\mathrm{hPa}$. The only places where high pressure is maintained during flight are the inside of the laser and the detector housings. Assuming 3 mm OPL within these housings, fitting of this feature yields an internal H_2O amount fraction of $\chi_{\mathrm{intern}} = 2.8\,\%$ (cf. Fig. 5.10(b)). Although the manufacturers ensure packaging under dry atmosphere, degassing and diffusion processes have apparently led to the accumulation of water vapor within the optoelectronics housings over time. This optoelectronics-related contribution can be disentangled by explicit fitting of both components using the corresponding pressure as a preset parameter. The calculation of the amount fraction relies on the measured values for p and T from the RS41 radiosonde, although the QCLAS contains such sensors on its own. However, temperature measurements in the UTLS are delicate and strongly dependent on the location and integration of the sensor (Dirksen et al., 2019). To avoid uncertainties of this kind, the values are used from the well-characterized RS41 radiosonde.

For the accurate derivation of the atmospheric humidity, it is important to recall that the OPL of the MPC is 609.4 cm (cf. Ch. 4.4.2). In addition, there is a short section of optical path between the MPC and both the laser and the detector. This distance amounts to $z_{\mathrm{int}} = 9\,\mathrm{mm}$ or 0.14 % of the total OPL. Despite the initial

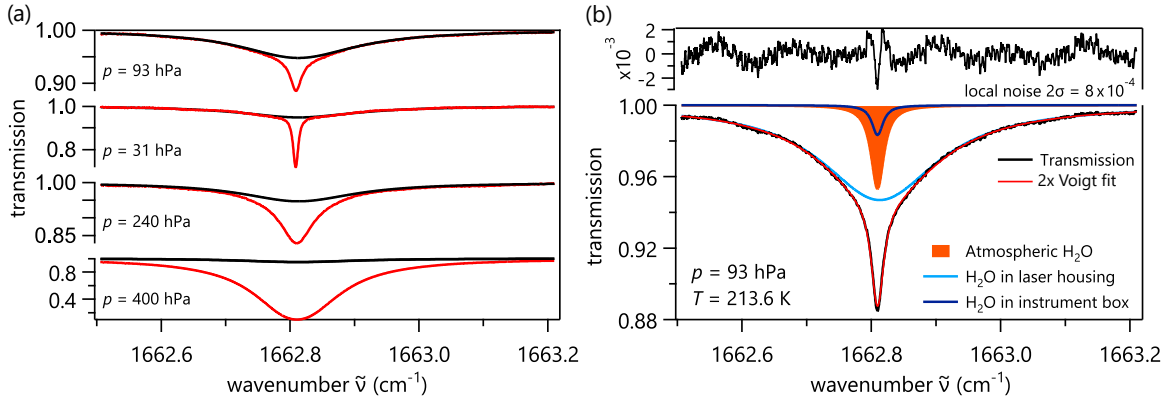

Figure 5.10: (a) Measured normalized spectra at different pressures/altitudes. (b) Typical decomposition of the absorption contributions for a spectrum at 16.1 km altitude.

purging of the instrument, degassing and diffusion lead to increasing humidity within the enclosure, such that the internal absorption becomes comparable in magnitude to the external one at altitudes higher than about 200 hPa (11.7 km). Therefore, the derived amount fraction from the narrow absorption feature χ_{tot} must be corrected for the absorption which is caused by the internal humidity. Due to the inability to maintain a pressure difference between the instrument's enclosure and the surrounding atmosphere, the internal moisture is deduced by a capacitance humidity sensor. Using Eq. 2.3, the combined number density of H_2O molecules n_{tot} along the total OPL z_{tot} is found by fitting. In this case, z_{tot} is split into an internal part with z_{int} at T_{int} and an external atmospheric part z_{out} at T_{out} while $p_{\mathrm{int}} \approx p_{\mathrm{out}}$. The exponent in the Beer-Lambert law can be, to first order, decomposed as

$$n_{\mathrm{tot}} z_{\mathrm{tot}} S_{ij}(T_{\mathrm{out}}) \approx \frac{p\chi_{\mathrm{int}}}{k_B T_{\mathrm{int}}} z_{\mathrm{int}} S_{ij}(T_{\mathrm{int}}) + \frac{p\chi_{\mathrm{out}}}{k_B T_{\mathrm{out}}} z_{\mathrm{out}} S_{ij}(T_{\mathrm{out}}) \tag{5.3}$$

using $n = \frac{p\chi}{k_b T}$. The equation can then be rearranged using $s_{\mathrm{x}} := \frac{S_{ij}(T_{\mathrm{x}})}{T_{\mathrm{x}}}$:

$$\chi_{\mathrm{out}} \approx \chi_{\mathrm{tot}} - \chi_{\mathrm{int}} \frac{z_{\mathrm{int}} s_{\mathrm{int}}}{z_{\mathrm{out}} s_{\mathrm{out}}} \tag{5.4}$$

assuming $z_{\mathrm{int}} \ll z_{\mathrm{out}}$ such that $z_{\mathrm{tot}} \approx z_{\mathrm{out}}$.

A more rigorous treatment requires an explicit spectral decomposition of the two absorption features, as shown in Fig. 5.10(a). In that case, the internal absorption line is reconstructed according to the measurements of $p_{\mathrm{int}}, T_{\mathrm{int}}, \chi_{\mathrm{int}}$, while χ_{out} is optimized by the fitting procedure.

5.4.4 Results

The amount fraction measured by the QCLAS at 1 Hz resolution is displayed in Fig. 5.11(a) for both CFH and QCLAS at ascent and descent. Frost point temperatures are converted into amount fractions using the Goff-Gratch relation (Murphy and

Koop, 2005). Comparison between QCLAS and CFH is only possible for Flight I due to problems with CFH during Flight II, where we observed strong contamination at ascent and no plausible data was received upon descent. In Fig. 5.11(a), the displayed QCLAS data are shown both uncorrected, as well as after the attempt to correct for the internal absorption using Eq. 5.4 for the descent data. For better comparison to the slower CFH, the corrected QCLAS data set is smoothed by a 20 s moving-average filter. The internal humidity data provided by a low-cost sensor enables the removal of the general trend, but fails to achieve realistic absolute values due to its limited accuracy between 0 and 10 % RH.

Below the tropopause, where the contribution of internal humidity is negligible with respect to the atmospheric H_2O abundance, the agreement between CFH and QCLAS is very good, as shown in Fig. 5.11(b). The calibration-free retrieval yields highly accurate results even at low altitudes, where the scanned spectral window is already partly saturated. In the right panel of this figure, the relative deviation of the amount fractions of the two instruments is plotted, showing a mean deviation of 3 % which indicates the absence of a significant systematic offset. The standard deviation (indicated as gray area) amounts to 13 % between 2 and 10 km altitude. Highest deviations are observed around sudden changes, which is likely due to the short-scale and rapid spatiotemporal changes in the tropospheric humidity in combination with the launch time delay and the slight difference in trajectory (Fig. 5.11(c)). The faster response time of the QCLAS with respect to CFH may additionally contribute to these deviations.

5.4.5 Discussion

The high-resolution QCLAS data in Fig. 5.11(a, inset) show strong and rapid variations at altitudes higher than ca. 200 hPa (11.8 km). While these variations may, at first sight, appear to be measurement noise, they exhibit a clear structure: The upper inset of Fig. 5.12, showing χ_{QCLAS} versus time in the stratosphere, reveals that the signal contains individual spikes above a slowly varying background. Furthermore, these spikes follow a certain regularity: A Fourier transform analysis indicates a favored oscillation periodicity of $\tau_1 = 6.5\,\mathrm{s}$ and $\tau_2 = 12.4\,\mathrm{s} \approx 2\tau_1$ in the occurrence of these spikes. Assuming an ideal pendulum as a simple model for describing the instrument's motion below the balloon, $\tau_p = 2\pi\sqrt{L/g} = 13.5\,\mathrm{s}$ is obtained considering the rope length $L = 45\,\mathrm{m}$, as used in the experiment. An analysis of the in-flight GPS data confirms this periodicity of oscillation and indicates maximal inclinations of 18° during ascent. Therefore, it is very likely that the spikes are caused by the measurement of contaminated air due to periodic transitions through the wake of the balloon. Another strong evidence for this hypothesis is the immediate disappearance of these spikes after the burst of the balloon, as shown in Fig. 5.12. Upon descent, the variation of the signal becomes more symmetric and amounts to as little as $\sigma_{\mathrm{sdev}} = 3.4\,\%$ for the non-averaged data acquired at 1 Hz. This variation, though, is not caused by noise in the spectrum, but it is a reproducible result of real variations of the humidity level. Since the QCLAS instrument was not optimized for descent measurements, i.e., no teflon duct at the bottom side, the observed variation during

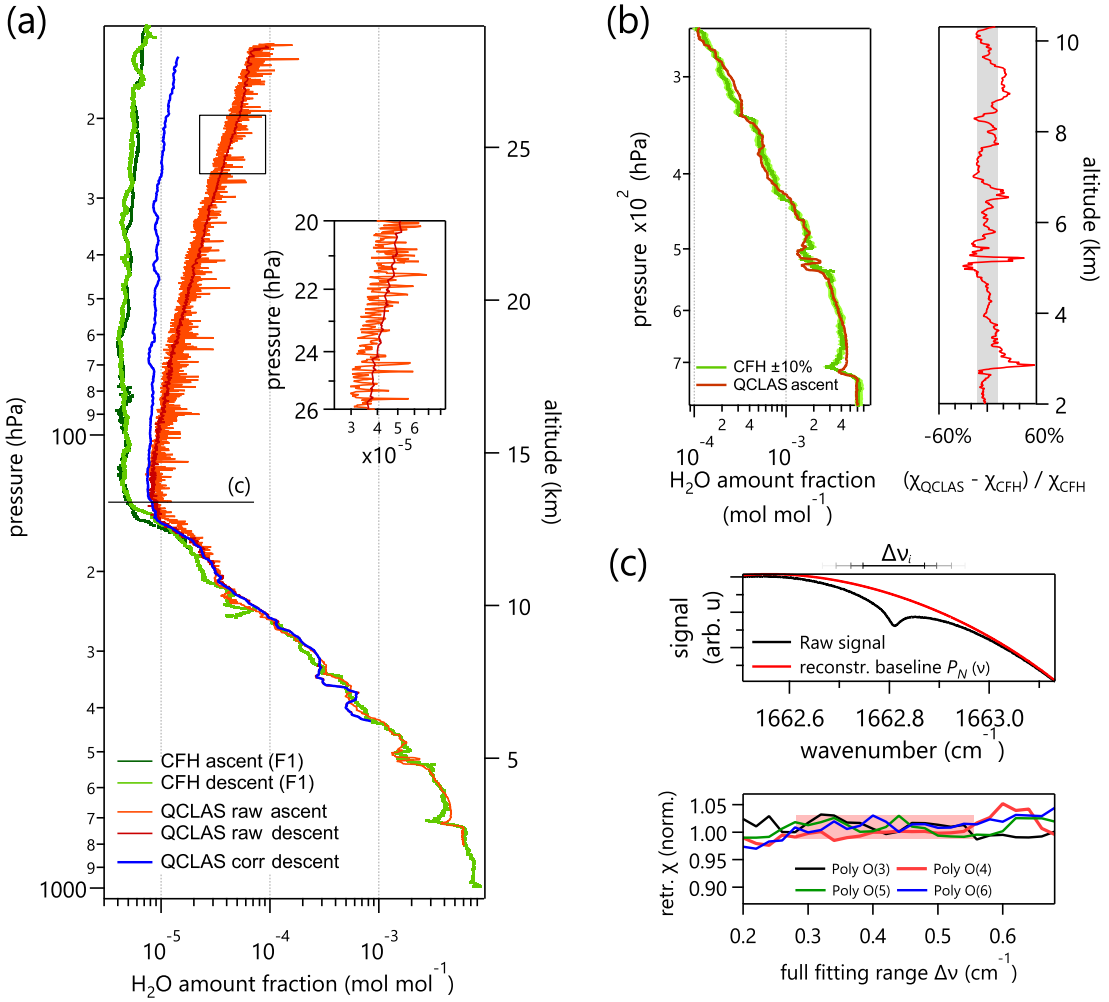

Figure 5.11: (a) Measured amount fractions during Flight I by the QCLAS and CFH for ascending and descending motion. The increasing values from the QCLAS in the stratosphere are due to the accumulation of humidity inside the instrument. An attempt to correct for this effect leads to the blue curve. The inset shows the unilateral peak structure on the ascent-data which is associated to the pendulum motion through the water vapor contaminated wake of the balloon. (b) Comparison of QCLAS and CFH data during descent in the troposphere. The envelope around the CFH dataset denotes the range of ±10 % and serves as a guide to the eye. A detailed uncertainty analysis of the QCLAS data is given in Sec. 5.4.6. In the right panel, the relative deviation is plotted, showing a standard deviation of 13 % (highlighted gray). (c) Fitting stability test: The same spectrum – acquired at the tropopause ($p = 141$ hPa) – is analyzed using different fitting ranges and background polynomials as illustrated in the upper panel. The lower panel shows the retrieved amount fraction as a function of the fitting range. Further details are given in the uncertainty discussion (Sec. 5.4.6).

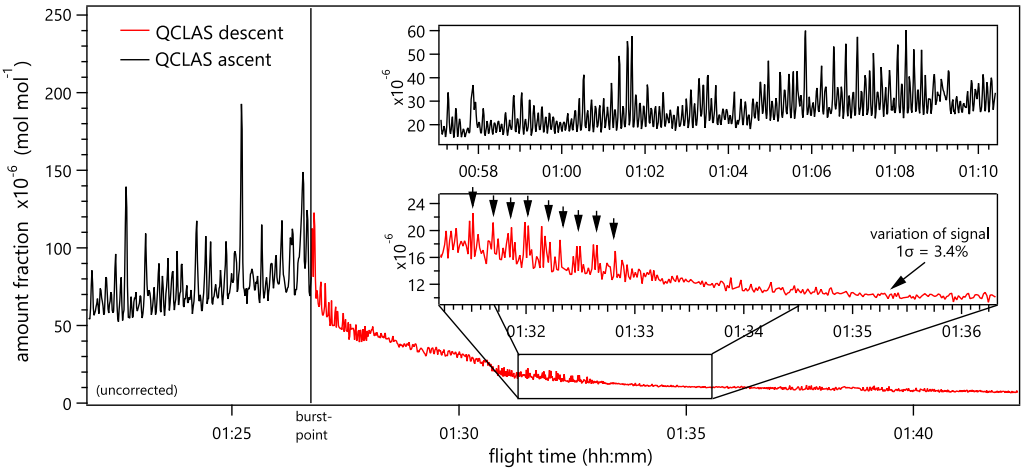

Figure 5.12: H_2O amount fraction measured by QCLAS as a function of time around the burst point ($p = 16$ hPa) without correcting for the internal humidity. As insets, close-ups to the data displaying the spike structure during ascent (top inset) and descent (bottom inset).

descent could be due to the measurement of self-contaminated air. Indeed, also the descent data exhibit periodicities in its fluctuation, as denoted by arrows of roughly 10 s distance in the lower inset of Fig. 5.12.

5.4.6 Uncertainty Contributions

The accumulation of internal humidity is discussed above and represents the dominant uncertainty contribution at altitudes above 200 hPa (11.8 km). Apart from this effect, the spectrometer-related sources of uncertainty can be quantified in a bottom-up uncertainty budget, which includes the following main contributions:
(*i*) **Laser drift**. During the flight, the mean temperature of the laser changes by 19 mK, resulting in a drift of the emission frequency by $\Delta\tilde{\nu} = 2.1 \times 10^{-3}\,\mathrm{cm}^{-1}$. This leads to a variation of the wavenumber scaling with respect to the primarily determined $\frac{\mathrm{d}\tilde{\nu}}{\mathrm{d}t}$ using the Fabry-Pérot etalon. The associated change in water vapor amount fraction is quantified to 0.76 %, which could potentially be accounted for in the evaluation procedure. However, such a correction is not considered in the current evaluation and the corresponding maximal error is therefore included in the uncertainty budget.
(*ii*) The measured **OPL** has an uncertainty of ±3 mm (0.05 %). In addition, thermal expansion alters the OPL during flight. A maximal $\Delta T_{\mathrm{cell}} = 54$ K is measured within the target region. Using $\alpha_{\mathrm{Alu}} = 23 \times 10^{-6}\,\mathrm{K}^{-1}$ yields an OPL change of 0.12 %. The thermal expansion was not specifically treated in the calculations, and the corresponding maximal error is thus considered in the uncertainty budget.
(*iii*) p, T**-measurement**. The pressure uncertainty is given by 0.5 % and the temperature uncertainty by 0.4 K (< 0.2 %), according to the specifications of the radiosonde (Vaisala, 2020). These values denote standard deviations.

(*iv*) **Spectral noise** is the main source of random error, and thus limits the precision. During flight, the relatively low normalized spectral noise level of $2\sigma = 1 \times 10^{-3}$ is dominated by optical fringes that are caused by stray light within the MPC. This corresponds to about 2.5 times more noise than under ideal laboratory conditions and is likely due to impurities or particles on the open-path MPC. Assuming that the precision of the retrieved amount fraction scales linearly with the spectral noise level, the in-flight precision is estimated to 0.075 %, i.e., 2.5 times the Allan-deviation of 0.03 %, as determined in the laboratory-based experiment at 1 Hz (cf. Sec. 5.1.3).
(*v*) **Fitting configuration and baseline reconstruction**. During flight, the curvature of the zero-absorption baseline can vary, e.g., due to low frequency fringes or slight changes in the optical alignment. In order to account for such variation, the polynomial, taken for the baseline reconstruction, must be of sufficiently high order. This induces additional degrees of freedom to the fit procedure, potentially leading to an undesired bias. To quantify the stability of the fitting procedure, the same spectrum is analyzed using different fitting configurations, following the procedure explained in Sec. 5.1.2. Such comparisons are performed at various pressures. As expected, the scatter is highest when the contrast of the absorption line is lowest, i.e., the height divided by the width is small. This is particularly the case at the hygropause, where the ambient pressure is still relatively high, while the H_2O concentration is very low. However, Fig. 5.11(c) shows that even for low contrast spectral conditions, the deviations in H_2O amount fraction are small among reasonable fitting configurations (red area). A standard deviation of 1.1 % relative to the chosen configuration of $\Delta\tilde{\nu} = 0.4\,\mathrm{cm}^{-1}$ and $P_4(\tilde{\nu})$ is found within this region.
(*vi*) Accuracy of the **absorption line parameters**. According to the HITRAN database, the uncertainty σ_S for the spectral line intensity is given by $1\,\% \leq \sigma_S < 2\,\%$ for this transition. The uncertainty of the broadening parameter $\gamma_{\mathrm{air}}(p_{\mathrm{meas}})$ is stated with $< 1\,\%$. However, to what extent the uncertainty of the broadening parameter impairs the fitting result, is difficult to predict analytically and depends on the spectral situation. Therefore, as a conservative estimate, a maximum uncertainty of 1 % is included in the budget.
(*vii*) The **Voigt profile deficiency**. As discussed in Sec. 2.2.2, the Voigt profile does not account for the full complexity of a rovibrational transition, leading to the characteristic 'W'-shaped residuals. This deviation can vary with changing pressure, and thus affect the accuracy. The effective error induced by this limitation strongly depends on the selected transition and can only be quantified experimentally by measuring a reference gas. Studies in the near-IR spectral region report differences in the reconstructed absorption line integral of up to 5 % between Voigt and higher order profiles (Lisak et al., 2015); however, their deviation goes to zero as the pressure is reduced. Therefore, for the UTLS region (< 250 hPa) an upper limit for the systematic profile-induced error is estimated to 1.25 %.
The contributions summarized in Tbl. 5.2 yield a spectrometer-related uncertainty of 2.94 % for the UTLS region. It should be noted, however, that this overall uncertainty does not consider the effect of internal humidity accumulation.

In conclusion, the first flight campaign was technically successful and very instructive. The thermal management strategy, incorporating a combination of PCM and

Parameter	relative uncertainty contribution in %
Absorption line	
Line intensity S_{ij}	$2^{(1)}$
Broadening parameter γ_{air}	$1^{(1)}$
Setup	
Thermal variation of OPL	$0.12^{(1)}$
Laser drift/tuning rate	$0.76^{(1)}$
Measurement	
Temperature T	0.2
Pressure p	0.5
Fitting	
Fitting config. & baseline	1.1
Voigt profile	$1.25^{(2)}$
Combined uncertainty σ_χ	2.94

Table 5.2: Uncertainty budget for the retrieved H_2O amount fraction χ during the test flights in absence of the internal humidity accumulation problem. [1]For contributions with strong dependence on the external conditions (e.g. pressure or temperature) the maximal uncertainty enters the calculation. [2]conservative estimation for the Voigt profile-associated uncertainty for $p < 250\,\text{hPa}$. Contributions below 0.1 % are omitted.

TEC, provided the required stabilization of the internal temperature. Also, the optical alignment remained stable and the cell stayed clean during the entire flight. The thermal inertia of the MPC and the attached bodies is sufficient to maintain a temperature difference that prevents condensation – except for the lowermost 5 km at descent. The high temporal resolution unveiled important information about contamination issues during ascent: The clear balloon-wake signature detected by the QCLAS seriously queries the adequacy of ascending measurements for high accuracy stratospheric humidity soundings. Measurements during descent show remarkably lower contamination, even though the QCLAS instrument is not yet optimized for that. The intercomparison between the QCLAS and CFH shows a mean deviation of 3 % and a standard deviation of 13 % within the troposphere, most likely dominated by the slightly different flight trajectories and response times of the two instruments. A bottom-up uncertainty budget suggests an accuracy of 2.94 % in the UTLS region. However, due to the accumulation of humidity within the QCLAS in the stratosphere, the experimental verification of this value was hindered.

5.5 Further Developments

The flight tests have proven the applicability of the QCLAS in the UTLS and its ability to deliver high-precision measurements. Concerning the achievable accuracy, there

are currently two major limitations that should be addressed by future work: Firstly, the perturbation of the measurement due to the accumulation of internal humidity, and secondly, the bottom-up uncertainty estimate of 2.94 % should be experimentally verified and further confined.

5.5.1 Absorption by Internal Humidity

In order to expand the range of reliable measurement to altitudes beyond 15 km, the absorption due to the accumulation of humidity inside the instrument must be solved or its measurement improved. Indeed, sensors exist with better – and documented – performance at low pressure (Lorek, 2014). However, since the humidity inside the enclosure lies between 0-10 % RH, a capacitive measurement is always prone to uncertainties. Therefore, further strategies are conceivable to solve the problem of internal absorption, however, these options require more or less fundamental adaptations on the spectrometer:
(*i*) Clearing the gap between laser/detector and cell by optical fibers appears the ideal solution. However, especially in the mid-IR spectral region, fiber coupling is generally difficult and usually produces a loss of intensity, optical feedback, and fringes. These fringe patterns are sensitively dependent on pressure and temperature as well as acceleration-driven variations in the alignment of the coupling optics.
(*ii*) Splitting the laser beam in front of the MPC, directly guiding one part onto a second detector, allows the spectroscopic measurement of the internal H_2O content. This is the most accurate solution and it additionally offers better access to the baseline as well. Even the inclusion of a reference cell may be considered. However, it complicates the acquisition process, requires more power and cooling capacity, and implies significant adaptations of the optical layout.
(*iii*) Attaching the laser and the detector in direct contact to the cell appears a simple solution. The same holds for the idea of flushing the gap with atmospheric air. These concepts were initially discarded considering the sensitivity of the optoelectronic components with respect to temperature variation. However, this solution may be re-evaluated, now that the influences and sensitivities were examined during the balloon-borne tests.
(*iv*) The most promising way to overcome this limitation is to establish a leak-tight connection between the laser (detector) and the MPC to maintain ground pressure for the OPL outside the MPC. Thereby, the absorption due to the gas outside the MPC is strongly broadened and remains – especially at higher altitude – easily distinguishable from the absorption signal of atmospheric water vapor. This may be accomplished by a flexible tube or a miniaturized bellow that still allow changes of the laser (detector) alignment, but on the same time ensures a thermal decoupling from the MPC.

5.5.2 Spectral Evaluation

To further improve and characterize the accuracy of the calibration-free spectral retrieval and the performance of the instrument within a broad range of conditions, I recommend the following steps:

The uncertainty, associated with the spectral evaluation, should be further reduced. This is achieved by a comparison of different fitting configurations not only with each other, but also relative to an accurate water vapor reference. Additionally, the parameters for the calculation of the absorption cross-section should be verified experimentally, while the use of higher order profiles can further reduce the uncertainty. The required additional parameters must be determined experimentally as well. These steps involve controlled conditions and accurate reference mixtures. The experiment described in Ch. 5.1 and the infrastructure at METAS are, in principle, suitable for this assessment. However, leakage of the MPC must be reduced by at least one order of magnitude, e.g., by using welded pipe connections and improved window holders on the MPC.

Finally, the impact of environmental perturbations should be examined in more detail, i.e., the precision of the measurement should be experimentally verified in the full range of pressure, temperature and humidity conditions. This requires a sophisticated climate chamber (e.g. AIDA (Fahey et al., 2014)) which allows to control each critical parameter (p, T, χ) independently. Following these steps, a complete characterization of the instrument can be achieved as well as a detailed verification of each contribution of uncertainty.

5.5.3 Future Adaptations of the Instrument

The following issues may be addressed or optimized in the future:
(*i*) The importance of contamination from the material used in the measurement funnel could not yet be quantified. However, minor constructional adaptations could reduce the surface area exposed to the air upstream of the MPC, e.g., by covering the teflon duct and the nitrile bellows with a stainless steel-sheet. Additionally, the same construction may be applied on the downward facing side of the QCLAS, optimizing the instrument for bidirectional use.
(*ii*) The enclosing box may be reconstructed with a more lightweight material than the currently used PCT. The use of carbon composite materials additionally enhances stiffness and insulating properties. This adaptation potentially saves up to 500 g.
(*iii*) Balloon-borne deployments offer very limited control over the landing site. This is a major drawback in combination with instruments that have to be recovered, either lack of a data-downlink or because of the expensive payload. While an onboard, real-time evaluation can potentially be integrated, there is little chance that the costs of the main components will significantly decrease in the near future. An appealing option to reduce the effort of recovery could lie in the combination of the QCLAS instrument with an UAV that autonomously returns to the launch site after the burst of the balloon, e.g., along the lines of the 'return glider' presented by Kräuchi (2016).

Chapter 6

Conclusions

This thesis addressed the challenge of frequent and highly accurate water vapor measurements in the UTLS. To this end, a direct absorption QCL spectrometer was developed that combines high sensitivity and accuracy in a lightweight, robust, and autonomous instrument, which operates reliably under the full range of temperature, pressure, and humidity encountered during balloon soundings from the ground up to the UTLS. The corresponding implementation required a fundamental reconsideration of the spectrometer design.

The initial theoretical work targeting the optimization of mask-enhanced toroidal MPCs, triggered the development of a novel MPC concept, called *segmented circular multipass cell* (SC-MPC), which is tailored for lightweight and robust spectrometers. Such MPCs show very low optical noise levels and have already found their application beyond the framework of this project, e.g., in Tuzson et al. (2020). Since the SC-MPC is highly tolerant with respect to the input laser beam characteristics, beam pre-shaping optics that are generally required for conventional MPCs, can be omitted. This results in an unprecedented reduction of complexity, higher compactness of the optical setup, and therefore to lower weight and enhanced robustness of the instrument. The combination of the SC-MPC together with specialized laser driving and DAQ electronics enabled the realization of an integrated instrument with an overall weight of merely 3.9 kg and a volume of $30 \times 23 \times 11\,\mathrm{cm}^3$.

The internal temperature stabilization of the spectrometer, realized by a combination of actively controlled thermoelectric cooling and phase-change material as a buffer medium, was proven to be highly efficient. Thereby, the external temperature variation is suppressed by almost five orders of magnitude during balloon deployment. This creates the possibility to use the highly temperature-sensitive QCLs for tunable laser spectroscopy even under harsh environmental conditions.

Laboratory-based characterization experiments demonstrated a precision of the water vapor measurements better than 0.1 % under pressure and humidity conditions representative for the UTLS. The assessment of the instrument's accuracy turned out to be highly challenging, especially at low concentration of the sticky and ubiquitous H_2O molecules. Diffusive contamination and sorption effects impaired the exact knowledge of the reference concentration. Therefore, several independent techniques

were applied to ensure perturbation-free reference mixtures or reference measurements within a subspace of the expected environmental conditions. The comparison of the calibration-free QCLAS measurements to a calibrated CRDS instrument at 250 hPa showed an excellent agreement of 2 %.

The field tests, conducted at the end of the project, consisted of two balloon flights of the QCLAS up to 28 km altitude, accompanied by simultaneous CFH launches. It marked the first ever deployment of a QCL-based absorption spectrometer in the UTLS aboard of a low-volume balloon. The successful continuous measurement both at ascent and descent illustrated that the instrument is well-suited for balloon deployments. The accomplishment of repeated flights on two consecutive days further demonstrated the feasibility of frequent and flexible deployments at reasonable effort. The high temporal resolution of the QCLAS instrument enabled the identification of considerable balloon-related contamination during ascent, observed as individual wake-transitions. Upon descent, these contamination events disappeared, underscoring the importance of descending measurements for highly accurate H_2O data in the UTLS. Such highly resolved measurements can shed light on the long-standing debate concerning the magnitude and importance of balloon-related contamination (Jorge, 2019). However, the QCLAS instrument yields sufficient spatial resolution also upon descent, when balloon-related contamination is not of concern. The comparison to CFH showed good agreement (mean deviation of 3 %) in the troposphere ($p > 250$ hPa) and the calibration-free retrieval has proven robust and reproducible over the whole span of conditions. Above 11 km altitude, the QCLAS measurements are currently limited by spurious absorption due to the accumulation of water vapor within the instrument, which can, however, be solved by future technical adaptations. This issue hindered an experimental verification of the estimated uncertainty, although, the instrument showed stable spectroscopic operation even in the stratosphere, where an accuracy of 3 % was estimated by a bottom-up uncertainty budget.

In conclusion, this project represents a significant advance in miniaturization of high-precision laser absorption spectroscopy in general. Furthermore, it demonstrates the technical feasibility of frequent, flexible and high-resolution water vapor measurements in the UTLS. The experimental characterization strongly indicates that QCLAS has the potential to complement and possibly substitute cryogenic frost point hygrometry. Clearly, a more detailed performance assessment in a broader range of conditions is still required to establish QCLAS as a reliable technique for UTLS water vapor measurements. This particularly involves the comparison to other instruments both in-flight and under controlled conditions, e.g., by participation in upcoming intercomparison campaigns.

Appendix A

QCLAS – Additional Information

A.1 Summarized Specifications

Property	Details
General	
Method	tunable QCL absorption spectroscopy
Sampling technique	ambient pressure, open-path
Total mass	3.86 kg
Mass of spectrometer only	2.60 kg (w/o enclosure and insulation)
Dimensions w/o insulation	$(300 \times 230 \times 110)\,\mathrm{mm}^3$
Dimensions w/ insulation	$(380 \times 310 \times 190)\,\mathrm{mm}^3$
Measurement funnel diameter	86 mm
Power consumption	15 W
Batteries	2x 4C LiPo 14.8 V (1800 mAh)
Operating Time	> 2 h
Spectroscopy	
Laser	DFB-QCL at 6 µm; $P \approx 10$ mW
Detector	TEC-controlled MCT
Multipass cell	SC-MPC with 6 m OPL
Monitored Transition	$221 \leftarrow 212$ (J, K_a, K_c) at $1662.809\,\mathrm{cm}^{-1}$
Data acquisition rate	1 Hz
Acquisition method	3000 co-averaged spectral sweeps
Performance	
Precision	$< 0.1\,\%$
Accuracy	3 % (bottom-up estimation)
Agreement to CFH	3 % (mean deviation at $p > 250$ hPa)
Costs (material only)	CHF 10,000 – 15,000.–

A.2 Power Consumption and PCM Distribution

Device	Power (W)	ΔT (K)	m_{PCM} (g)
Laser	1.1	10^{-3}	70 [(a)]
Laser driver	2.1	30	–
Laser internal TEC	1.5	1[1]	70 [(a)]
Laser internal TEC controller	1.5	1	70 [(a)]
TEC at laser heatsink (PWM)	2	5[1]	70 [(a)]
SoC 'Red-Pitaya'	4	30	45
Detector	– [2]	10	45
Detector controller	2.8	10	–
Total	15		160

Table A.1: Estimated average power consumption of the incorporated electronics, their acceptable temperature fluctuation range and the amount of PCM attached. [1]For TECs, the T-variation at the uncontrolled side is denoted. [2]Detector power consumption is included in the controller. [a]These devices share the amount of 70 g PCM.

A.3 Balloon-borne Test Flights – Details

Launch site:
Meteorological Observatory Lindenberg (52.2135 N, 14.12 E)

	Flight 1 (17.12.2019)	Flight 2 (18.12.2019)
Conditions		
Clouds	Ac str tr Ci fib	Sc str op du
rel. humidity (%)	87.0	74.0
Pressure (hPa)	994.6	1003.7
Temperature (°C)	5.6	9.6
QCLAS		
Liftoff time	09:51:59	09:43:02
Unwinder length	45 m	45 m
Burst altitude (km)	28.296	27.380
Ascent rate ($\mathrm{m\,s^{-1}}$)	5.60	5.48
CFH		
Liftoff time	09:14:31	09:36:21
Unwinder length	60 m	60 m
Burst altitude (km)	32.123	34.615
Ascent rate ($\mathrm{m\,s^{-1}}$)	5.05	5.23

Appendix B

Pressure Chamber

This pressure chamber was specifically designed for the characterization of the QCLAS instrument. The chamber is based on a cylindrical body out of PMMA with 370 mm inner diameter and wall strength 15 mm, containing a gas volume of 60 l. The front and the rear face is made of a 15 mm PMMA plate, containing feedthroughs for sensors, power, and cooling water. These plates further contain gas inlets and outlets. Using membrane pumps, the chamber can be evacuated to < 5 hPa. An internal rack holds the cold plate system and allows the centered placement of the instrument. The cold plate system comprises six high-power TECs mounted on a water-cooled heat exchange plate that withdraws the excess heat. The cold side of these TECs is enlarged by connection to aluminum plates with enlarged surface area. The cold plate temperature is stabilized by a feedback-driven controller (Meerstetter, Switzerland). Fig. B.1 shows the entire system.

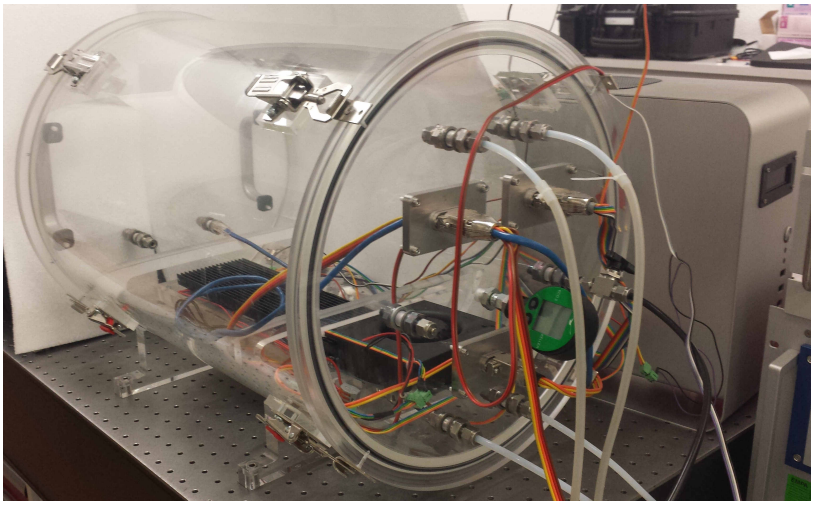

Figure B.1: In-house developed chamber to simulate stratospheric pressure conditions. Furthermore, it was used for characterization experiments of the QCLAS in various configurations.

Bibliography

D. W. Allan. Statistics of Atomic Frequency Standards. *Proc. IEEE*, 54(2):221–230, 1966. ISSN 15582256. DOI: 10.1109/PROC.1966.4634.

J. G. Anderson, D. M. Wilmouth, J. B. Smith, and D. S. Sayres. UV Dosage Levels in Summer: Increased Risk of Ozone Loss from Convectively Injected Water Vapor. *Science*, 337:835–839, 2012. ISSN 0036-8075. DOI: 10.1126/science.1222978.

A. Banerjee, G. Chiodo, M. Previdi, M. Ponater, A. J. Conley, and L. M. Polvani. Stratospheric water vapor: an important climate feedback. *Clim. Dyn.*, 53(3-4):1697–1710, 2019. ISSN 14320894. DOI: 10.1007/s00382-019-04721-4. URL http://dx.doi.org/10.1007/s00382-019-04721-4.

P. R. Berman. Speed-dependent collisional width and shift parameters in spectral profiles. *J. Quant. Spectrosc. Radiat. Transf.*, 12(9):1331–1342, 1972. ISSN 00224073. DOI: 10.1016/0022-4073(72)90189-6.

BIPM. Evaluation of measurement data — Guide to the expression of uncertainty in measurement. *Int. Organ. Stand. Geneva ISBN*, 50(September):134, 2008. ISSN 00099147. DOI: 10.1373/clinchem.2003.030528. URL http://www.bipm.org/en/publications/guides/gum.html.

A. W. Brewer. Evidence for a World Circulation Provided by the Measurement of Helium and Water Vapour Distribution in the Stratosphere. *Q. J. R. Meteorol. Soc.*, 75(326):351, 1949. ISSN 1477870X. DOI: 10.1002/qj.49707532603.

S. Brunamonti, T. Jorge, P. Oelsner, S. Hanumanthu, B. B. Singh, K. Ravi Kumar, S. Sonbawne, S. Meier, D. Singh, F. G. Wienhold, B. Ping Luo, M. Boettcher, Y. Poltera, H. Jauhiainen, R. Kayastha, J. Karmacharya, R. DIrksen, M. Naja, M. Rex, S. Fadnavis, and T. Peter. Balloon-borne measurements of temperature, water vapor, ozone and aerosol backscatter on the southern slopes of the Himalayas during StratoClim 2016-2017. *Atmos. Chem. Phys.*, 18(21):15937–15957, 2018. ISSN 16807324. DOI: 10.5194/acp-18-15937-2018.

B. Buchholz and V. Ebert. Absolute, pressure-dependent validation of a calibration-free, airborne laser hygrometer transfer standard (SEALDH-II) from 5 to 1200 ppmv using a metrological humidity generator. *Atmos. Meas. Tech.*, 11(1):459–471, 2018. ISSN 18678548. DOI: 10.5194/amt-11-459-2018.

B. Buchholz, A. Afchine, A. Klein, C. Schiller, M. Krämer, and V. Ebert. HAI, a new airborne, absolute, twin dual-channel, multi-phase TDLAS-hygrometer: Background, design, setup, and first flight data. *Atmos. Meas. Tech.*, 10(1):35–57, 2017. ISSN 18678548. DOI: 10.5194/amt-10-35-2017.

A. L. Buck. New equations for computing vapour pressure and enhancement factor. 20(12): 1527–1532, 1981. ISSN 08948763.

R. Busen and A. Buck. A High-Performance Hygrometer for Aircraft Use: Description, Installation, and Flight Data. 12:73–84, 1995.

S. Chandrasekhar. *Radiative Transfer*. Dover Books on Physics. Dover Publications, 1960.

R. F. Curl, F. Capasso, C. Gmachl, A. A. Kosterev, B. McManus, R. Lewicki, M. Pusharsky, G. Wysocki, and F. K. Tittel. Quantum cascade lasers in chemical physics. *Chem. Phys. Lett.*, 487(1-3):1–18, 2010. ISSN 00092614. DOI: 10.1016/j.cplett.2009.12.073. URL http://dx.doi.org/10.1016/j.cplett.2009.12.073.

A. E. Dessler and S. C. Sherwood. Atmospheric science: A matter of humidity. *Science*, 323(5917):1020–1021, 2009. ISSN 00368075. DOI: 10.1126/science.1171264.

A. E. Dessler, M. R. Schoeberl, T. Wang, S. M. Davis, and K. H. Rosenlof. Stratospheric water vapor feedback. *Proc. Natl. Acad. Sci. U. S. A.*, 110(45), 2013. ISSN 1091-6490. DOI: 10.1073/pnas.1310344110.

A. E. Dessler, M. R. Schoeberl, T. Wang, S. M. Davis, K. H. Rosenlof, and J. Vernier. Variations of stratospheric water vapo over the past three decades. *J. Geophys. Res.*, 119 (12):588–598, 2014. DOI: 10.1002/2014JD021712.

R. H. Dicke. The Effect of Collisions upon the Doppler Width of Spectral Lines. *Phys. Rev.*, 89(2):472, 1953.

R. J. Dirksen, G. E. Bodeker, P. W. Thorne, A. Merlone, T. Reale, J. Wang, D. F. Hurst, B. B. Demoz, T. D. Gardiner, B. Ingleby, M. Sommer, C. von Rohden, and T. Leblanc. Progress in managing the transition from the rs92 to the vaisala rs41 as the operational radiosonde within the gcos reference upper-air network. *Geoscientific Instrumentation, Methods and Data Systems Discussions*, 2019:1–40, 2019. DOI: 10.5194/gi-2019-36. URL https://www.geosci-instrum-method-data-syst-discuss.net/gi-2019-36/.

G. S. Diskin, J. R. Podolske, G. W. Sachse, and T. A. Slate. Open-path airborne tunable diode laser hygrometer. *Int. Symp. Opt. Sci. Technol.*, 4817:196–204, 2002. ISSN 0277786X. DOI: 10.1117/12.453736. URL http://proceedings.spiedigitallibrary.org/proceeding.aspx?articleid=1314316.

G. Durry and G. Megie. In Situ Measurements of H2O From a Stratospheric Balloon by Diode Laser Direct-Differential Absorption Spectroscopy at 1.39 μm. *Appl. Opt.*, 39(30): 5601, 2000. DOI: 10.1364/AO.39.005601.

G. Durry, N. Amarouche, L. Joly, X. Liu, B. Parvitte, and V. Zeninari. Laser diode spectroscopy of H2O at 2.63 um for atmospheric applications. *Appl. Phys. B Lasers Opt.*, 90 (3-4):573–580, 2008. ISSN 09462171. DOI: 10.1007/s00340-007-2884-3.

D. W. Fahey, R. S. Gao, O. Möhler, H. Saathoff, C. Schiller, V. Ebert, M. Krämer, T. Peter, N. Amarouche, L. M. Avallone, R. Bauer, Z. Bozóki, L. E. Christensen, S. M. Davis, G. Durry, C. Dyroff, R. L. Herman, S. Hunsmann, S. M. Khaykin, P. Mackrodt, J. Meyer, J. B. Smith, N. Spelten, R. F. Troy, H. Vömel, S. Wagner, and F. G. Wienhold. The AquaVIT-1 intercomparison of atmospheric water vapor measurement techniques. *Atmos. Meas. Tech.*, 7(9):3177–3213, 2014. ISSN 18678548. DOI: 10.5194/amt-7-3177-2014.

J. Faist. *Quantum cascade lasers*. 2012. ISBN 978-0-7503-0726-0. DOI: 10.1201/9781420056990.ch12. URL http://dx.doi.org/10.1201/9781420056990.ch12.

M. Fischer, B. Tuzson, A. Hugi, R. Brönnimann, A. Kunz, S. Blaser, M. Rochat, O. Landry, A. Müller, and L. Emmenegger. Intermittent operation of QC-lasers for mid-IR spectroscopy with low heat dissipation: tuning characteristics and driving electronics. *Opt. Express*, 22(6):7014–7027, 2014. ISSN 1094-4087. DOI: 10.1364/OE.22.007014.

P. M. D. E. Forster and K. P. Shine. Radiative forcing and temperature trends from stratospheric ozone changes. *J. Geophys. Res. Lett.*, 102(D9):10841–10855, 1997.

A. G. Fox and T. Li. Resonant Modes in a Maser Interferometer. *Bell Syst. Tech. J.*, 40 (2):453 – 488, 1961. ISSN 00058580. DOI: 10.1002/j.1538-7305.1961.tb01625.x.

S. Fueglistaler and P. H. Haynes. Control of interannual and longer-term variability of stratospheric water vapor. *J. Geophys. Res. Atmos.*, 110(24):1–14, 2005. ISSN 01480227. DOI: 10.1029/2005JD006019.

S. Fueglistaler, A. E. Dessler, T. J. Dunkerton, I. Folkins, Q. Fu, and P. W. Mote. Tropical tropopause layer. *Reviews of Geophysics*, 47(1), 2009. DOI: 10.1029/2008RG000267. URL https://agupubs.onlinelibrary.wiley.com/doi/abs/10.1029/2008RG000267.

S. Fueglistaler, Y. S. Liu, T. J. Flannaghan, P. H. Haynes, D. P. Dee, W. J. Read, E. E. Remsberg, L. W. Thomason, D. F. Hurst, J. R. Lanzante, and P. F. Bernath. The relation between atmospheric humidity and temperature trends for stratospheric water. *J. Geophys. Res. Atmos.*, 118(2):1052–1074, 2013. ISSN 21698996. DOI: 10.1002/jgrd.50157.

L. Galatry. Simultaneous effect of doppler and foreign gas broadening on spectral lines. *Phys. Rev.*, 122(4):1218–1223, 1961. ISSN 0031899X. DOI: 10.1103/PhysRev.122.1218.

A. Gettelman and S. C. Sherwood. Processes Responsible for Cloud Feedback. *Curr. Clim. Chang. Reports*, 2(4):179–189, 2016. ISSN 21986061. DOI: 10.1007/s40641-016-0052-8. URL http://dx.doi.org/10.1007/s40641-016-0052-8.

R. Ghorbani and F. M. Schmidt. Real-time breath gas analysis of CO and CO2 using an EC-QCL. *Appl. Phys. B Lasers Opt.*, 123(5):144, 2017. ISSN 09462171. DOI: 10.1007/s00340-017-6715-x.

I. Gordon, L. Rothman, C. Hill, R. Kochanov, Y. Tan, P. Bernath, M. Birk, V. Boudon, A. Campargue, K. Chance, B. Drouin, J.-M. Flaud, R. Gamache, J. Hodges, D. Jacquemart, V. Perevalov, A. Perrin, K. Shine, M. Smith, J. Tennyson, G. Toon, H. Tran, V. Tyuterev, A. Barbe, A. Császár, V. Devi, T. Furtenbacher, J. Harrison, J.-M. Hartmann, A. Jolly, T. Johnson, T. Karman, I. Kleiner, A. Kyuberis, J. Loos, O. Lyulin, S. Massie, S. Mikhailenko, N. Moazzen-Ahmadi, H. Müller, O. Naumenko, A. Nikitin,

O. Polyansky, M. Rey, M. Rotger, S. Sharpe, K. Sung, E. Starikova, S. Tashkun, J. V. Auwera, G. Wagner, J. Wilzewski, P. Wcisło, S. Yu, and E. Zak. The HITRAN2016 molecular spectroscopic database. *J. Quant. Spectrosc. Radiat. Transf.*, 203:3–69, 2017. ISSN 00224073. DOI: 10.1016/j.jqsrt.2017.06.038.

M. Graf, H. Looser, L. Emmenegger, and B. Tuzson. Beam folding analysis and optimization of mask-enhanced toroidal multipass cells. *Opt. Lett.*, 42(16):3137–3140, 2017. DOI: 10.1364/OL.42.003137. URL http://ol.osa.org/abstract.cfm?URI=ol-42-16-3137.

M. Graf, L. Emmenegger, and B. Tuzson. Compact, circular, and optically stable multipass cell for mobile laser absorption spectroscopy. *Opt. Lett.*, 43(11):2434–2437, 2018. ISSN 15394794. DOI: 10.1364/OL.43.002434. URL http://ol.osa.org/abstract.cfm?URI=ol-43-11-2434.

M. Graf, P. Scheidegger, A. Kupferschmid, H. Looser, T. Peter, R. Dirksen, L. Emmenegger, and B. Tuzson. Miniaturized Mid-IR Laser Spectrometer for Balloon-borne Water Vapor Measurements in the UTLS. *Atmos. Meas. Tech.*, submitted, 2020.

W. Gurlit, R. Zimmermann, C. Giesemann, T. Fernholz, V. Ebert, J. Wolfrum, U. Platt, and J. P. Burrows. Lightweight diode laser spectrometer CHILD (Compact High-altitude In-situ Laser Diode) for balloonborne measurements of water vapor and methane. *Appl. Opt.*, 44(1):91–102, 2005. ISSN 0003-6935. DOI: 10.1364/AO.44.000091. URL http://www.ncbi.nlm.nih.gov/pubmed/15662890http://www.scopus.com/inward/record.url?eid=2-s2.0-12144281285{&}partnerID=tZOtx3y1.

H. P. Haerri, T. Macé, J. Waldén, C. Pascale, B. Niederhauser, K. Wirtz, V. Stovcik, C. Sutour, J. Couette, and T. Waldén. Dilution and permeation standards for the generation of NO, NO2 and SO2 calibration gas mixtures. *Meas. Sci. Technol.*, 28(3), 2017. ISSN 13616501. DOI: 10.1088/1361-6501/aa543d.

E. G. Hall, A. F. Jordan, D. F. Hurst, S. J. Oltmans, H. Vömel, B. Kühnreich, and V. Ebert. Advancements, measurement uncertainties, and recent comparisons of the NOAA frost point hygrometer. *Atmos. Meas. Tech.*, 9(9):4295–4310, 2016. ISSN 18678548. DOI: 10.5194/amt-9-4295-2016.

T. F. Hanisco, E. J. Lanzendorf, P. O. Wennberg, K. K. Perkins, R. M. Stimpfle, P. B. Voss, J. G. Anderson, R. C. Cohen, D. W. Fahey, R. S. Gao, E. J. Hintsa, R. J. Salawitch, J. J. Margitan, C. T. McElroy, and C. Midwinter. Sources, sinks, and the distribution of OH in the lower stratosphere. *J. Phys. Chem. A*, 105(9):1543–1553, 2001. ISSN 10895639. DOI: 10.1021/jp002334g.

J. E. Harries. Atmospheric radiation and atmospheric humidity. *Q. J. R. Meteorol. Soc. Part B*, 123(544):2173–2186, 1997. ISSN 00359009.

I. M. Held and B. J. Soden. Water Vapor Feedback And Global Warming. *Annu. Rev. Energy Env.*, 25:441, 2000.

D. Herriott, H. Kogelnik, and R. Kompfner. Off-Axis Paths in Spherical Mirror Interferometers. *Appl. Opt.*, 3(4):523, 1964. ISSN 0003-6935. DOI: 10.1364/AO.3.000523.

HITRAN. HITRAN Definitions, 2020. URL https://hitran.org/docs/definitions-and-units/.

J. R. Holton, P. H. Haynes, M. E. Mcintyre, A. R. Douglass, B. Rood, and L. Pfister. STRATOSPHERE-TROPOSPHERE EXCHANGE. (95):403–439, 1995.

J. Humlíček. Optimized computation of the voigt and complex probability functions. *J. Quant. Spectrosc. Radiat. Transf.*, 27(4):437–444, 1982. ISSN 00224073. DOI: 10.1016/0022-4073(82)90078-4.

P. M. Hundt, M. Müller, M. Mangold, B. Tuzson, P. Scheidegger, H. Looser, C. Hüglin, and L. Emmenegger. Mid-IR spectrometer for mobile, real-time urban NO_2 measurements. *Atmos. Meas. Tech.*, 11(5):2669–2681, 2018. DOI: 10.5194/amt-11-2669-2018. URL https://www.atmos-meas-tech.net/11/2669/2018/.

D. F. Hurst, S. J. Oltmans, H. Vömel, K. H. Rosenlof, S. M. Davis, E. A. Ray, E. G. Hall, and A. F. Jordan. Stratospheric water vapor trends over Boulder, Colorado: Analysis of the 30 year Boulder record. *J. Geophys. Res. Atmos.*, 116(2):1–12, 2011. ISSN 01480227. DOI: 10.1029/2010JD015065.

ISO-5725. Accuracy (trueness and precision) of measurement methods and results, 1994.

E. J. Jensen, J. B. Smith, L. Pfister, J. V. Pittman, E. M. Weinstock, D. S. Sayres, R. L. Herman, R. F. Troy, K. H. Rosenlof, T. L. Thompson, A. M. Fridlind, P. K. Hudson, D. J. Cziczo, A. J. Heymsfield, C. Schmitt, and J. C. Wilson. Ice supersaturations exceeding 100% at the cold tropical tropopause: implications for cirrus formation and dehydration. *Atmos. Meas. Tech.*, 5:851–862, 2005.

T. Jorge. *Developments in balloon-borne water vapour measurements with frost point hygrometers*. PhD thesis, ETH Zurich, Zurich, 2019.

N. Kämpfer. *Monitoring Atmospheric Water Vapour*. Springer, 2013. ISBN 9781461460992.

D. B. Kirk-Davidoff, E. J. Hintsa, J. G. Anderson, and D. W. Keith. The effect of climate change on ozone depletion through changes in stratospheric water vapour. *Nature*, 402 (6760):399–401, 1999. ISSN 00280836. DOI: 10.1038/46521.

D. Kley, J. M. Russell, C. Phillips, E. Remsberg, C. Schiller, J. Bates, R. Bevilacqua, E. Browell, E. Chiou, W. Chu, G. Ehret, D. Feist, D. Seidel, L. Gordley, M. Gunson, P. Hartogh, M. Helten, R. Herman, E. Hintsa, F. Irion, S. Ismail, D. Johnson, and D. Whiteman. *SPARC Assessment of Upper Tropospheric and Stratospheric Water Vapour*. 2000.

F. K. Kneubühl and M. W. Sigrist. *Laser*. Teubner Studienbücher Physik. Vieweg+Teubner Verlag, 2013. ISBN 9783322938756.

M. Krämer, C. Schiller, A. Afchine, R. Bauer, I. Gensch, A. Mangold, S. Schlicht, N. Spelten, N. Sitnikov, S. Borrmann, M. De Reus, and P. Spichtinger. Ice supersaturations and cirrus cloud crystal numbers. *Atmos. Chem. Phys.*, 9(11):3505–3522, 2009. ISSN 16807324. DOI: 10.5194/acp-9-3505-2009.

A. Kräuchi. *New in-situ upper-air technology and measurements using a return glider radiosonde*. PhD thesis, ETH Zürich, 2016.

T. Li, H. Kogelnik, and T. Li. Laser Beams and Resonators.pdf. *Appl. Opt.*, 5(10):1312–1329, 1966. ISSN 15582256. DOI: 10.1109/PROC.1966.5119.

D. Lisak, A. Cygan, D. Bermejo, J. L. Domenech, J. T. Hodges, and H. Tran. Application of the Hartmann-Tran profile to analysis of H2O spectra. *J. Quant. Spectrosc. Radiat. Transf.*, 164:221–230, 2015. ISSN 00224073. DOI: 10.1016/j.jqsrt.2015.06.012. URL http://dx.doi.org/10.1016/j.jqsrt.2015.06.012.

C. Liu, B. Tuzson, P. Scheidegger, H. Looser, B. Bereiter, M. Graf, M. Hundt, O. Aseev, D. Maas, and L. Emmenegger. Laser driving and data processing concept for mobile trace gas sensing: Design and implementation. *Rev. Sci. Instrum.*, 89(6), 2018. ISSN 10897623. DOI: 10.1063/1.5026546. URL http://dx.doi.org/10.1063/1.5026546.

A. Lorek. Humidity measurement with capacitive humidity sensors between -70°C and 25°C in low vacuum. *J. Sensors Sens. Syst.*, 3(2):177–185, 2014. ISSN 2194878X. DOI: 10.5194/jsss-3-177-2014.

A. Lykov, V. Yushkov, S. Khaykin, V. Astakhov, and V. Budovich. New version of balloon hygrometer for in situ water vapour measurements in the upper troposphere and lower stratopshere (FLASH-BM). *Eur. Sp. Agency, (Special Publ. ESA SP)*, 700 SP:341–345, 2011. ISSN 03796566.

S. Manabe and R. T. Wetherald. Thermal Equilibrium of the Atmosphere with a Given Distribution of Relative Humidity. *J. Atmos. Sci.*, 24(3), 1967.

M. Mangold, B. Tuzson, M. Hundt, J. Jágerská, H. Looser, and L. Emmenegger. Circular paraboloid reflection cell for laser spectroscopic trace gas analysis. *J. Opt. Soc. Am. A*, 33(5):913–919, 2016. ISSN 1084-7529. DOI: 10.1364/JOSAA.33.000913.

H. J. Mastenbrook and S. J. Oltmans. Stratospheric water vapor variability for washington, dc/boulder, co: 1964–82. *Journal of the Atmospheric Sciences*, 40(9):2157–2165, 1983. DOI: 10.1175/1520-0469(1983)040<2157:SWVVFW>2.0.CO;2.

R. D. May. Open-path, near-infrared tunable diode laser spectrometer for atmospheric measurements of H2O. *J. Geophys. Res. Atmos.*, 103(D15):19161–19172, 1998. ISSN 01480227. DOI: 10.1029/98JD01678.

J. B. McManus. Application of quantum cascade lasers to high-precision atmospheric trace gas measurements. *Opt. Eng.*, 49(11):111124, 2010. ISSN 0091-3286. DOI: 10.1117/1.3498782. URL http://opticalengineering.spiedigitallibrary.org/article.aspx?doi=10.1117/1.3498782.

J. B. McManus and P. L. Kebabian. Narrow optical interference fringes for certain setup conditions in multipass absorption cells of the Herriott type. *Appl. Opt.*, 29(7):898–900, 1990. ISSN 0003-6935. DOI: 10.1364/AO.29.000898.

J. B. McManus, P. L. Kebabian, and M. S. Zahniser. Cells for Long-Path-Length Spectroscopy. *Appl. Opt.*, 34(18), 1995.

J. B. McManus, M. S. Zahniser, and D. D. Nelson. Dual quantum cascade laser trace gas instrument with astigmatic Herriott cell at high pass number. *Appl. Opt.*, 50(4):A74, 2011. ISSN 0003-6935. DOI: 10.1364/AO.50.000A74.

J. Meyer, C. Rolf, C. Schiller, S. Rohs, N. Spelten, A. Afchine, M. Zöger, N. Sitnikov, T. D. Thornberry, A. W. Rollins, Z. Bozóki, D. Tátrai, V. Ebert, B. Kühnreich, P. Mackrodt, O. Möhler, H. Saathoff, K. H. Rosenlof, and M. Krämer. Two decades of water vapor measurements with the FISH fluorescence hygrometer: A review. *Atmos. Chem. Phys.*, 15(14):8521–8538, 2015. ISSN 16807324. DOI: 10.5194/acp-15-8521-2015.

G. Moreau, C. Robert, V. Catoire, M. Chartier, C. Camy-peyret, N. Huret, M. Pirre, L. Pomathiod, and G. Chalumeau. SPIRALE : a multispecies in situ balloonborne instrument with six tunable diode laser spectrometers. *Appl. Opt.*, 44(28), 2005.

P. W. Mote, K. H. Rosenlof, E. Mcintyre, E. S. Carr, J. C. Gille, R. Holton, S. Kinnersley, H. C. Pumphrey, M. Russell, and J. W. Wal. An atmospheric tape recorder: The imprint of tropical tropopause temperatures on stratospheric water vapor. *J. Geophys. Res.*, 101 (D2):3989–4006, 1996. ISSN 0148-0227. DOI: 10.1029/95JD03422.

R. Müller, A. Kunz, D. F. Hurst, C. Rolf, M. Krämer, and M. Riese. The need for accurate long-term measurements of water vapor in the upper troposphere and lower stratosphere with global coverage. *Earth's Future*, 4:25–32, 2016. ISSN 23284277. DOI: 10.1002/2015EF000321.

D. M. Murphy and T. Koop. Review of the vapour pressures of ice and supercooled water for atmospheric applications. *Q. J. R. Meteorol. Soc.*, 131(608):1539–1565, 2005. ISSN 00359009. DOI: 10.1256/qj.04.94.

M. Nazarathy and J. Shamir. First-order optics—a canonical operator representation: lossless systems. *J. Opt. Soc. Am.*, 72(3):356, 1982. ISSN 0030-3941. DOI: 10.1364/JOSA.72.000356.

G. E. Nedoluha, R. M. Bevilacqua, R. M. Gomez, B. C. Hicks, J. M. Russell, and B. J. Connor. An evaluation of trends in middle atmospheric water vapor as measured by HALOE, WVMS, and POAM. *J. Geophys. Res. Atmos.*, 108(D13):4391, 2003. DOI: 10.1029/2002jd003332.

N. H. Ngo, D. Lisak, H. Tran, and J. M. Hartmann. An isolated line-shape model to go beyond the Voigt profile in spectroscopic databases and radiative transfer codes. *J. Quant. Spectrosc. Radiat. Transf.*, 129:89–100, 2013. ISSN 00224073. DOI: 10.1016/j.jqsrt.2013.05.034. URL http://dx.doi.org/10.1016/j.jqsrt.2013.05.034.

S. J. Oltmans and D. J. Hofmann. Increase in lower-stratospheric water vapour at a mid-latitude Northern Hemisphere site from 1981 to 1994. *Nature*, 374:146–149, 1995. ISSN 0028-0836. DOI: 10.1038/374146a0. URL http://www.nature.com/nature/journal/v374/n6518/abs/374146a0.html.

M. E. Paige. Compact and low-power diode laser hygrometer for weather balloons. *J. Atmos. Ocean. Technol.*, 22(8):1219–1224, 2005. ISSN 07390572. DOI: 10.1175/JTECH1770.1.

T. Peter, C. Marcolli, P. Spichtinger, T. Corti, M. B. Baker, and T. Koop. Atmosphere. When dry air is too humid. *Science*, 314(5804):1399–402, 2006. ISSN 1095-9203. DOI: 10.1126/science.1135199.

S. G. Rautian and I. I. Sobel'man. The effect of collisions on the doppler broadening of spectral lines. *Sov. Phys. Uspekhi*, 9(5), 1967.

L. E. Revell, A. Stenke, E. Rozanov, W. Ball, S. Lossow, and T. Peter. The role of methane in projections of 21st century stratospheric water vapour. *Atmos. Chem. Phys.*, 16(20): 13067–13080, 2016. ISSN 16807324. DOI: 10.5194/acp-16-13067-2016.

D. Richter, P. Weibring, J. G. Walega, A. Fried, S. M. Spuler, and M. S. Taubman. Compact highly sensitive multi-species airborne mid-IR spectrometer. *Applied Physics B*, 119(1): 119–131, 2015. ISSN 0946-2171. DOI: 10.1007/s00340-015-6038-8. URL http://link.springer.com/10.1007/s00340-015-6038-8.

A. W. Rollins, T. D. Thornberry, R. S. Gao, J. B. Smith, D. S. Sayres, M. R. Sargent, C. Schiller, M. Krämer, N. Spelten, D. F. Hurst, A. F. Jordan, E. G. Hall, H. Vömel, G. S. Diskin, J. R. Podolske, L. E. Christensen, K. H. Rosenlof, E. J. Jensen, and D. W. Fahey. Evaluation of UT/LS hygrometer accuracy by intercomparison during the NASA MACPEX mission. *J. Geophys. Res. Atmos.*, 119(4):1915–1935, 2014. ISSN 2169897X. DOI: 10.1002/2013JD020817.

H. Rosenlof and D. Kley. Stratospheric water vapor increases over the past half-century. *Geophys. Res. Lett.*, 28(7):1195–1198, 2001.

K. H. Rosenlof. *Stratospheric Chemistry Topics: Stratospheric Water Vapor*, volume 5. Elsevier, 2015. ISBN 9780123822260. DOI: 10.1016/B978-0-12-382225-3.00393-5. URL http://dx.doi.org/10.1016/B978-0-12-382225-3.00393-5.

L. S. Rothman, I. E. Gordon, Y. Babikov, A. Barbe, D. C. Benner, P. Bernath, M. Birk, L. Bizzocchi, V. Boudon, L. R. Brown, A. Campargue, K. Chance, E. Cohen, L. Coudert, V. Devi, B. Drouin, A. Fayt, J.-M. Flaud, R. Gamache, J. Harrison, J.-M. Hartmann, C. Hill, J. Hodges, D. Jacquemart, A. Jolly, J. Lamouroux, R. L. Roy, G. Li, D. Long, O. Lyulin, C. Mackie, S. Massie, S. Mikhailenko, H. Müller, O. Naumenko, A. Nikitin, J. Orphal, V. Perevalov, A. Perrin, E. Polovtseva, C. Richard, M. Smith, E. Starikova, K. Sung, S. Tashkun, J. Tennyson, G. Toon, V. Tyuterev, and G. Wagner. The hitran2012 molecular spectroscopic database. *Journal of Quantitative Spectroscopy and Radiative Transfer*, 130:4 – 50, 2013. ISSN 0022-4073. DOI: https://doi.org/10.1016/j.jqsrt.2013.07.002. URL http://www.sciencedirect.com/science/article/pii/S0022407313002859. HITRAN2012 special issue.

M. R. Sargent, D. S. Sayres, J. B. Smith, M. Witinski, N. T. Allen, J. N. Demusz, M. Rivero, C. Tuozzolo, and J. G. Anderson. A new direct absorption tunable diode laser spectrometer for high precision measurement of water vapor in the upper troposphere and lower stratosphere. *Rev. Sci. Instrum.*, 84(7):074102, 2013. ISSN 1089-7623. DOI: 10.1063/1.4815828. URL http://www.ncbi.nlm.nih.gov/pubmed/23902086.

G. A. Schmidt, R. A. Ruedy, R. L. Miller, and A. A. Lacis. Attribution of the present-day total greenhouse effect. *J. Geophys. Res. Atmos.*, 115(20):1–6, 2010. ISSN 01480227. DOI: 10.1029/2010JD014287.

SciPyCommunity. SciPy Reference. URL https://docs.scipy.org/doc/scipy/reference/index.html. accessed: Feb. 2020.

D. J. Seidel, R. J. Ross, J. K. Angell, and G. C. Reid. Climatological characteristics of the tropical tropopause as revealed by radiosondes. *J. Geophys. Res. Atmos.*, 106(D8): 7857–7878, 2001. ISSN 01480227. DOI: 10.1029/2000JD900837.

A. E. Siegman. Unstable optical resonators. *Appl. Opt.*, 13(2):353–67, 1974. ISSN 0003-6935. DOI: 10.1364/AO.13.000353. URL http://www.ncbi.nlm.nih.gov/pubmed/20125987.

A. E. Siegman. *Lasers*. University Science Books, 1986. ISBN 9780935702118.

J. A. Silver. Simple dense-pattern optical multipass cells. *Appl. Opt.*, 44(31):6545–6556, 2005. ISSN 0003-6935. DOI: 10.1364/AO.44.006545.

J. A. Silver and D. C. Hovde. Near-infrared diode laser airborne hygrometer. *Rev. Sci. Instrum.*, 65(5):1691, 1994. ISSN 00346748. DOI: 10.1063/1.1144861.

J. B. Smith. Chemistry of the Atmosphere, Observations for Chemistry (In Situ): Water Vapor Sondes, 2015.

B. J. Soden. The Radiative Signature of Upper Tropospheric Moistening. *Science*, 310:841, 2005. ISSN 0036-8075. DOI: 10.1126/science.1115602.

S. Solomon, K. H. Rosenlof, R. W. Portmann, J. S. Daniel, S. M. Davis, T. J. Sanford, and G.-K. Plattner. Contributions of stratospheric water vapor to decadal changes in the rate of global warming. *Science*, 327(5970):1219–23, 2010. ISSN 1095-9203. DOI: 10.1126/science.1182488.

D. M. Sonnenfroh, W. J. Kessler, J. C. Magill, B. L. Upschulte, M. G. Allen, and J. D. W. Barrick. In-situ sensing of tropospheric water vapor using an airborne near-IR diode laser hygrometer. *Appl. Phys. B Lasers Opt.*, 67(3):275–282, 1998. ISSN 09462171.

STEMLab. Red Pitaya Specifications, 2020. URL https://www.redpitaya.com/f145/specifications.

T. Sugidachi. New Peltier-based chilled-mirror hygrometer "SKYDEW", 2018. GRUAN ICM-10 Meeting.

M. L. Thoma, R. Kaschow, and F. J. Hindelang. A multiple-reflection cell suited for absorption measurements in shock tubes. *Shock Waves*, 4(1):51–53, 1994. ISSN 09381287. DOI: 10.1007/BF01414633.

T. D. Thornberry, A. W. Rollins, R. S. Gao, L. A. Watts, S. J. Ciciora, R. J. McLaughlin, and D. W. Fahey. A two-channel, tunable diode laser-based hygrometer for measurement of water vapor and cirrus cloud ice water content in the upper troposphere and lower stratosphere. *Atmospheric Measurement Techniques*, 8(1):211–224, 2015. DOI: 10.5194/amt-8-211-2015. URL https://www.atmos-meas-tech.net/8/211/2015/.

B. Tuzson, M. Mangold, H. Looser, A. Manninen, and L. Emmenegger. Compact multipass optical cell for laser spectroscopy. *Opt. Lett.*, 38(3):257–9, 2013. ISSN 1539-4794. DOI: 10.1364/OL.38.000257. URL http://www.ncbi.nlm.nih.gov/pubmed/23381403.

B. Tuzson, J. Jágerská, H. Looser, M. Graf, F. Felder, M. Fill, L. Tappy, and L. Emmenegger. Highly Selective Volatile Organic Compounds Breath Analysis Using a Broadly-Tunable Vertical-External-Cavity Surface-Emitting Laser. *Anal. Chem.*, 89(12):6377–6383, 2017. ISSN 15206882. DOI: 10.1021/acs.analchem.6b04511.

B. Tuzson, M. Graf, J. Ravelid, P. Scheidegger, A. Kupferschmid, H. Looser, R. P. Morales, and L. Emmenegger. A compact qcl spectrometer for mobile, high-precision methane sensing aboard drones. *Atmospheric Measurement Techniques Discussions*, 2020:1–16, 2020. DOI: 10.5194/amt-2020-102. URL https://www.atmos-meas-tech-discuss.net/amt-2020-102/.

UNEP. Montreal Protocol – Kigali Amendment, 2016.

Vaisala. RS41 Specifications, 2020. URL https://www.vaisala.com/sites/default/files/documents/RS41-SG-Datasheet-B211321EN.pdf. accessed: Feb. 2020.

T. Villa, F. Gonzalez, B. Miljievic, Z. Ristovski, and L. Morawska. An Overview of Small Unmanned Aerial Vehicles for Air Quality Measurements: Present Applications and Future Prospectives. *Sensors*, 16(7):1072, 2016. ISSN 1424-8220. DOI: 10.3390/s16071072. URL http://www.mdpi.com/1424-8220/16/7/1072.

VLK Art. 16. Verordnung des UVEK über Luftfahrzeuge besonderer Kategorien, 1994.

H. Vömel, D. E. David, and K. Smith. Accuracy of tropospheric and stratospheric water vapor measurements by the cryogenic frost point hygrometer: Instrumental details and observations. *J. Geophys. Res. Atmos.*, 112(8):1–14, 2007. ISSN 01480227. DOI: 10.1029/2006JD007224.

H. Vömel, T. Naebert, R. Dirksen, and M. Sommer. An update on the uncertainties of water vapor measurements using cryogenic frost point hygrometers. *Atmos. Meas. Tech.*, 9(8):3755–3768, 2016. DOI: 10.5194/amt-9-3755-2016. URL https://www.atmos-meas-tech.net/9/3755/2016/.

C. R. Webster and P. R. Mahaffy. Determining the local abundance of Martian methane and its' 13C/12C and D/H isotopic ratios for comparison with related gas and soil analysis on the 2011 Mars Science Laboratory (MSL) mission. *Planetary and Space Science*, 59(2-3):271–283, 2011. ISSN 00320633. DOI: 10.1016/j.pss.2010.08.021. URL http://linkinghub.elsevier.com/retrieve/pii/S003206331000259X.

E. M. Weinstock, J. B. Smith, D. S. Sayres, J. V. Pittman, J. R. Spackman, E. J. Hintsa, T. F. Hanisco, E. J. Moyer, J. M. St. Clair, M. R. Sargent, and J. G. Anderson. Validation of the Harvard Lyman-a in situ water vapor instrument: Implications for the mechanisms that control stratospheric water vapor. *J. Geophys. Res. Atmos.*, 114(23):1–24, 2009. ISSN 01480227. DOI: 10.1029/2009JD012427.

G. Weissler and R. Carlson. *Vacuum Physics and Technology*. ISSN. Elsevier Science, 1980. ISBN 9780080859958.

J. Wendell and A. Jordan. iMet-1-RSB Radiosonde XDATA Protocol and Daisy Chaining, 2016. URL ftp://aftp.cmdl.noaa.gov/user/jordan/iMet-1-RSB%20Radiosonde%20XDATA%20Daisy%20Chaining.pdf. accessed: Feb. 2020.

P. O. Werle, R. Mücke, and F. Slemr. The limits of signal averaging in atmospheric trace-gas monitoring by tunable diode-laser absorption spectroscopy (tdlas). *Applied Physics B*, 57(2):131–139, 1993.

D. N. Whiteman, K. C. Vermeesch, L. D. Oman, and E. C. Weatherhead. The relative importance of random error and observation frequency in detecting trends in upper tropospheric water vapor. *J. Geophys. Res. Atmos.*, 116(21):1–7, 2011. ISSN 01480227. DOI: 10.1029/2011JD016610.

M. A. Zondlo, M. E. Paige, S. M. Massick, and J. A. Silver. Vertical cavity laser hygrometer for the National Science Foundation Gulfstream-V aircraft. *J. Geophys. Res. Atmos.*, 115 (20):1–14, 2010. ISSN 01480227. DOI: 10.1029/2010JD014445.

Acknowledgments

I would like to express my gratefulness to all the people who accompanied this journey of science and development. This work would not be in this state without your valuable contribution. I would like to thank...

- Béla Tuzson, my supervisor, for the great collaboration. I deeply appreciate your patience and your style of leading, which was always based on trust and self-reliance.
- Lukas Emmenegger for being a generous and pragmatic group leader, ready to help and advise from early morning 'till late.
- Prof. Tom Peter for being the responsible professor of this work and all the kind and helpful discussions.
- Ruud Dirksen for your willingness to co-examine my thesis. Moreover, I gratefully acknowledge the help of you and your team during the test flights at MO Lindenberg.
- Philipp Scheidegger for your priceless help as well as all the discussions related or unrelated to business. Your patience, your helpfulness and your extraordinary experience impressed me a lot.
- Herbert Looser for your versatile support – even during vacation.
- The laser spectroscopy team at Empa, namely Michele Gianella, Oleg Aseev, Morten Hundt, Berni Bereiter, Badrudin Stanicki, Akshay Nataraj, and Chang Liu for all the fruitful discussions and the good time we have had in and around the lab.
- Erwin Pieper (and his team) from the Empa workshop for your great support and the helpful advises. This also holds for Urs Hintermüller from the construction department at Empa.
- André Kupferschmid from the Empa electronics department. Thank you for your relentless efforts in Red Pitaya tweaking.
- The civil servants Yannick Stöferle, Curdin Flepp, Reto Bezzola, Florian Lienhard, and Killian Brennan for your support.
- The members of the Atmospheric Chemistry Group at IACETH for your support and the amusing time during the retreats.
- Stéphane Blaser and his team from Alpes Lasers SA for providing timely and pragmatic solutions for all our special desires concerning QCLs.
- Tobias Bühlmann for your great help during the experimental session at METAS (including overtime hours).
- Carole Delemont and Petra Forney for your valuable support in all things bureaucratic.

- A special thank goes out to my parents and Leandra for your love and support!

List of Publications

First Author Publications

M. Graf, H. Looser, L. Emmenegger, and B. Tuzson
Beam folding analysis and optimization of mask-enhanced toroidal multipass cells. *Optics Letters* 42(16):3137-3140, 2017.

M. Graf, L. Emmenegger, and B. Tuzson
Compact, circular, and optically stable multipass cell for mobile laser absorption spectroscopy. *Optics Letters* 43(11):2434-2437, 2018.

M. Graf, P. Scheidegger, H. Looser, A. Kupferschmid, T. Peter, L. Emmenegger, and B. Tuzson. Compact and lightweight QCL absorption spectrometer for balloon-borne water vapor measurements in the UTLS. *submitted to Atmos. Meas. Tech.*, 2020

Coauthored Publications

B. Tuzson, J. Jágerská, H. Looser, **M. Graf**, F. Felder, M. Fill, L. Tappy, L. Emmenegger, Highly selective volatile organic compounds breath analysis using a broadly-tunable vertical-external-cavity surface-emitting laser. *Analytical Chemistry*, 89, 6377-6383, 2017.

C. Liu, B. Tuzson, P. Scheidegger, H. Looser, B. Bereiter, **M. Graf**, M. Hundt, O. Aseev, D. Maas, and L. Emmenegger, Laser driving and data processing concept for mobile trace gas sensing: Design and implementation. *Rev. Sci. Instrum.* 89(6), 2018.

B. Tuzson, **M. Graf**, J. Ravelid, P. Scheidegger, A. Kupferschmid, H. Looser, R. P. Morales, and L. Emmenegger, A compact laser spectrometer for mobile, high-precision methane sensing aboard drones. *under review at Atmos. Meas. Tech.*, 2020

Conference Contributions

First author contributions only.

Oral Presentations

– MIRSENS 2017, Wroclaw, Poland
– European Geoscience Union Annual Assembly (EGU) 2018, Vienna, Austria
– Conference on Lasers and Electro-Optics (CLEO) 2019, San José, USA
– Swiss Geoscience Meeting (SGM) 2019, Fribourg, Switzerland

Posters

– Field Laser Applications in Industry and Research (FLAIR) 2018, Assisi, Italy